DYNAMICS OF PERTURBED EXOTHERMIC BLUFF-BODY FLOW-FIELDS

A Dissertation
Presented to
The Academic Faculty

by

Santosh Janardhan Shanbhogue

In Partial Fulfillment
of the Requirements for the Degree
Doctor of Philosophy in the
School of Aerospace Engineering

Georgia Institute of Technology
June 2008

DYNAMICS OF PERTURBED EXOTHERMIC BLUFF-BODY FLOW-FIELDS

Approved by:

Tim Lieuwen, Advisor
Associate Professor
School of Aerospace Engineering
Georgia Institute of Technology

Jerry Seitzman
Professor
School of Aerospace Engineering
Georgia Institute of Technology

Ben T. Zinn
David S. Lewis Jr. Chair and Regents' Professor
School of Aerospace Engineering
Georgia Institute of Technology

Rick Gaeta
Senior Research Engineer
ATASL/GTRI
Georgia Institute of Technology

Suresh Menon
Professor
School of Aerospace Engineering
Georgia Institute of Technology

Date Approved: 30th June 2008

When we think about the future, we always have in mind its being at the place where it would be if it continued to move as we see it moving now. We do not realize that it moves not in a straight line, but in a curve, and that its direction changes constantly.

-Ludwig Wittgenstein
(translated, from Vermischte Bermerkingen)

Where the mind is without fear and the head is held high;
Where knowledge is free;
Where the world has not been broken up into fragments by narrow domestic walls;
Where words come out from the depth of truth;
Where tireless striving stretches its arms towards perfection;
Where the clear stream of reason has not lost its way into the dreary desert sand of dead habit;
Where the mind is led forward by Thee into ever-widening thought and action---
Into that heaven of freedom, my Father, let my country awake.

-Rabindranath Tagore
(*in Gitanjali – Song Offerings*)

TABLE OF CONTENTS

LIST OF FIGURES

LIST OF TABLES

ACKNOWLEDGEMENTS

If I have seen a little further, it is by standing on the shoulders of Giants

-Issac Newton

This thesis would not have been possible without the valuable guidance of my advisor, Dr. Tim Lieuwen. I would like to offer him my heartfelt gratitude for the five years of mentoring from which I have immensely benefited.

Special thanks and gratitude are due to Prof. Zvi Rusak of Rensselaer Polytechnic Institute, with whom I had enlightening discussions on vortex dynamics. My exposure to his piercing insight in fluid mechanics was a profound experience.

I would also like to thank Prof. Zinn, Prof. Menon, Prof. Seitzman and Dr. Gaeta for serving on my committee.

A huge advantage of working in a facility like the Combustion Lab is the exposure to über-engineers such Yedidia Neumeier, David Scarborough and Sasha Bibik. I learnt a lot from their superior grasp on various issues, and adding to that, the courtesy that they extended in taking time off their overloaded schedules to patiently engage in discussions makes me truly grateful for all the help I have received.

Thanks to T. M. Muruganandam, Mohan Bobba, Preetham and Santosh Hemchandra for those endless discussions on anything and everything. I benefited greatly from their companionship during the various experiences of graduate school, good times and bad.

Thanks are also due to Bobby, Bellows, Akiva, Rob, Jermemy, Shashvat, Jo-Hyeong, JP, Nori, Nelson, Satish, Suraj, Rajesh, Qingguo, Priya, Greg Nowicki, Sai,

Jackie O'Connor, Dmitriy Plaks, Michael Seelhorst, Lisa, Shai, Jonathon Colby, Dong-Hyuk, Shreekrishna, Andrew, Prabhakar, Hann, Yogish, John Cutright, Caleb Cross, Karthik and all other staff and students at the combustion lab for taking the time off to help me at various times.

I would like to thank Master Niels Onsager and the members of the Black Knight Dojang for those unforgettable moments of my life when I used to practice Hapkido. Thanks also to Shai Birmaher for pushing me to run the half-marathon and thus leaving me with a new hobby for me to indulge myself. Thanks to Yedidia and Yossi for polishing whatever little I know of Hebrew and to Ghislain for putting up with my French.

Finally, I would like to thank Prof. R. I. Sujith and Prof. S. R. Chakravarthy who planted the seeds of my research career.

Addendum: Special thanks to Jackie O'Connor for the delicious cake she baked for my PhD defense.

SUMMARY

This thesis describes research on acoustically excited bluff body flow-fields. Bluff bodies are commonly used to stabilize flames in high velocity flows in a variety of propulsion and industrial combustion systems. This work is motivated by the problem of combustion instabilities in devices utilizing these types of flame-holders, a particularly problematic issue in jet engine augmenters.

Vortices/convective-structures play a dominant role in perturbing the flame during these combustion instabilities. This thesis addresses a number of issues related to the origin, evolution and the interaction of these structures with the flame.

The first part of this thesis reviews the fluid mechanics of non-reacting and reacting bluff body flows. It highlights the key features of the flow (the boundary layer, separated shear layer, and wake), the flow instabilities that influence each of these features, and the influences of the flame on these instabilities. A key point is the large differences between the non-reacting wake (dominated by an absolutely unstable, sinuous instability associated with vortex shedding from the bluff body) and the reacting wake of high dilatation ratio flames.

The second and third parts of this thesis present the original contributions of this study. The second part describes the spatio/temporal characteristics of bluff-body flames responding to excitation. The key processes controlling the flame response have been identified as 1) the anchoring of the flame at the bluff body, 2) the excitation of flame-front wrinkles by the oscillating velocity field and 3) flame propagation normal to itself at the local flame speed. The first two processes control the growth of the flame response and the last process controls the decay. Good agreement was also obtained when

comparing the measured flame sheet response characteristics with a kinematic model (Shin and Lieuwen, 2008) that encapsulated the dominant features of the perturbing velocity field.

The third part of this thesis describes the effect of acoustic excitation on the velocity field of reacting bluff body flows. Acoustic disturbances excite the Kelvin-Helmholtz (KH) instability of the reacting shear layer. This leads to a spatially decaying vorticity field downstream of the bluff body in the shear layers. The length over which the decay occurs was shown to scale with the length of the recirculation zone of the bluff body, i.e. the length over which the velocity profile transitions from shear layer to wake. The flame influences this decay process in two ways. Gas expansion across the flame reduces the extent of shear by reducing the magnitude of negative velocities within the recirculation zone. This combined with the higher product diffusivity reduces the length of the recirculation zone, thereby further augmenting the decay of the vorticity fluctuations. Lastly, these results also revealed the existence of phase jitter, viz. a cycle-to-cycle variation in the position of the rolled-up vortices. Close to the bluff-body, phase jitter is very low but increases monotonically in the downstream direction. This leads to significant differences between instantaneous and ensemble averaged flow fields and, in particular, the estimation of decay rate of the vorticity in the downstream direction.

CHAPTER 1

INTRODUCTION

"Experience has indicated that screeching combustion in an afterburner should be avoided and can be violently destructive of afterburner components if allowed to continue even for a fraction of a minute"
-1954, Lewis Flight Propulsion Laboratory, Clevland, Ohio

1.1.Motivation

This thesis describes research on the dynamics of acoustically forced bluff body flames. Bluff bodies are commonly used to stabilize flames in high velocity flows in a variety of propulsion and industrial combustion systems. For example, they are employed in most duct burner designs, which are widely used for supplementary firing in boilers and heat recovery steam generators, for direct fired air heating, and stack gas reheat applications (Somers 2004). In addition, most gas turbine engine afterburners rely on radial or circular arrays of stabilizers (e.g., "v-gutters") for flame stabilization. Finally, bluff body stabilized flames are often used in fundamental studies of turbulent flame characteristics (Knaus and Gouldin 2000) or as computational test cases (Rhee *et al.* 1995, Chakravarthy and Menon 1999). This work is motivated by the problem of combustion instabilities in devices utilizing these types of flame-holders, a particularly problematic issue in jet engine augmentors.

Combustion instability, or the occurrence of periodic high-amplitude pressure oscillations in the combustion chamber, is a major concern in both aircraft engines and land based gas turbines. Significant effort has been devoted to the understanding of this problem common to both types of turbines. Accordingly, the focus has been on the

combustor section. Recently there has been a renewed attention on the afterburner of aircraft engines (Lovett *et al.* 2004, Kiel 2001). Afterburners are essentially thrust augmenters. They do not produce thrust for the bulk of the flight regime; they simply provide the extra boost needed during acceleration demanding tactics such as maneuvering. Since they operate at lower pressure, after the turbine, the gas velocity is even higher than the main burner, ranging from 150 – 300m/s. In these devices, flame stabilization is generally accomplished using an arrangement such as shown in Figure 1.1.1.

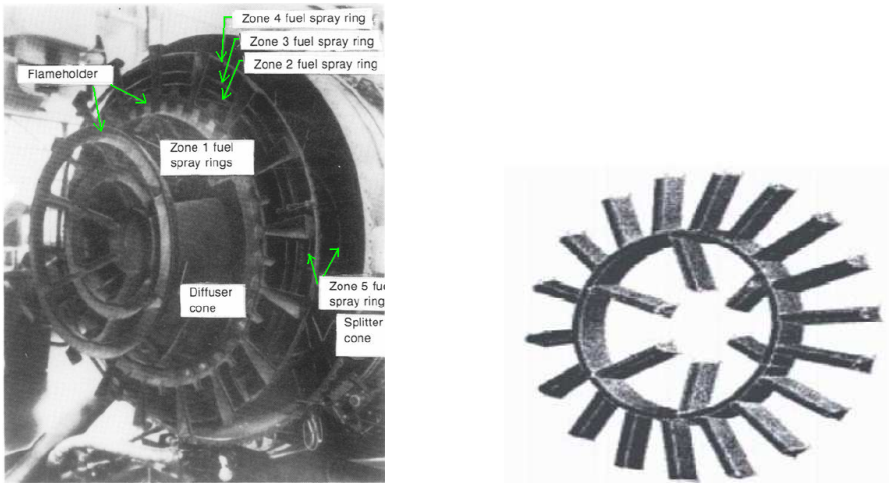

Figure 1.1.1: (Left) Photograph of an afterburner, adapted from Zukoski (1997). (Right) Schematic of bluff bodies used in afterburners, adapted from Ebrahimi (2006).

It can be seen that the flame stabilizer is a radial array of a blunt objects, in this case "V-Gutters". They, along with other blunt objects, such as circular cylinders, form a class of aerodynamics bodies known as bluff bodies, whose defining feature is flow separation at some point on their surface. As a result of separation, there exists a re-circulating region behind the bluff body. This quintessential feature is what aids in the stabilization of the flame.

1.2.Combustion Instabilities in Bluff Body Combustors

In jet engine afterburners, two types of instabilities are of interest: buzz and screech. Buzz occurs at high altitudes and intermediate Mach numbers whereas screech occurs at low altitudes and at all Mach numbers (Ebrahimi 2006). The characteristics of these instabilities are further described below.

1.2.1. Buzz

Buzz/rumble/howling is the instability that has characteristic frequencies of the order of a few hundred Hertz. During this instability, oscillations occur at frequencies that correspond to the longitudinal eigenmodes of the combustion chamber. Figure 1.2.1 compiles flame images from a number of studies where the combustor exhibited self excited oscillations at frequencies that could be connected to the longitudinal mode of the duct housing the bluff body. Further, from all these images one can see that during this instability, the flame bends over towards the flow axis at regular intervals as though it is being "pinched". The wavelength of these structures equals the ratio of the flow velocity and the frequency of oscillation. If this wavelength is large comparable to the duct length, then only one pinch occurs. If the wavelength is small compared to the duct length, a number of cusps on the flame-fronts at well defined periodic intervals in the direction of the flow, as we shall see below.

Kaskan and Noreen (1955) conducted tests on a V-gutter flame holder in a wind tunnel. They observed three modes of oscillations: pure longitudinally coupled (330 Hz), mixed longitudinally & transverse coupled (330 Hz & 4000 Hz) and finally pure transverse coupled (4000 Hz). Instantaneous flame images for the top half of the

combustor corresponding to the first two cases are shown in Figure 1.2.1(a),(b). In both these cases, notice the characteristic "pinch" that occurs near the end of the combustor. For the mixed mode, notice the presence of vortical-type structures that ride on top of the flame; these undulations are a result of the transverse mode that is also present. For the pure transverse coupled oscillation, only vortical like structures can be seen. This will be discussed in more detail in §1.2.2.

Dunlap (1950) conducted tests on confined rod stabilized flames for different bluff body sizes and approach flow velocities. He observed oscillations at a fixed frequency of 760 Hz regardless of the approach flow velocity or size of the bluff-body. The images from these tests are shown in Figure 1.2.1(c). In all three cases, periodic cusps are evident on the flame front. As the velocity increases, the distance between the cups increases.

Nicholson and Field (1948) observed periodic oscillations in lean mixtures in V-gutter stabilized flames during two test conditions: a few seconds after ignition or just before rich blowoff. They identified the frequency of pulsation to be associated with the longitudinal mode of the duct. During the pulsations, they recorded what they labeled as "alternate broadening and narrowing of the flame", as shown in Figure 1.2.1(d).

Reuter (1988) recorded a sequence of images during self-excited oscillations over a cycle of the oscillation. These oscillations were at 80 Hz that corresponded to the fundamental mode of his duct. He mentions that in course of the instability cycle 'flamelets' are periodically shed from the bluff body and propagate along the flame. A typical image is shown in Figure 1.2.1(e). Interestingly, Reuter also conducted tests in which he introduced a periodic disturbance at 385 Hz and large amplitudes into the setup;

heat release fluctuations were detected at 385 Hz but the 'flamelet shedding' still continued at 80 Hz. Instead, heat-release oscillations arising out of the 385 Hz signal was confined to a few diameters from the bluff body.

(a) Kaskan and Noreen (1955)

(b) Kaskan and Noreen (1955)

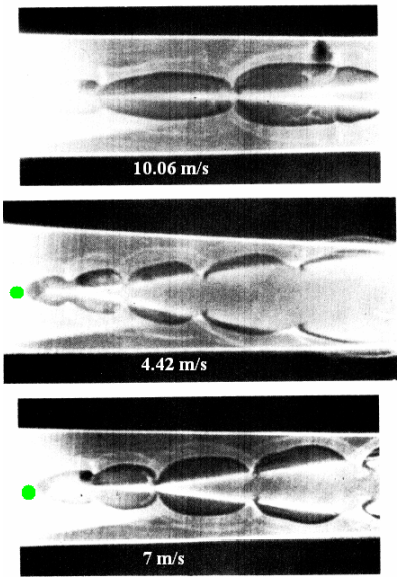

(c) Dunlap (1950)

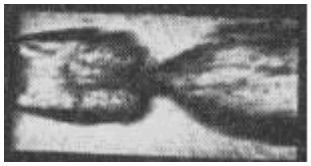

(d) Nicholson and Field (1948)

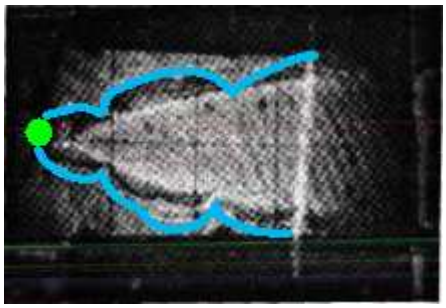

(e) Reuter (1988)

Figure 1.2.1: A compendium, of flame shapes observed during self-excited buzz oscillations in the combustion chamber. In figures (a)&(b) only the top half of the combustor was deemed necessary to be imaged due to symmetry.

1.2.2. Screech

Screech/screaming instability is a high frequency instability that occurs at frequencies of thousand's of Hertz. This instability is particularly problematic in afterburners as it leads to cracks in the housing chamber (Usow *et al.* 1953) as well as higher shell temperatures by virtue of hot-spots (Harp *et al.* 1954) leading to thermal fatigue. This instability couples with the transverse acoustic mode of the duct that houses the bluff body; hence the high-frequency signature.

In order to gain some insight into the processes that are in play during screech instabilities in bluff body combustors, images from schliren and shadowgraph studies are compiled in Figure 1.2.2.

Rogers and Marble (1956) conducted spark-schlieren experiments in a combustor with a triangular bluff-body flame holder. For a fixed velocity the combustor exhibited high frequency ocillations at 3800 Hz for certain fuel-air ratios. Regardless of the conditions at which the oscillations were seen, the frequency at which screech occured was the same, i.e. around 3800 Hz with very little variation. Further, whenever the combustor exhibited screech, flow visualization revealed the presence of anti-symmetric vortical structures (Figure 1.2.2(b)) that distort the flame front. They also pointed out that these anti-symmetric vortices "are in no way connected with the Kármán vortex street formed in the wakes of bluff bodies". Instead, they attributed the anti-symmetry to the fact the oscillations at the lips of the flameholder were out of phase. Similar antisymmetric vortical structures were also seen in the study by Kaskan and Noreen (1955) and are shown in Figure 1.2.2(a). Also, note that images from both these studies

suggest that the oscillations on the flame are restricted to a region spanning less than two bluff-body diameters.

(a) Kaskan and Noreen (1955)

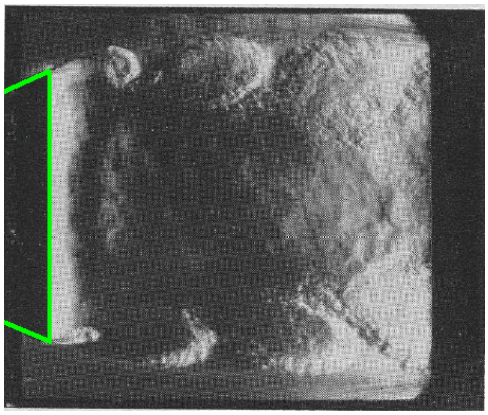

(b) Rogers and Marble (1956)

Figure 1.2.2: Flame shapes observed during self-excited screech oscillations in bluff body combustors.

In summary, the two kinds of instabilities that occur in afterburners - screech and buzz, have been reviewed. In course of screech oscillations, vortices (or convective structures) can be seen perturbing the flame over a region spanning less than two diameters downstream. During buzz oscillations too, the whole flame organizes itself into periodic structures whose wavelengths are dependent on the mean velocity, indicating convective behavior. As such, a better understanding of combustion instability (and any attempts at physics based control) requires knowledge of the role played by these coherent structures. This is addressed in the next section.

1.3.Background on Combustion Instabilities

Combustion instabilities are a feedback process that lead to self-sustained ocillations. A necessary condition to be satisfied during this interaction was proposed by Rayleigh (1896) who stated[1]: "If heat be given to the air at the moment of greatest condensation, or be taken from it at the moment of greatest rarefaction, the vibration is encouraged". This condition is incorporated in the following equation that provides a broader criterion for combustion instability (Lieuwen 1999):

$$\iint_{VT} p'(\vec{x},t)q'(\vec{x},t)dtdV \geq \iint_{VT} \sum L_i(\vec{x},t)dtdV$$

In the above equation, the terms on the left represent driving processes and the terms on the right describe damping processes. Stated differently, a combustor will be unstable only if the driving exceeds damping. Thus the first step in determining the stability of a combustion processes involves identifying the driving processes. Ducruix *et al.* (2003) review a number of such driving processes that can contribute to unstable combustion. Some of these include equivalence ratio fluctuations, flame-vortex interactions, flame wall interaction, et cetera. The process of immediate interest is the interaction between vortices (or coherent structures in general) and flames.

1.3.1. Combustion instabilities involving coherent structures

This section reviews a number of studies in which coherent structures have been known play a key role in the instability process.

Poinsot *et al.* (1987) studied vortex driven instabilities that coupled with the longitudinal eigenmodes of the combustor. Upon flow visualization it was found that a

[1] He referred to combustion oscillations as 'vibrations sustained by heat'

definite fraction of the instability cycle involved a formation of vortices at the exit of inlet jets (containing reactants) in their combustion chamber. Flames were wrapped around each vortex and continued to grow in size during the cycle increasing the interfacial area between products and reactants; this continued to a point until two neighbouring vortices interacted leading to the collapse of the vortices. This produced intense mixing between the products and reactants and was the point of maximum heat release.

Schadow and Gutmark (1992) reviewed a number of studies from literature in which coherent structures were the drivers of the combustion instability. They connected the structures to the inherent hydrodynamic instabilities arising out of the fluid mechnics of the flow. This can lead to certain configurations that are inherently unstable at frequencies that happen to coincide with the 'preferred mode' of the flow or the instability of any shear layers in the flow.

Yu *et al.* (1991) observed combustion oscillations in a dual-dump combustor at frequencies that were *not* connected to any of the eigenmodes of the combustor. The frequencies at which the combustors were rendered unstable occured at values that were a function of both an acoustic time and a vortex propagation time. Visualization revealed that the key processes generating heat release fluctuations were flame area fluctuations. The feedback loop was closed when the vortex impinged on the exit nozzle, creating a pressure pulse that travelled upstream and orchestrated the formation of a fresh vortex.

Cohen and Anderson (1996) reported measurements carried out in single-dump combustors. They found the combustor to be unstable at three frequencies. Two of these frequencies were connected to the longitudinal eigenmodes of the combustor. Ghoniem *et*

al. (2002) carried out a numerical/theoretical analysis on this configuration and attributed the third peak to an absolutely unstable mode of the wake (of the dump plane). In this case the acoustic field only acted as an amplifier.

1.3.2. Key processes of interest

From the previous section one can see that there are a number of ways in which coherent structures lead to combustion instability. A common theme emerges from all these studies regardless of the conditions/combustor-configuration under which the studies were carried out. This is schematically illustrated in Figure 1.3.1 and can be explained as a two step interaction: First, a vortical disturbance perturbs the flame; the flame responds to these perturbations giving rise to heat-release perturbations. Then, the heat-release perturbations, under favorable conditions, trigger periodic waves that now gives rise to fresh vorticity oscillations and close the loop. These two processes are the driving and the feedback processes respectively.

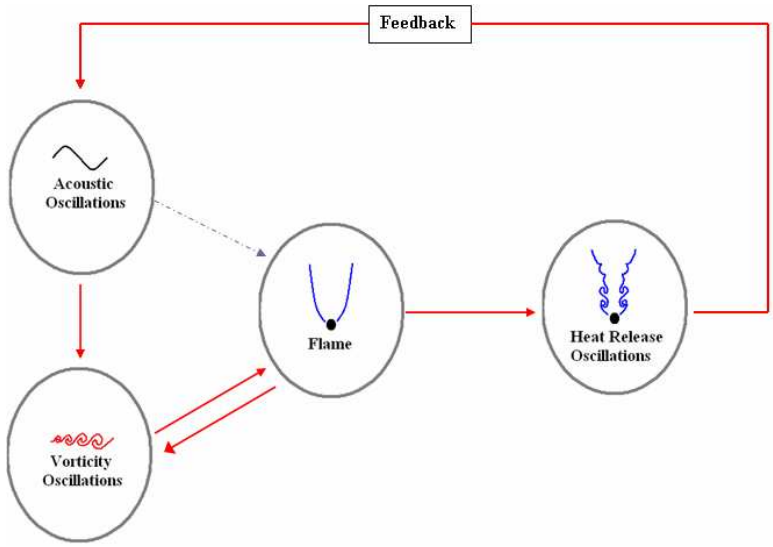

Figure 1.3.1: Interaction diagram during self-excited oscillations involving vortices.

Figure 1.3.1 exposes three key questions (part of the driving process) that need to addressed:

(a) Under what conditions are vorticity oscillations triggered by acoustic oscillations? In other words, what is the *response of the flow to excitation*.

(b) Once convective structures are generated, how does the flame respond ? In other words, what is the *response of the flame to excitation*.

(c) How does the flame influence the flow oscillations that are pertubed ? In other words, what is the *influence of the flame on the flow*.

Understanding the first and third questions requires a deeper understanding of the fluid-mechanics of bluff body flows. This involves reviewing the instabilities that are inherent to these flows. It is only then that one can address how these instabilities are affected by excitation. This is carried out in detail in Chapter 2. A background on the second question is provided next.

1.3.3. Response of the flame to oscillations

A number of prior studies have characterized the interaction of premixed flames with harmonic waves arising due to both acoustic waves (Schuller *et al.* 2003) and also convecting, vortical disturbances (Preetham and Lieuwen 2004, 2005, Birbaud *et al.* 2006). The dynamics of the flame are controlled by flame kinematics, i.e., the propagation of the flame normal to itself at the local burning velocity, and the local flow field into which the flame is locally propagating. This is mathematically described by the so-called *G* equation (Poinsot and Veynante 2001):

$$\frac{\partial G}{\partial t} + \vec{u} \cdot \nabla G = S_L \, | \nabla G | \quad (1.1)$$

The flame position is described by the function $G(\vec{x},t)=0$. Also, $\vec{u}=\vec{u}(\vec{x},t)$ and S_L denote the flow field just upstream of the flame and laminar burning velocity, respectively. In the unsteady case, the flame is being continually wrinkled by the unsteady flow field, $\vec{u}'$. The action of flame propagation normal to itself, the term on the right side Eq. (1.1) is to attempt to smooth these wrinkles out. As such, a wrinkle created at one point of the flame due to a velocity perturbation propagates downstream and diminishes in size due to flame propagation. Indeed, the dynamical interaction between the driving (acoustic oscillations) and the damping (restoration property of the flame) can lead to a range of effects depending upon the relative values of the flow oscillations and flame speed. This manifests itself through both local influences upon the flame topology (e.g., cusping, amplitude of corrugation, pocket formation), and global influences upon the overall unsteady heat release response of the flame.

1.4.Overview of the Present Work

From the background provided in the previous sections it is clear that coherent structures play a key role in combustion instability. However, a number of effects related to the origin and evolution of these structures still remain elusive for reacting bluff-body flows.

With regard to the flame response, the main body of the existing literature focuses on the 'global flame response', i.e. the spatially integrated heat-release perturbations induced as a result of acoustic excitation. In contrast few studies have characterized the simultaneous spatio-temporal characteristics of the flame response, i.e. the 'local flame response'. This is required to understand how the vortices interact with the flame.

In light of the above points, the thesis is organized as follows. Chapter 2 provides an overview of the fluid mechanics of bluff body flows. This chapter reviews the topology of the flows, the impact of exothermicity on the flow-field and the respose of different parts of the flow to acoustic excitation.

Chapter 3 describes the experimental apparatus used for the present study and the details of the measurement techniques used.

The findings of this thesis are presented in Chapters 4 and 5. Chapter 4 describes the response of the flame sheet to harmonic excitation. Chapter 5 deals with the characteristics of the velocity field that is perturbing the flame.

Chapter 6 summarizes the conclusions attained in course of the study and provides some suggestions for future work.

CHAPTER 2

FLUID MECHANICS OF 2D BLUFF BODY FLOWS

This chapter describes the flow-field of the bluff body. Section 2.1 discusses the key features of the flow, the various instabilities exhibited by each of these flow features and the resulting topology. The characteristics of the flow are described by presenting the flow-field as a combination of a boundary layer, a separated shear layer and a wake. Some discussion is also provided on how these sub-flow-fields are influenced by each other. Then, section 2.2 discusses how the presence of a premixed flame modifies these instabilities. Finally, section 2.3 presents how these flow features respond to acoustic excitation.

2.1.Flow Structures and Topology

The flow field of a bluff body is a superposition of three flow regions: the boundary layer along the bluff body, the separated free shear layer, and the wake (Prasad and Williamson 1997), see Figure 1.4.1. The boundary layer refers to the region starting from the bluff body leading edge until the separation point. The separated shear layer refers to the portion of the flow that starts at the separation point and ends at the closure point of the recirculation bubble (where the axial velocity is zero). Directly behind the bluff body is the recirculation bubble, which, depending upon bluff body width, may or may not include part of the shear layer. The wake begins where the shear-layers merge, i.e. at the end of the recirculation bubble and encompasses the region further downstream. Moreover, in the combustion case, gas expansion causes the bluff body wake to revert to a jet farther downstream, as shown in Figure 1.4.1. In turn, each of these constituent

flow-fields exhibits a range of dynamics (Williamson 1996) as described further in this section.

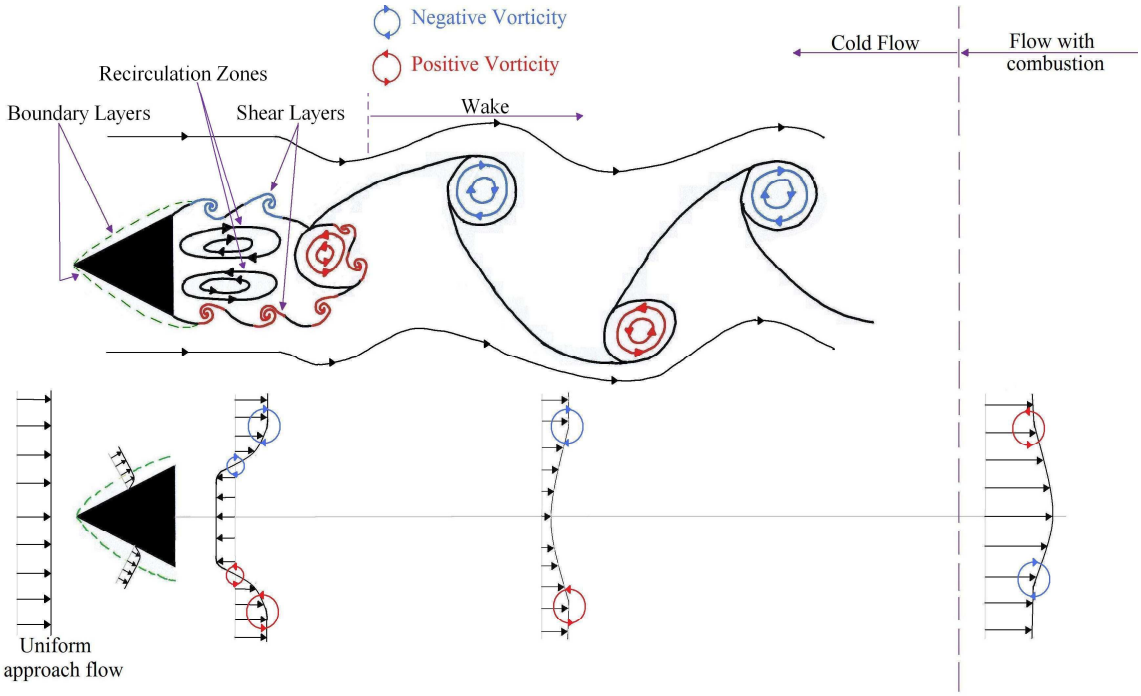

Figure 1.4.1: Schematic of key features in a low dilatation ratio bluff-body flow; time averaged velocity profiles are also shown.

The dynamics of each of these three flow features have significant influences upon flow properties, such as entrainment rates and drag coefficient. The flow characteristics are best documented for circular cross section bluff bodies (Williamson 1996, Zdravkovich 1997), where it is known that multiple distinct transitions in the base suction coefficient ($-Cp_b$, directly related to bluff body drag) dependence upon Reynolds number (Re_D) occur with increasing Reynolds numbers, as different instabilities appear in the flow or as the different flow regimes transition to turbulence. These trends are influenced by bluff-body aspect ratio, approach flow turbulence, end conditions of the cylinder, compressibility effects at high velocity and blockage-ratio.

For Re_D < ~200,000, the boundary layer is laminar (referred to as the "sub-critical regime") and the dynamics of the flow-field downstream of the bluff body is largely driven by the physics of the shear layer and wake alone. For this Re_D range, both absolute and convective instabilities are present – asymmetric vortex shedding (the Bénard/von Kármán instability, referred to as BVK from now on) and Kelvin-Helmholtz (KH) instability of the separated shear layer (see Figure 1.4.1). The former is an absolute instability, whereas the latter is a convective instability (Huerre and Monkewitz 1990). High heat release, stable flames are dominated by the KH shear layer instability. Very low heat release flame's (i.e., flames with T_b/T_u < 2, which can occur with highly preheated reactants, such as in vitiated flows), or high heat release flame's near blowoff are apparently influenced by the wake instability (Erickson *et al.* 2006). Both these phenomena are described in the following sections for nominally two-dimensional bluff bodies.

The rest of this section details the features and instabilities in the flow. An attempt is made to provide a reasonably complete picture of the flow dynamics where data and understanding is available. However, there is some disconnect in knowledge for geometries and flow regimes of interest for combustion applications. Combustion applications often utilize non-circular bluff bodies (e.g. V-gutters) at "high" Reynolds numbers, while most of the data on these topics is available for circular bluff bodies, often at relatively lower Reynolds numbers.

2.1.1. Bluff Body Wake

Bluff body wake dynamics have been most extensively characterized for the circular cylinder. This same basic picture apparently remains similar for other bluff body shapes, but the Reynolds number boundaries depend upon shape.

Below $Re_D = 40$, the entire wake is steady with two recirculating bubbles attached to the bluff body. Between $40 < Re < 50$ an absolute instability of the wake is triggered by a Hopf bifurcation (Plaschko *et al.* 1993, Provansal *et al.* 2006), leading to anti-symmetric shedding of vortices from the bluff-body, as sketched in Figure 1.4.1. This instability of the wake, which leads to shedding of concentrated regions of vorticity in the near-field, is one of the flows most prominent features. Depending upon Reynolds number, bluff body aspect ratio, and boundary conditions, this shedding can be in line with, or at an oblique angle to, the bluff body (Williamson 1996). Associated with this instability is its sinuous structure which leads to an undulating, asymmetric wake (Perry *et al.* 1982). The presence of vortex-shedding necessarily implies a sinuous wake; however, the inverse is not necessarily true (Homann 1936). The BVK instability is inherently periodic and has a characteristic frequency:

$$f_{BVK} = St_D \cdot \frac{U_\infty}{D} \tag{2}$$

where St_D is the Strouhal number and is independent of Reynolds number ($St_D = 0.21$) in the post-shear-layer-transition, sub-critical regime, $\sim 1000 < Re_D < \sim 200{,}000$, see Cantwell and Coles (1983). For bluff bodies of arbitrary shape, Roshko (1954) suggested a universal relation, $St = 0.28$, based upon a length scale defined as the vertical separation distance between the vortices in the wake. Roshko also conducted experiments on bluff-

bodies with different cross sectional shapes, such as vertical flat-plates and wedges, and found that utilizing the convection velocity of the vortices, U_s, and wake width D', as velocity and the length scales led to a universal Strouhal number $S^* = 0.16 \pm 0.02$, regardless of the shape of the bluff body generating it.

The BVK instability dominates the flow field in the region near the bluff body, but decays with downstream distance. However, in situations where streaklines are used for flowfield visualization, the presence of staggered vortices is often seen far downstream at locations where the instability is completely dissipated; see (Cimbala 1984) for a discussion. Roshko (1954) conducted experiments at $Re_D = 150$ (where the wake is laminar) and was able to detect fluctuations at the BVK frequency at downstream distances up to x/D =100. In contrast, at a Reynolds number of 10,000 the wake is fully turbulent within 40-50 diameters and no traces of periodic fluctuations could be detected at x/D =50.

Turbulence levels have important influences upon the decay rate of vortices generated by the BVK instability. As the Reynolds number is increased, the axial extent of the wake that is influenced by these vortices correspondingly decreases. As detailed in Sec. 2.1.2, turbulent transition begins to occur in the separated shear layers at about Re = 1000, further augmenting the decay of the BVK vortices.

Even though the periodic fluctuations associated with the BVK instability may be dissipated downstream, the flow-field still possesses a wake velocity profile, which is unstable (Cimbala 1984). This is apparently the reason for the appearance of another organized flow instability farther downstream after the BVK has disappeared, referred to as the "far-wake" instability, see Figure 1.4.2. These two instabilities are apparently

independent of each other (Williamson and Prasad 1993). Cimbala *et al.* (1988) conducted experiments at Re_D = 150 and showed that, although the fluctuations at BVK frequencies were completely dissipated, anti-symmetric vortices with much larger horizontal spacing were present further downstream and persisted beyond x/D > 200. The spectrum of the velocity signal confirmed the presence of lower-frequency fluctuations distinct from that of the BVK frequency. No direct connection could be established between the far-wake instability and the BVK instability in the near-field of the cylinder (Cimbala 1984). This point has also been demonstrated by experiments in which vortex shedding was suppressed with permeable splitter plates (Cardell 1993) or porous bluff bodies (Cimbala 1984). Vorobieff *et al.* (2002) reported the results of studies up to Re_D = 1000 and showed that the far-wake instability appears to originate at a downstream location scaling as $x/D \sim Re_D^{-1/2}$. Thus, as the Reynolds numbers increases, the far-wake instability appears earlier in the flow-field (Figure 1.4.2, right).

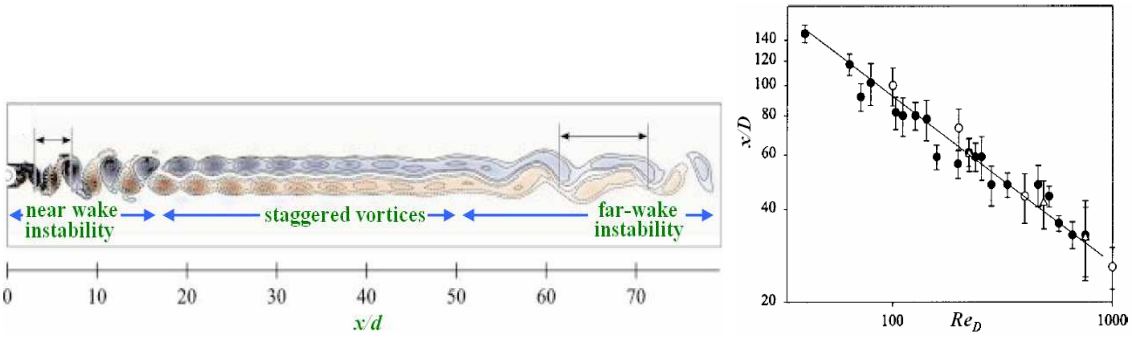

Figure 1.4.2: (Left) Computed vorticity iso-contours showing near and far-wake instability of the bluff body at Re_D = 200. (Right) Axial location of onset of the far-wake instability as a function of Reynolds number. Pictures reproduced from Vorobieff *et al.* (2002).

In summary, the wake of the bluff body exhibits anti-symmetric structures at different points that originate from two different physical processes. One occurs in the near-field of the bluff body and is the result of a Hopf bifurcation, while the other occurs

in the far-field of the body, and is apparently the result of an inviscid instability of the wake velocity profile.

Even though the BVK was referred to as dominating in the near-wake region, oscillations at its characteristic frequency are not necessarily detected at the separation point; this depends on the Reynolds number. Below Re_D ~ 10,000 or before the shear layer has completely transitioned to turbulence, vortex shedding is preceded in space by steady symmetric separation bubbles on either side of the cylinder centerline. At the end of the separation bubble, the axial velocity is zero. The region of flow between this point and the base of the cylinder is referred to as the recirculation zone. In the laminar shear layer regime (turbulence originates post-recirculation zone), i.e. Re_D<1000, L_{recirc} increases with Reynolds number. This delays the onset of vortex shedding further downstream. For Re_D>1000, the shear layer begins to transition to turbulence, causing a reduction in L_{recirc} with increases in Reynolds number. Thus, the onset of vortex shedding moves closer to the cylinder. In the same way, increasing free stream flow turbulence reduces the length of the recirculation bubble by enhancing the transition process in the shear layers. Beyond Re_D = 10,000, the steady recirculation zone reduces to a length less than half the diameter of the bluff body (Cantwell and Coles 1983, Bloor 1964) and stays constant for higher Reynolds numbers (Schiller and Linke 1933).

Above Re_D = ~200,000, the boundary layer starts to transition to turbulence. In this regime it is not clear whether vortex shedding occurs for all Reynolds numbers. Discrete frequencies are observed at certain pockets of Reynolds numbers, with corresponding Strouhal numbers of ~0.4, see Bearman (1969).

2.1.2. Separated Shear Layer

The primary instability of the separated shear-layer occurs due to the Kelvin-Helmholtz mechanism, leading to shear layer rollup into tightly concentrated vorticity. Measurements over the Re_D < 50,000 range have shown that this instability has a characteristic frequency for circular cylinders of (Prasad and Williamson 1997):

$$f_{KH} = \frac{U_{sep}}{\theta_t} = 0.0235 f_{BVK} \cdot \mathrm{Re}^{0.67} \tag{3}$$

where U_{sep} is the velocity outside the shear-layer ($0.99U_\infty$) at the flow separation point and θ_t is the momentum thickness at the transition point (the point where the momentum thickness starts growing rapidly due to growth of flow instabilities). This equation shows that this is a high frequency instability compared with the BVK at high Reynolds numbers. Unlike the BVK instability, which is an absolute instability, this is a convective instability and so this is the frequency of the most amplified mode. Indeed, spectra of non-reacting flows with this instability reveal a broadband peak as opposed to the narrowband peak that occurs for the BVK instability, as is illustrated in Figure 1.4.3.

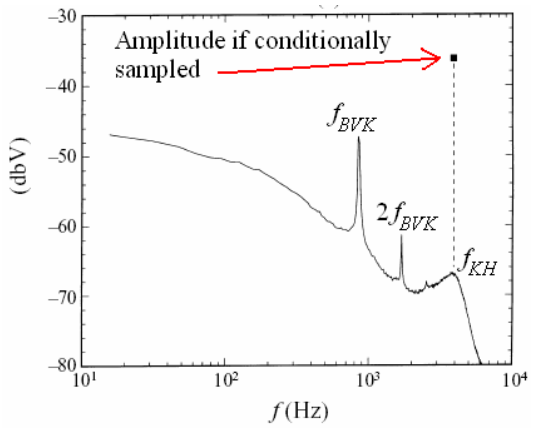

Figure 1.4.3: Spectrum of velocity fluctuations at a point downstream of the bluff body. Picture adapted from Prasad and Williamson (1997).

A number of studies were carried out to further understand the spectral features of the KH instability (Prasad and Williamson 1997, Cardell 1993, Sheridan *et al.* 1991). As was just mentioned, the high frequency oscillations of the KH instability do not yield a discrete peak in the spectrum, rather, the energy from these fluctuations are spread over a band, see the "hill" in the spectrum in Figure 1.4.3 (labeled f_{KH}). Investigation of the time signal of the velocity fluctuations (at a fixed point in space) showed that the KH fluctuations occur in bursts (Cardell 1993) . In other words, the high-frequency KH fluctuations would be contained for only a fraction of the total sample time. These bursts are because the shear layer does not initiate its rollup at the same fixed points in space, but at random locations along the shear layer. This burst rate would increase with increasing Reynolds numbers, such that for higher Reynolds numbers the KH fluctuations will be present for nearly 100% of the time. Prasad and Williamson (1997) also reported conditionally sampled measurements of the shear layer spectrum. In course of the analysis, they resolved the spectral features of the data contained in the bursts only, as

opposed to the entire time signal. This resulted in the amplitude of the KH instability being much higher than that of the BVK instability, see Figure 1.4.3.

The roll-up of the shear layer is sensitive to the span-wise variation in the BVK instability, Reynolds number, recirculation zone length and approach flow turbulence. The origin of its rollup is marked by the detection of high frequency (relative to the BVK) oscillations. These oscillations do not begin at the separation point itself, but at a location labeled the transition point (not to be confused with turbulence transition) which occurs downstream of the separation point (Sato 1956). This is shown for reacting flows in Figure 1.4.4 where part of the shear layer is laminar and the rest of it is turbulent. The location of the transition point depends on the Reynolds number and approach flow turbulence (Gerrard 1965). Increasing either of these moves the transition point upstream, facilitating the roll-up of the shear layer.

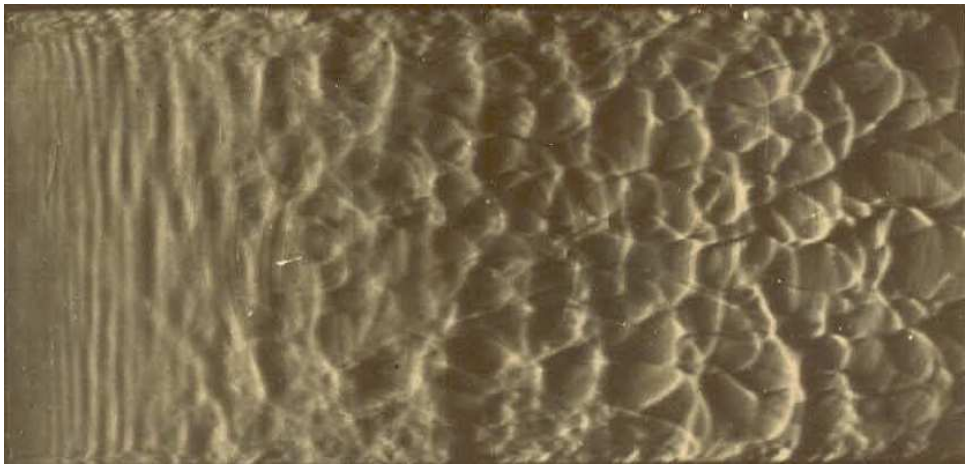

Figure 1.4.4: Spanwise view of the flame (captured using Schliren imaging) at Re_D = 7700. Picture reproduced from Zukoski (1954). Flow direction is from left to right.

All the studies cited earlier in this section were for generic bluff body flows, i.e. flows in which both the BVK and the KH instability are present. However, in what follows, the BVK instability can influence the evolution of the KH instability. This

interaction was studied by Kourta *et al.* (1987). By using hot-wire anemometry to study the velocity spectrum, they observed certain regions of the flow within the recirculation zone in which spectral peaks occurred at frequencies $f_{KH} - f_{BVK}$ and $f_{KH} + f_{BVK}$ (in addition to peaks at f_{KH} & f_{BVK}). From this, they concluded that there are non-linear interactions between the shear layer and the wake instabilities.

To isolate the development of the KH instability from the BVK instability, Cardell (1993) reported measurements in which permeable splitter plates were used to vary the degree of influence from the BVK instability. When the shear layer is allowed to evolve long enough without being impeded by the BVK instability, its evolution is analogous to that of the mixing layer; i.e., the instability grows at the fundamental mode for some downstream distance, saturates and, switches over to the sub-harmonics (associated with vortex pairing events), before completely transitioning to turbulence. Essentially, the presence of the BVK instability reduces the length of the recirculation zone, thus shortening the length over which the shear-layer evolves. If the BVK instability is absent, the recirculation zone length is elongated. This dependence of the recirculation zone length on the BVK instability illustrates that the interdependence of the shear layer and the wake mode instabilities. Understanding this interaction is a necessary first step to explain reacting bluff body flows in which the BVK instability is present only for a narrow rage of conditions.

2.1.3. On the interactions between the recirculation zone and the wake

In non-reacting flows, it is not possible to vary the Reynolds number, the recirculation zone length and the base-suction independently. For example, as the

Reynolds number is increased for Re_D>1000, the base suction also increases and the length of the recirculation bubble decreases. It remains to be seen how independent variations in base suction or the length of the recirculation zone affect the wake instability. This is a necessary step towards understanding the effect of combustion on the wake dynamics. Combustion results in gas expansion, and this modifies the recirculation zone velocity distribution. As such, Zukoski (1954) noted that the presence of the flame reduces the base suction in the recirculation zone and for a wide range of conditions, annihilation of the BvK instability, at least in the near-field.

Early attempts in studying the effect of base suction independent of the Reynolds number were accomplished by introducing a splitter plate in the flow (Roshko 1954). An important observation from this technique is that vortex shedding is suppressed due to the splitter plate and that the recirculation zone is elongated. This also results in discontinuous changes in the base pressure and reattachment of the separated flow on the plate. If the plate was made short enough, so that reattachment would occur in the flow-field as opposed to some point on the plate, then the base pressure would discontinuously change back to values as though the splitter plate was not present.

Cardell (1993) studied the non-reacting flow-field using *permeable* splitter plates. For high values of permeability, the flow-field was indistinguishable from an ordinary bluff-body flow-field (that is, a flow-field without a splitter plate). For very low values of permeability the flow-field resembled the case when a solid splitter plate was present. Between these two limits the permeability could be altered to bring about a continuous change in base pressure at a given Reynolds number. This type of investigation revealed some key insights into the flow-field. At a given permeability, changing the Reynolds

number changed the base pressure as is expected in ordinary bluff body flows. However at low permeabilities, there were certain points in the parametric space at which the base pressure was constant, independent of the Reynolds number. In such ranges, near-field vortex shedding was absent.

Continuously changing the permeability allows us to observe the transition from BVK instability to its suppression. These results are shown in Figure 1.4.5. First, notice that as the permeability is decreased, there are striking differences in the topology of the wake. For high permeabilities, both the horizontal and vertical spacing between the vortices take on values close to that of the unforced flow. As the permeability is decreased, notice that the spacing between the vortices changes. Another change that occurs with decreasing permeability is that the recirculation zone length increases. At some critical value of permeability (for a given Re_D) vortex shedding ceases to occur. At this point the length of the recirculation zone is the longest. Decreasing the permeability even further does not lead to any visible changes in the flow, at least in the field of view. The values of the base suction coefficient also cease to depend on permeability if it is further decreased from this critical value and saturates at values as if a rigid splitter plate were present in the flow (Roshko 1954).

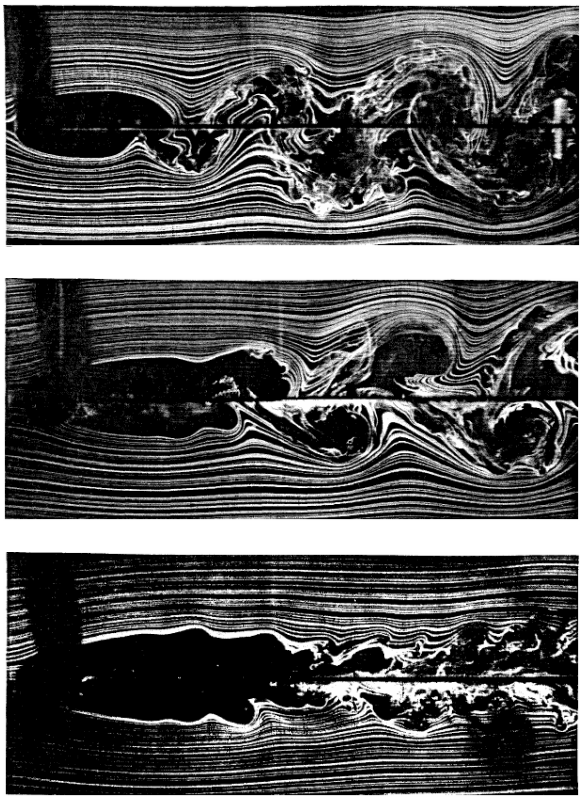

Figure 1.4.5: Smoke wire visualizations of flow past a circular cylinder at Re_D = 2500 with a permeable splitter plate (indicated by thin black line running across the image). Images reproduced from Cardell (1993).

Based on the above observations, Cardell (1993) concluded that the length of the recirculation zone is dependent on the presence of vortex shedding. This key observation allows us to explain some characteristics of the recirculation zone length for combusting flows. For instance, in lean bluff body flames ($\phi = 0.6$), the recirculation zone length was observed to be longer compared to the non-reacting case (Pan *et al.* 1992). This increase is due to the suppression of vortex shedding by combustion, a phenomenon that will be explained in the following sections.

2.2.Exothermicity Influences on the Flow Field

The previous section outlined some of the characteristic instabilities of the bluff body in a non-reacting flow. We next consider the additional physics introduced by effects of exothermicity and flow dilatation on the flow-field. In general, results indicate substantially reduced turbulence intensities and vorticity magnitudes in the combusting flows relative to the non-reacting flow. For example, studies of heat release impacts in non-premixed flames on planar shear layers indicate reduced vortex structure growth rates, entrainment rates, and Reynolds stresses compared to the non-reacting situation (Hermanson and Dimotakis 1989, McMurtry *et al.* 1989, Soteriou and Ghoniem 1994). The presence of a premixed flame, the bluff body wake, and the two interacting shear layers introduce additional complexities. For example, Fureby and Lofstrom (1994) point out that the vorticity field strength was much weaker and "less structured" in the presence of combustion. Similarly, Fujii and Eguchi (1981) and Bill and Tarabanis (1986) noted that turbulence levels in the reacting flow were much lower than the non-reacting case, particularly in the vicinity of the recirculation zone boundary. This is apparently due to the stabilization of the BVK instability, as discussed in the next section, as well as the substantial increase in viscosity in the post flame gases and the gas expansion induced vorticity sink. Other computations and data on the structure of the mean and r.m.s field are presented in Beer and Chigier (1972), Pan (1991),Fureby and Moller (1995), Fujii and Eguchi (1981), Bill and Tarabanis (1986), and Yang *et al.* (1994).

The effect of exothermic reactions introduces several additional significant physical processes upon the flow field beyond that present in the non-reacting flow. These can be understood from the vorticity transport equation:

$$\frac{D\vec{\omega}}{Dt} = (\vec{\omega}\cdot\vec{\nabla})\vec{V} - \vec{\omega}(\vec{\nabla}\cdot\vec{V}) - \frac{\vec{\nabla}p\times\vec{\nabla}\rho}{\rho^2} + \vec{\nabla}\times\frac{\vec{\nabla}\cdot\vec{\vec{\Xi}}}{\rho} \quad (4)$$

Vortex Stretching	Gas Expansion	Baroclinic Production	Viscous Diffusion
(I)	(II)	(III)	(IV)

where $\vec{\vec{\Xi}}$ denotes the stress tensor. First, the kinematic gas viscosity (term IV above) sharply rises through the flame, due to its large temperature sensitivity. This enhances the rate of diffusion and damping of vorticity, an effect emphasized by Coats (1996). Second, due to the inclination of the flame with respect to the flow (and, therefore, the pressure gradient), vorticity is generated by the baroclinic mechanism (term III above), due to the misaligned pressure and density gradients. While the exact magnitude of this term is difficult to calculate since it depends upon the details of the streamline and flame curvature (e.g., see Emmons 1958), this term is proportional to the pressure and density jump across the flame, as well as the relative orientation of their gradients. These density and pressure jumps are proportional to the gas dilatation ratio, ρ_u/ρ_b, and $\rho_u S_L^2(1-\rho_b/\rho_u)$, respectively. The orientation of their gradients is a function of the flame/flow angle that, in turn, depends on the ratio of flame speed and flow velocity, S_L/U_∞.

Since the magnitude of the baroclinic vorticity is also a function of the temperature ratio across the flame and the relative angle of the flame and flow, the relative strengths of the two vorticity sources is also determined by flame temperature,

flame speed and flow velocity. Thus, the vorticity distributions shown above will be substantially altered as these parameters are varied.

Third, there is gas expansion behind the flame (term II above). The flow dilatation acts as a vorticity sink, as can be seen by the negative sign of this term, $\vec{\omega}\nabla\cdot\vec{V}$, in the vorticity transport equation above. This term is also directly proportional to the gas dilatation ratio across the flame, ρ_u/ρ_b.

Some appreciation for the complexity of the dependence of the vortex dynamics on flow parameters can be appreciated by noting the impact of variations in flame temperature, flame speed, and axial flow velocity: A variation in flame temperature and, therefore, gas expansion ratio, ρ_u/ρ_b, effects both vorticity source and sink terms. It increases baroclinic vorticity production (term III) but also increases the flow dilatation (term II) and gas kinematic viscosity (term IV). On the other hand, variations in the flame speed at constant expansion ratio impact the relative flame-flow alignment, and thereby the baroclinic vorticity production (term III), but probably not the other vorticity source/sink terms. Variations in the axial flow velocity, U_∞, impact the wake and baroclinic generated vorticity (term III), but not the dilatation term.

2.2.1. Exothermicity Influences on the Shear Layer

In high velocity flows, the flame lies nearly parallel to the flow and, thus, almost directly in the bluff body shear layer. The separating vorticity sheet on both sides of the bluff body rolls up, which induces a flow field that wraps the flame around these regions of intense vorticity. This wrinkling and corrugation of the flame sheet by this unstable, separating shear layer has been noted in a number of prior studies, such as shown in

Figure 1.4.7 and Figure 1.4.8. In general, the rollup of the shear layer occurs in a somewhat random spatial location, but can be phase locked with the introduction of acoustic forcing (Nottin *et al.* 2000).

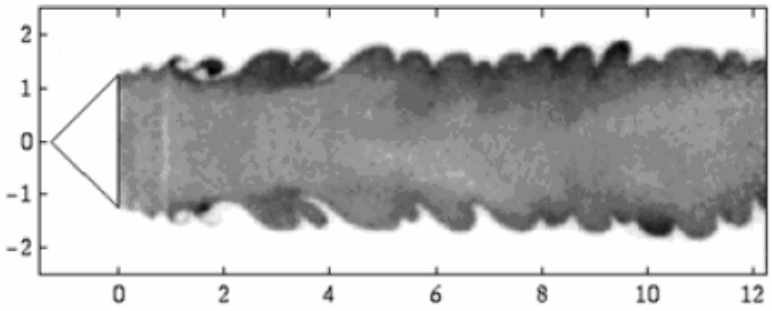

Figure 1.4.6: Instantaneous OH-PLIF image of premixed, flame stabilized by triangular flameholder. Picture reproduced from Nottin *et al.* (2000)

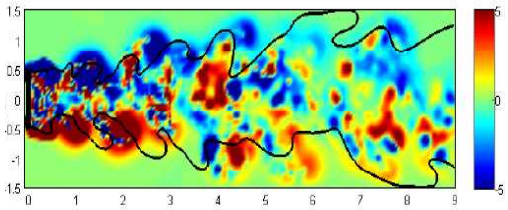

Figure 1.4.7: Computed vorticity contours and flame location for a triangular flameholder. Picture reproduced from Erickson *et al.* (2006).

There are significant interactions between exothermicity and the shear layer (Mehta and Soteriou 2003). Most significantly, there are interactions between shear generated vorticity and flame-generated, baroclinic vorticity. Assuming that the pressure is decreasing in the flow direction, then the baroclinic vorticity is of the opposite sign as bluff body generated vorticity. As such, there is a competition between shear and baroclinic vorticity sources, which can result in complete cancellation, and then sign reversal, of flow vorticity in certain regions of the flow. Apparently, the flow near and far from the bluff body is dominated by bluff body and baroclinic generated vorticity,

respectively. An alternative, but equivalent way of thinking of this, is to note that the near field bluff body wake transitions into a jet in the far-field, see Figure 1.4.8.

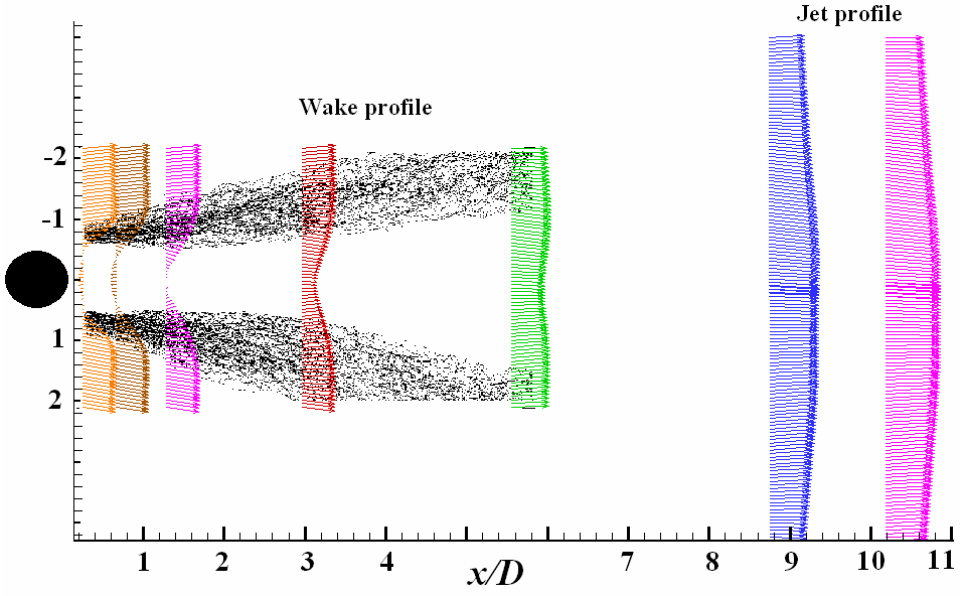

Figure 1.4.8: Experimentally measured mean-velocity profiles at different stream-wise locations downstream of an exothermic bluff body flow-field. Black lines denote the flame brush. The bluff body is also shown for reference, drawn to scale. For this flow U_∞ = 1.55 m/s, equivalence ratio ϕ = 0.71 & bluff-body diameter D = 6.35 mm.

This competition has important implications upon the interactions between flame dilatation ratio and the fluid mechanic strain imposed on the flame. If the flame dilatation ratio drops due to, e.g., a decrease in equivalence ratio or increase in preheat temperature (such as vitiation level), the magnitude of the flame generated baroclinic vorticity source term decreases, due to the decreasing density jump across the flame. In addition, the vorticity damping term due to flow dilatation (given by the $\vec{\omega}\nabla\cdot\vec{V}$ term in the vorticity transport equation) also decreases. This necessarily means that *the flame near the bluff body experiences a higher magnitude vorticity field* than it did at higher equivalence ratios, and a vorticity field that persists farther downstream. The average vorticity decreases with increasing axial distance for all cases and at some point, switches sign from positive (bluff body generated vorticity) to negative (flame generated

vorticity). Measurements by Nair and Lieuwen (2007) & Bush and Gutmark (2006) show such characteristics.

Fundamental studies of vortex-flame interactions has shown that the nature of the flow changes substantially with the amplitude of vorticity perturbation (Wu and Driscoll 1992, Sinibaldi *et al.* 1998 & Louch and Bray 2001). For low vortex strengths, the flame is wrinkled with an amplitude proportional to the ratio of u_θ/S_L, where u_θ in this case denotes the velocity amplitude associated with the vortex. The amplitude of the vortex decreases through the flame due to volume dilatation and the large diffusivity of the products. Furthermore, if the flow and flame are nominally normal to each other, the baroclinic term is zero. As the amplitude of the vortex increases, the flame becomes highly wrinkled to the point that vorticity can also be produced/destroyed by baroclinic processes. i.e., very strong vortices distort the flame to such an extent that they change the sign of the baroclinically generated vorticity along the corrugated flame sheet. This point was made by Louch and Bray (2001): "with increasing vortex rotation rates, the flame wraps around the vortex and results in 'scrambling' the alignment of the density and pressure gradients, causing different signs of baroclinic torque along the flame". However, one key difference between the present investigation and the above cited studies is the fact that the flame is nominally at an angle to the flow, so that baroclinic vorticity is present even in the nominal, unforced case. Nonetheless, this discussion illustrates the complications that can arise between shear generated vorticity that has its own dynamics (e.g., rollup, pairing, growth, etc.), viscous diffusion, volume dilatation, and baroclinic processes.

2.2.2. Exothermicity influences on the Wake Flow

A significant change in the fluid mechanics of the bluff body wake is the apparent stabilization of the wake instability in the bluff body near-field in the presence of large flow dilatation; e.g., T_b/T_u>~2 (Erickson *et al.* 2006). That is, for flames with large density ratios across the flame, the BVK instability is apparently suppressed (Fujii and Eguchi 1981, Yamaguchi *et al.* 1985). For example, comparisons of velocity spectra show a narrowband peak in the non-reacting case that is absent in the presence of combustion, as shown in Figure 1.4.9. There are a few exceptions as, for example, Yang *et al.* (1994) present visualizations showing sinuous structures – these are, however, farther downstream of the bluff body and not in its immediate near-field, see also Zukoski (1954), Figure 1.4.11 and Figure 1.4.12. Also, Hertzberg *et al.* (1991) were able to detect harmonic velocity fluctuations for lean acetylene-air flames. These were, however, of lower frequency compared to the case when the flame was absent.

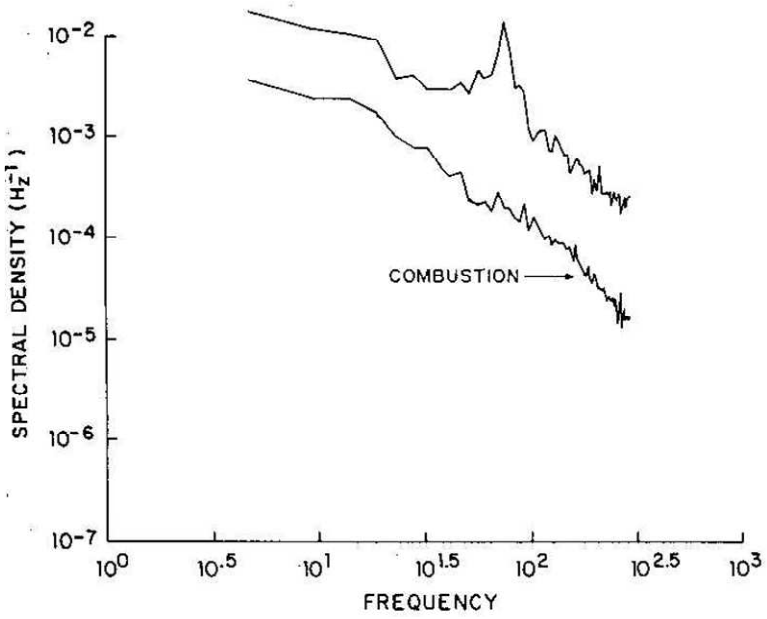

Figure 1.4.9. Comparison of velocity spectra with and without combustion in a Re=1000 flow, reproduced from Bill and Tarabanis (1986).

In general, however, the flow field loses its sinuous, undulating character, the dominant feature of the non-reacting flow, and is dominated by much weaker flow fluctuations of the shear layer, at least in the bluff body near field, see Figure 1.4.10. Overall, vorticity levels are significantly lower in the reacting wake. The reasons for this shift have been considered extensively by Mehta and Soteriou (2003). They suggest that, due to gas expansion at the flame, vorticity is reduced and, thus, the interaction of the separating vortex sheet from one side with the oppositely signed vortex sheet from the other side of the bluff body (which leads to vortex shedding; Perry *et al.* 1982), is inhibited. Note, however, that the flow does apparently revert to back to a sinuous structure in the farfield, such as shown in Figure 1.4.10 and Figure 1.4.11.

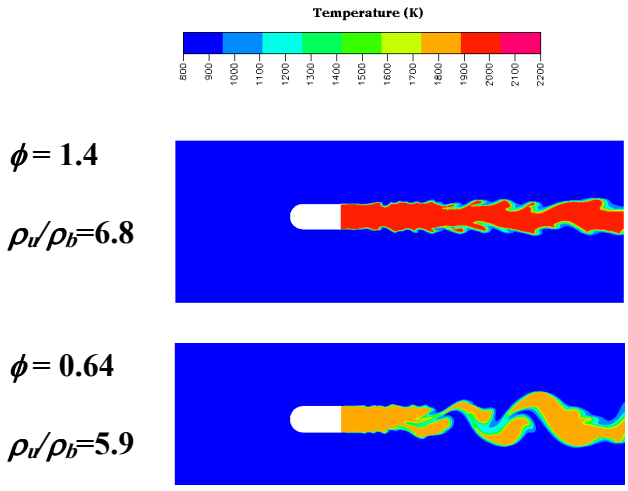

Figure 1.4.10: Temperature distribution for high dilatation ratio flames Smith *et al.* 2007.

The above observations suggest that the wake mode should be present at low T_b/T_u values. This has been demonstrated by Erickson *et al.* (2006) who computationally demonstrated that the BVK instability magnitude gradually grows in prominence below a T_b/T_u value of approximately 2-3. This phenomenon is illustrated in Figure 1.4.11 and Figure 1.4.12, which show instantaneous flame sheet locations at several dilatation ratios. Although other parameters, such as relative flame/flow angle and bluff body blockage ratio also doubtlessly exert influences, these results suggest that the dilatation ratio across the front is the key parameter that influences the relative significance of the BVK and KH instabilities.

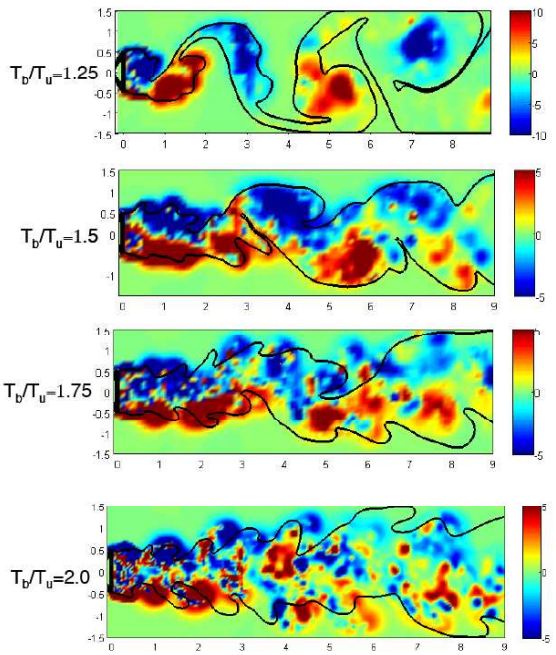

Figure 1.4.11: Vorticity contours and instantaneous flame positions for triangle stabilized flames at various dilatation ratios. Picture reproduced from Erickson *et al.* (2006).

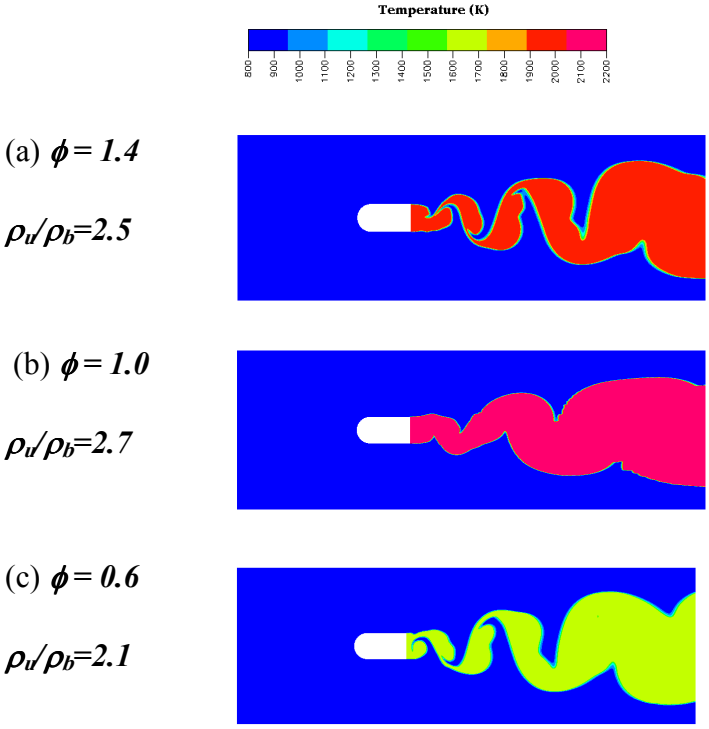

Figure 1.4.12: Temperature distribution for bluff body stabilized flames at low dilatation ratios (Smith *et al.* 2007).

There is a fairly uniform consensus that vortex shedding/sinuous wake structure is suppressed in the bluff body near-field in the presence of combustion. However, as also mentioned above, several results do indicate that the wake reverts to a sinuous structure farther downstream. Such behavior is pointed out explicitly by Fureby and Moller (1995), and can be seen in the results of Smith *et al.* (2007), Thurston (1958). One possibility is that this occurs at the point where the flow transitions from a wake to a jet, as 2-D jets are well known to be unstable to anti-symmetric disturbances (Crow and Champagne 1971), or that it related to the far wake instability described in §2.1.1.

Directly related to the structure of the wake is that of its entrainment dynamics. As products exit the flame, some are entrained into the recirculating wake and some convect downstream. Under near blowoff conditions, holes in the flame appear, leading to propagation of unburned reactants through the nominal flame location. It can be anticipated that their entrainment into the wake may significantly alter these wake dynamics. Thus, determining the nominal wake entrainment characteristics and the axial distance over which entrainment *vs.* downstream convection occurs is an important issue associated with understanding flame blowoff phenomenon.

Such exchange processes cannot be understood from time averaged streamlines, as there is a dividing streamline between the closed recirculation bubble and that of the outer flow; i.e., these dynamics are controlled by unsteady exchange between coherent vortices and fine scale turbulence. The exchange between the outer flow and wake was considered primarily in two experimental studies by Winterfeld (1965) and Bovina (1959). Measurements of the actual entrainment rates into the wake were not obtained,

but both determined rates at which particles leave the wake, given by $C(t)=C_o exp(-t/\tau_{recirc})$, which must balance the rate of entrainment on average. In both studies, it was found that the τ_{recirc} scaled with bluff body diameter and approach flow velocity, $\tau_{recirc} \sim D/U_\infty$ for a fixed approach flow turbulence intensity. Winterfield also varied blockage ratio, showing that the velocity scale in the above relationship is the lip velocity, U_{lip}, as expected. The proportionality constant relating this time scale and the ratio D/U decreased with approach flow turbulence intensity. Moreover, it increased in the presence of combustion by a factor of about three, having values of ~100, compared to ~37 for non-reacting flow. This time scale exhibited little dependence upon fuel/air ratio over the range tested.

In addition to the bluff body transverse dimension, D, and shear layer thickness, θ, the length of the time averaged recirculation region, L_{recirc}, is a natural length scale. There is a wide range of data in the literature showing L_{recirc} increasing, decreasing, or staying constant with changes in fuel/air ratio, bluff body type, and fuel/air ratio (Pan *et al.* 1992, Potter and Wong 1958, Zukoski and Marble 1956). Two different perspectives of the recirculation zone are presented in Figure 1.4.13. The first, derived from its time-averaged streamlines, depicts it as two symmetric, recirculating eddies. An alternative perspective is shown in Figure 1.4.13 (right), indicating that the recirculation zone length is controlled by the merging distance for the two distinct shear layers. As discussed in §2.1.2, there are some analogies with the evolution of the free shear layer and and mixing layers.

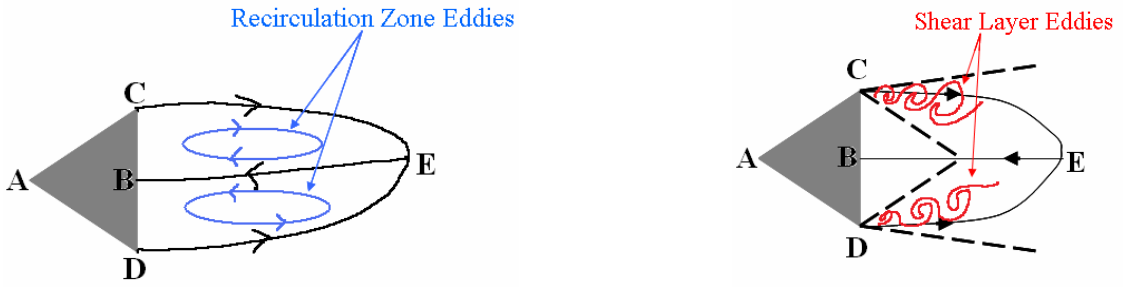

Figure 1.4.13: (Left) The recirculation zone viewed as a region of two steady eddies. (Right) The recirculation zone viewed w.r.t. two interacting shear-layers. Dashed lines indicate the mixing layers and solid black lines denote the streamlines.

It is helpful to categorize the shear layer momentum transport processes by whether it is molecular diffusivity, transitional, or turbulence dominated. In non-reacting, circular bluff body flows, these zones are demarcated roughly by Re_D<1000, 1000<Re_D<10,000 and Re_D > 10,000. Zukoski and Marble (1956) observe similar limits for exothermic flows. In the turbulent regime, transverse turbulent momentum transport increases proportional to flow velocity, leading to L_{recirc} scaling that is invariant with flow velocity/Reynolds number (Pan *et al.* 1992, Potter and Wong 1958, Schiller and Linke 1933, Zukoski and Marble 1956). These trends can be seen in Potter and Wong's (1958) data**,** reproduced in Figure 1.4.14. For an analogous reason, L_{recirc} increases with approach flow velocity in the laminar and transitional regimes. Also, approach flow turbulence can alter the turbulence transition point/Reynolds number of the shear layer and have a corresponding influence upon L_{recirc}. For example, increasing the approach flow turbulence reduces L_{recirc} in the transitional regime for both exothermic (Pan *et al.* 1992) and non-reacting flows (Gerrard 1965). Fuel/air ratio or ratio of burned to unburned gas temperature effects are more complex, but have similar sensitivities. Data indicates that L_{recirc} exhibits little sensitivity to fuel/air ratio in the turbulent regime (Ames 1956, Potter and Wong 1958, Zukoski and Marble 1956), but decreases with

increasing fuel/air ratio in the laminar/transitional regime (Foster 1956, Nair 2006, Pan *et al.* 1992, Zukoski and Marble 1956).

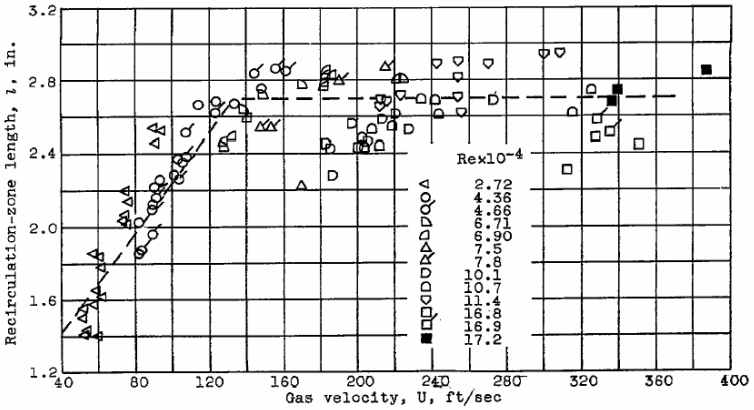

Figure 1.4.14: Recirculation zone length, L_{recirc}, as a function of approach flow velocity. Picture reproduced from Potter and Wong (1958).

2.3.Response of the flow to Acoustic Excitation

This section reviews different studies to gain some knowledge of how the different structures in the wake respond to harmonic perturbations.

Blevins (1985) studied the spectral characteristics of the wake when a transverse acoustic mode was excited in the windtunnel. The measurements were made using Hot-Wire anemometry without any accompanying flow visualizations. Blevins observed that it takes large amplitudes to shift the vortex shedding frequency from its natural frequency to that of the imposed excitation. These results are reproduced in Figure 1.4.15. For the conditions described, natural vortex shedding occurs at 392 Hz. The response of the wake was then studied by exciting the 380 Hz (transverse) mode of the wind tunnel duct. Notice that only at amplitudes as high as 142 dB does the spectral feature at 392 Hz vanish. At a lower amplitude, i.e. at 136 dB, peaks are present at both the natural and the forced frequencies. As the frequency of excitation shifted further away from the natural

frequency of shedding, it required larger amplitudes to "entrain" the shedding at frequncies matching that of the excitation.

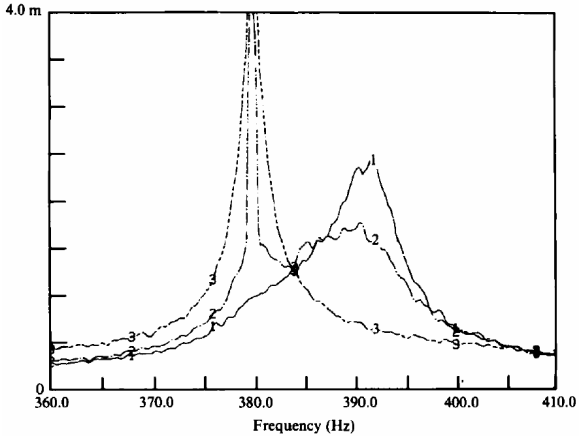

Figure 1.4.15: Spectrum of the flow at Re_D = 22,000 when excited at f = 380 Hz, without excitation (1), 136 dB (2) & 142 dB (3). BVK oscillations occur at f = 392 Hz. Image reproduced from Blevins (2006).

Both, flow visualization and velocity measurements for acoustically excited bluff body flows were also reported by Desruelle (1983). For the range of frequencies at which excitation was carried out, it was observed that the wake responds at $f_{response} = (f_{BVK} - f_{excitation})$. He also studied the spatial evolution of the response amplitude. The results are shown in Figure 1.4.16 (left). Close to the cylinder, i.e. for $x/D < 25$, fluctuations are present only at f_{BVK}. Further downstream the spectrum reveals fluctuations at both f_{BVK} & $f_{response}$. Also, in these tests, fluctuations at $f_{response}$ were detected upto $x/D = 300$ whereas fluctuations at f_{BVK} had decayed by $x/D = 200$. Thus, during excitation, the flow topology takes on three shapes. In the near field, the flow structures resemble that of the BVK instability. In the intermediate region, the flow structure resembles that as shown in Figure 1.4.16 (right). Finally, at large distances from the bluff body, only fluctuations at $f_{response}$ are detected. In this region, the topology resembles the far-wake instability.

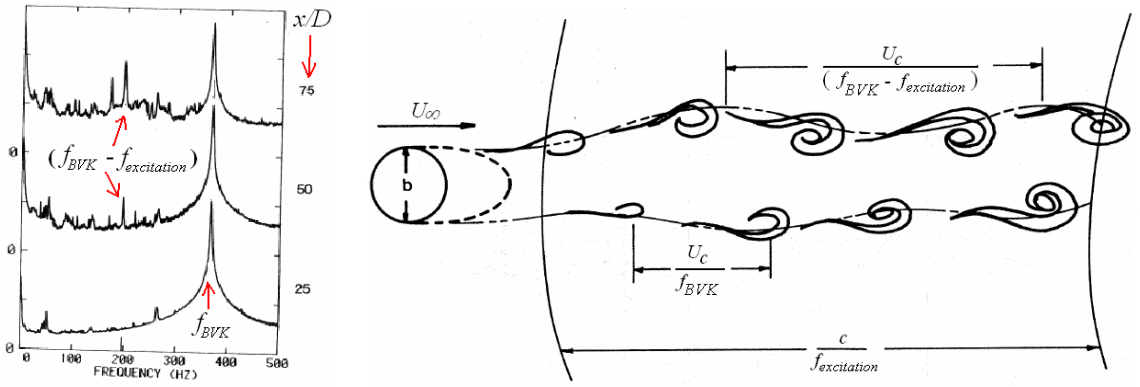

Figure 1.4.16: (Left) Spectrum of velocity fluctuations at different downstream locations for Re_D = 155. The y-axis is plotted on a log scale. (Right) Corresponding flow schematic. Notice that the BVK instability rides over a wake that is "breathing" at a lower frequency. Images adapted from Desruelle (1983).

The response of the shear-layer to acoustic excitation in non-recting flow was studied by Sheridan *et al.* (1991). They chose the frequency of excitation as per the equation $\frac{f_{KH}}{f_{BVK}} \propto \mathrm{Re}^{0.87}$. Flow visualization revealed the presence of distinct, small vortices bounding the recirculation zone as a result of the excitation. They also reported that the shear layer responds to a range of frequencies (an observation also reported by Cardell 1993); this range increases as the Reynolds number increases. Finally, they mention that their spectrum also contained peaks at $f_{KH} - f_{BVK}$ & $f_{KH} + f_{BVK}$ during excitation. From this, they conclude that there are non-linear interactions between the BVK instability and the KH instability during acoustic excitation, although they could not tie these spectral peaks to any features in the topology

2.4.Summary

This chapter reviewed the topology of bluff body flows. Coherent structures of different sizes are seen in different regions of the flow. These structures originate due to different mechanisms. The anti-symmetrical structures that exist between the end of the

recirculation zone to some point further downstream in the wake is the BVK instability; this is an absolute instability. On the other hand, the vortices that exist in the "far-wake" are apparently due to the instability of the velocity profile. Between the bluff body trailing edge and the end of the recirculation zone, small scale (or high frequency) vortices are seen depending on the Reynolds number; these vortices arise out of the Kelvin-Helmholtz mechanism. Some attention was also devoted to reviewing experiments that used permeable splitter plates to modify the characteristics of the BVK instability. This revealed the dependence of the recirculation zone length on the BVK instability. For the particular case when the BVK instability is suppressed, the recirculation zone length is at its longest size.

The impact of exothermicity on the bluff body flow-field results in two new influences. The first is volume dilatation, due to the gas expansion. The second influence is due to the inclination of the flame with respect to the pressure gradient also known as baroclinic torque. Additionally, the high temperatures accompanying combustion products result in enhanced viscous diffusion. A direct result of combustion in the flow-field is seen as the velocity profile transitions from a wake profile to a jet profile. Combustion was also shown to have significant influences on the wake mode instability. As opposed to non-reacting flows where the wake mode instability is ubiquitous, it is suppressed during combustion for dilatation ratios greater than ~2.

The parts of the bluff body flow-field most receptive to the acoustic forcing are the convectively unstable regions, i.e. the shear-layer and the far-wake. Both of these respond to a wide range of forcing frequencies and amplitudes. The shear-layer response frequency is the same as the frequency of the imposed perturbation ($f_{response} = f_{excitation}$)

whereas the far-wake responds at $f_{response} = f_{BVK} - f_{excitation}$. By contrast, the BVK instability responds chiefly at large amplitudes of excitation and frequencies close to the natural frequencies of vortex shedding. As the frequency of excitation is moved further away from f_{BVK}, it requires a larger amplitude to completely entrain vortex shedding to the frequency of the imposed excitation.

CHAPTER 3

EXPERIMENTAL APPARATUS AND METHODS OF ANALYSIS

This chapter begins by detailing the experimental setup and the instruments used to carry out flow measurements. §3.2 describes the planar Mie-scattering technique, used to visualize and quantify the movement of the flame front. §3.3 provides the details of velocity measurements used to map the velocity profile and acoustic field at the burner exit. Finally, §3.4 delineates the specifics of the PIV technique used to carry out velocity and vorticity field measurements, with and without combustion.

3.1. Description of the Combustor

All experiments were carried out in an atmospheric pressure burner with a square cross-section (4.85" x 4.85") that is 3' long (Figure 3.1.1). Fuel, air and seeding material are introduced in a mixing chamber located at the base of the burner. Depending upon the diagnostic technique, two different seeding materials were used. Four micron (median size) olive oil droplets and 1.5 micron Al_2O_3 particles were used for Mie scattering and PIV measurements respectively. The olive oil droplets were with an aerosol seeder utilizing Laskin nozzles and commercially available olive oil. The Al_2O_3 particles were introduced into the setup using a cyclone seeder filled with powdered seeding material.

The fuel and air flow rates are measured with rotameters with accuracies of 2% (see Appendix A) and 4% respectively. The premixed mixture exits the mixing chamber into a six inch tube of the same cross-section as the burner, which also contains the 100W Walsch PA acoustic loudspeakers. The mixture then passes through a honeycomb grid flow straightening section. The bluff body is mounted at the immediate exit of the

channel. The excitation was carried out using loudspeakers that were sinusoidally forced with an Agilent 33120A-15 MHz connected in series with a RadioShack MPA-101, 100 Watt amplifier.

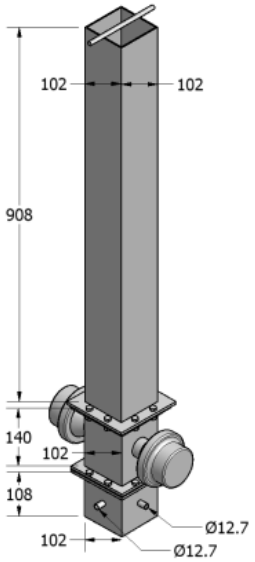

Figure 3.1.1: Schematic of the experimental setup, drawn to scale. Dimensions are also indicated, in millimeters

On this burner, two laser-based diagnostics were applied to investigate the flame response and the velocity field. These are planar Mie-scattering and particle image velocimetry, described in §3.2 and §3.4 respectively.

3.2.Planar Mie Scattering

This technique that was used to quantify the spatio-temporal flame response.

3.2.1. Details of the technique

In order to extract a distinct reactants/product interface, the inlet premixed mixture is seeded with micron size olive oil droplets. At these sizes, the evaporation temperature of these droplets is of the order of 600K (Muruganandam 2006), well below the lowest flame temperature for which measurements are conducted in this thesis

(1700K at $\phi = 0.63$). Then, a planar sheet light sheet is used to illuminate the field of view as shown in Figure 3.2.1. This light sheet originates from a continuous Ar-Ion laser of wavelength 514.5 nm. A cylindrical lens arrangement provides a diverging 2 mm thick light sheet that passes through the flame at the bluff body midpoint. The resulting plane was directly imaged onto a high speed camera with bandpass filters in front of it to reduce stray background light. The details of the cameras and lasers that were used to capture the images and are listed in Table 3.1.

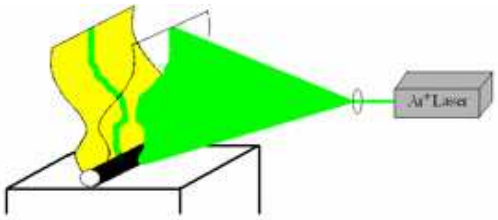

Figure 3.2.1: Schematic illustrating a planar measurement. The span of the illumination is of the order of the thickness of the laser beam.

Table 3.1: Details of the laser, camera and lenses used for planar Mie scattering.

No.	Laser	Camera	Resolution	Lens & Optics	Field of View
1	8W Coherent Innova 90C, Argon Ion	Redlake Motionscope PCI-2000S	320 x 280	Nikon 50 mm, f#-1.4	88.9 mm x 65.5 mm

2	1W Coherent Innova 70-5, Argon Ion	Phantom Ultracam3 with intensifier	512 x 512	Nikon 55 mm, f#-2.8 lens. 514 nm laser line filter. BG-7 Schott Glass absorption filter	109 mm x 109 mm.

At each collection point, 2048 images were obtained at 500 frames/second with an exposure time of 400 microseconds. These parameters were chosen to comply with the Nyquist criterion and optimize between resolution and processing time.

3.2.2. Quantification of flame front movement

The flame sheet dynamics were quantified by tracking the flame edge. The coordinate system is shown in Figure 3.2.2 where the *(x,y)=(0,0)* point is chosen as the bottom of the bluff body centerline. Thus we obtain the flame location, *L(y,t)* at each time instant, *t*, and each spatial location, *y*. The mean value of *L* at each *y* location is subtracted to get a flame front perturbation, $L'(y,t) = L(y,t) - \overline{L(y,t)}$. This signal is then decomposed into its spectral components using the Fourier transform (implemented using the FFT algorithm) to yield *L'(y, f)*.

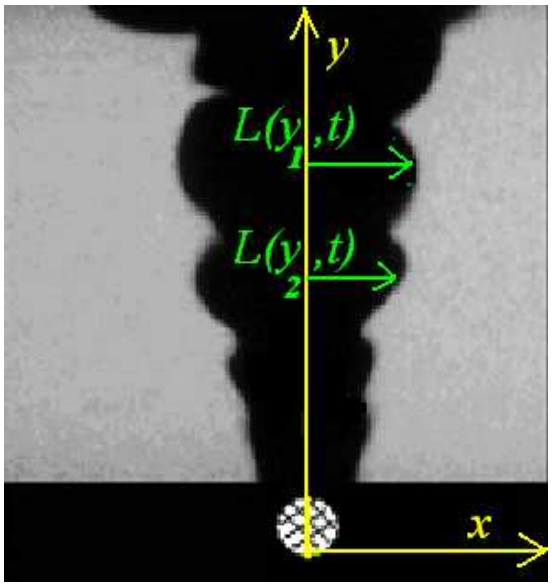

Figure 3.2.2: Schematic of the reference axis used. A caricature of the cylinder is shown to better represent the reference frame.

3.3.Hotwire Measurements

Single point velocity measurements were obtained with a Dantec Streamline CTA hotwire system (with a 55p11 probe) calibrated using a Dantec 90H02 unit to a precision of 2%. As will be discussed next, this technique was used to check the uniformity of the velocity profile, estimate the turbulent intensities in the setup and to measure the acoustic amplitudes output by the loudspeakers. The acoustic velocity amplitudes reported in later sections/chapters were obtained at the center of the jet exit, without the bluff body mounted.

The normalized mean and acoustic velocity distribution across the burner (the z-direction) are shown in Figure 3.3.1a and Figure 3.3.1b respectively. These show transverse uniformities within 3% and 4% respectively, for the regions away from the edges. In addition, the velocity profile was also measured with air flow through the seeder to observe the impact of seeding injection on the velocity profile. The results are

shown in Figure 3.3.3. As the volume flow rate through the seeder increases, so does the mean velocity because of the extra mass flow, but this does not lead to any major changes in the spatial distribution of the velocity profile.

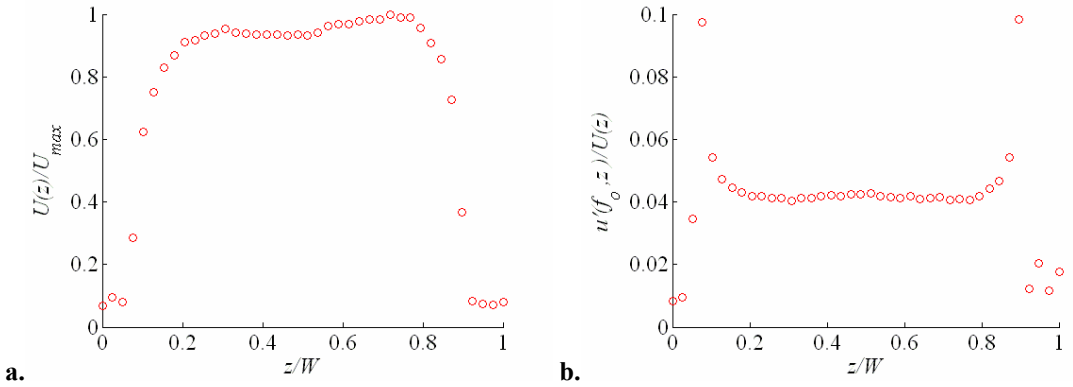

a. **b.**

Figure 3.3.1: a. Velocity profile measured across the burner, normalized by the burner width b. Profile of acoustic velocities, normalized by the mean velocity at that point. Conditions: U_∞ = 1.8 m/s, f_o = 130 Hz.

To estimate the turbulent intensities in the approach flow, 131,072 (2^{17}) velocity samples were collected at each velocity by fixing the probe at the center of the burner. The velocity was varied between 1.5 m/s to 7 m/s and the standard deviation of all the samples in a set were computed. The results are plotted in Figure 3.3.2. From this graph, we estimate the turbulent intensities, $u'/\overline{U}_o$ for the setup to be 7.4% for the range of experiments conducted.

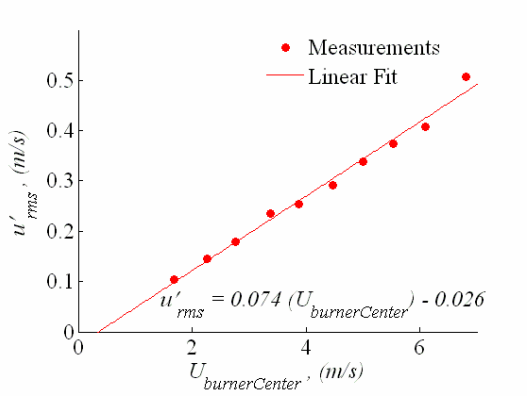

Figure 3.3.2: Plot of turbulent intensities at different mean velocities.

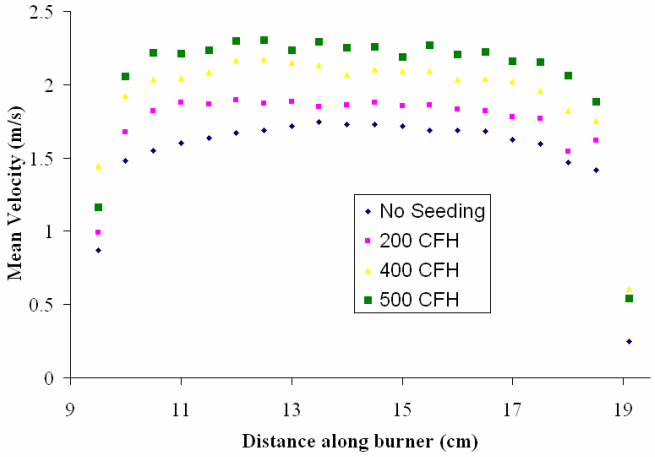

Figure 3.3.3: Velocity Profile along the burner for different volume flow rates through the seeder

In addition to the measurements above, acoustic velocities were obtained for a frequency range 250 Hz < f_o < 600 Hz by placing the hot-wire at the center of the burner. To minimize Fourier transform errors such as leakage, the sampling frequency and the number of samples collected varied depending upon the frequency. For a given frequency f_o, the sampling rate was set to $10f_o$ and the total number of points collected set to $100f_o$.

This way, at each frequency, the FFT has a frequency resolution set at 1 Hz when computed using 10 ensembles.

The relationship between input (function-generator) voltage and output acoustic velocities for a few frequencies are plotted in Figure 3.3.4. Polynomial curve fits through the points are also drawn.

Some experiments required excitation at various frequencies with fixed excitation amplitude. In such a situation, the input voltages that would yield these amplitudes were computed from the curves by interpolating from the fitted curve.

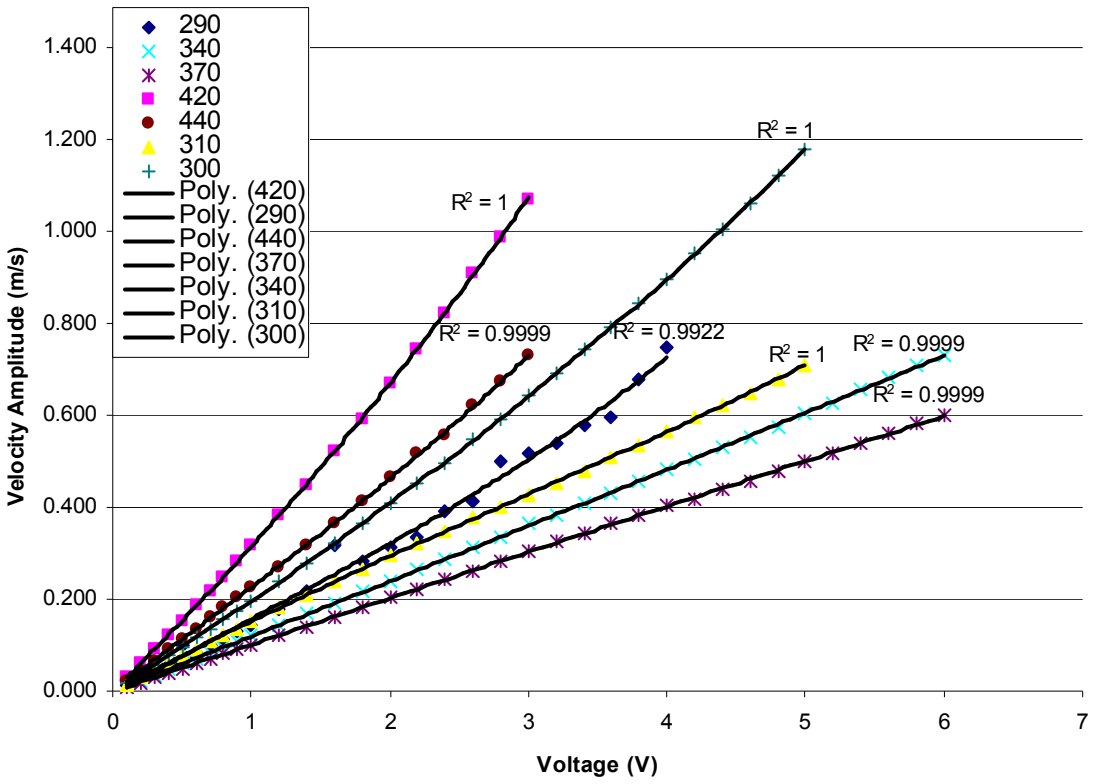

Figure 3.3.4: Plot of velocity-voltage amplitude transfer function, at different frequencies.

3.4.Particle Image Velocimetry

The velocity field was characterized with particle image velocimetry. This is a standard technique and is discussed in detail in literature, see Raffel *et al.* (1998). The details of this technique, unique to the present work are described next.

3.4.1. Details of the apparatus

A dual head 532 nm Nd:YAG laser with a peak power output of 120mJ/pulse was used as the light source. The interval between the beam pulses was varied between 25 – 60 μs depending on the flow speed. The light sheet was generated using two cylindrical lenses of 150 and 1000 mm focal length. The latter was used to reduce the thickness of the beam and the former was used to diverge the 5 mm laser beam to a height of 40 mm.

A 1600x1200 pixels CCD camera, with an F-mount Nikon 55mm micro-lens with an aperture of f/5.6 was used for imaging. The distance between the imaging plane and the camera was set at 12 inches.

Phase synchronization of the excitation signal with the PIV system was managed by a LaVision timing generator. At each phase, 128 images were recorded and the resulting data was ensemble averaged to provide velocity data repeatable to within 2% of its reported value.

The velocity vectors were processed from the raw seeding images using DaVis 7.0 commercial software. The field of view varied between 37mm and 50 mm in the axial direction depending upon the diameter of the bluff body imaged and was split into interrogation regions of 64 x 64 pixels, with a 50% overlap.

Vorticity values were computed using TECPLOT 360, from the velocity data. The uncertainity estimates in the vorticity are described in §3.4.3.

3.4.2. Computation of vorticity decay downstream

This section provides more details of the peak averaged method that will be used in Chapter 5, to compute vorticity decay rates.

For a vorticity image obtained at any given phase (Figure 3.4.1 as an example) say N vortices are spotted. The position and (maximum) vorticity characteristic of each vortex from 128 images obtained at that phase are then grouped into sets as follows:

$$\begin{bmatrix} \{(x_{1,1},\omega_{1,1}),(x_{1,2},\omega_{1,2})\ldots(x_{1,128},\omega_{1,128})\} \\ \{(x_{2,1},\omega_{1,1}),(x_{2,2},\omega_{1,2})\ldots(x_{2,128},\omega_{2,128})\} \\ \vdots\vdots\vdots\

Here ω represents the total vorticity, i.e. ($\omega = \Omega + \omega'$), where ω' and Ω denote the fluctuating and mean vorticity, respectively. The mean vorticity decreases along the shear layer as shown in Figure 3.4.2. Given that the vortex randomly visits different locations in space, i.e. locations with different values of mean vorticity, the amplitude (ω'), position ($<x>$) and fluctuation in position (x_σ) of the N^{th} vortex are calculated using the following formulae:

$$\omega'_N = \frac{\sum_{j=1}^{128}\left(\omega_{N,j} - \Omega(x_{N,j})\right)}{128}$$

$$< x >_N = \frac{\sum_{j=1}^{128} x_{N,j}}{128}$$

$$x_{\sigma,N} = \sqrt{\frac{\sum_{1}^{128}\left(x_{N,j} - < x >_N\right)^2}{128}}$$

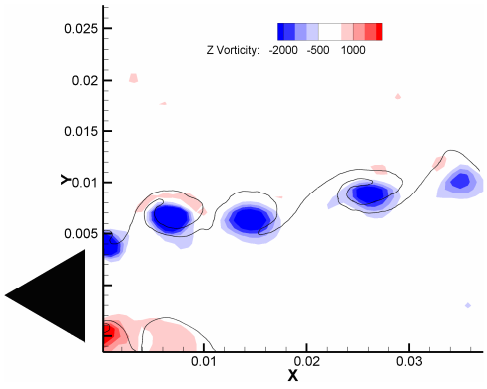

Figure 3.4.1: Sample illustration of instantaneous vorticity contours and flame sheet location. The bluff body is also shown in the figure, drawn to scale.

This process is repeated for the different phases at which measurements were obtained. The essence of the above formula (i.e. for ω'_N) is the fact that vorticity

amplitudes are averaged, as opposed to averaging the total vorticity first and then subtracting the mean vorticity from an averaged position.

For completeness, it should be mentioned that for each of the *N* vortices, out of 128 images, not all the *N* vortices could be identified each time in 128 images, especially for vortices far downstream, where the ratio of vorticity amplitude to mean vorticity was lower. For this reason a threshold of 50 points was set, below which the data point is not reported.

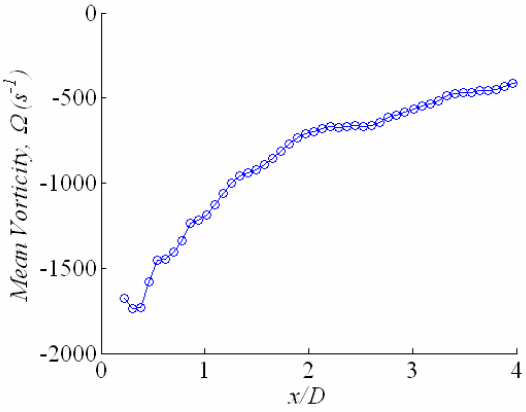

Figure 3.4.2. Mean vorticity variation along the shear layer plotted as a function of downstream distance.

3.4.3. Uncertainity estimates in vorticity computation

To estimate the uncertainty in vorticity without acoustic excitation, i.e. for the 'mean flow', three independent experiments were done where 128 samples were recorded, for each experiment. The vorticity was then computed for each of these and the standard deviation was computed at each spatial location. The results are plotted in Figure 3.4.3. This results in a maximum deviation of 5%.

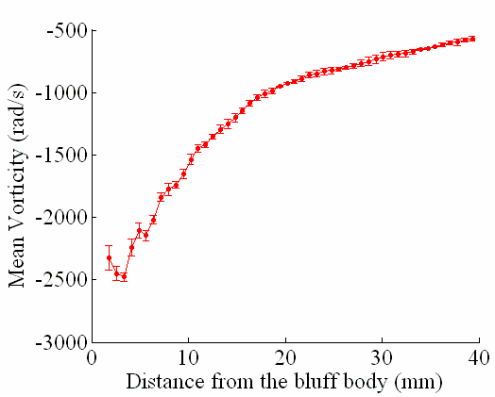

Figure 3.4.3: Uncertainity estimates in mean vorticity plotted at various points downstream.

To estimate the uncertainty in vorticity during acoustic excitation, the standard deviation in vorticity amplitudes were computed as per the equation:

$$\sigma_{\omega'_N} = \sqrt{\frac{\sum_{j=1}^{128}\left(\omega_{N,j} - <\omega'_N>\right)^2}{128}}$$

where the symbols have their usual meanings and are described in the earlier section.

The results are plotted in Figure 3.4.4. Figure 3.4.4a figure plots the standard deviation in vorticity values at each point as vertical bars. This uncertainty is also plotted as a percentage of its mean value in Figure 3.4.4b.

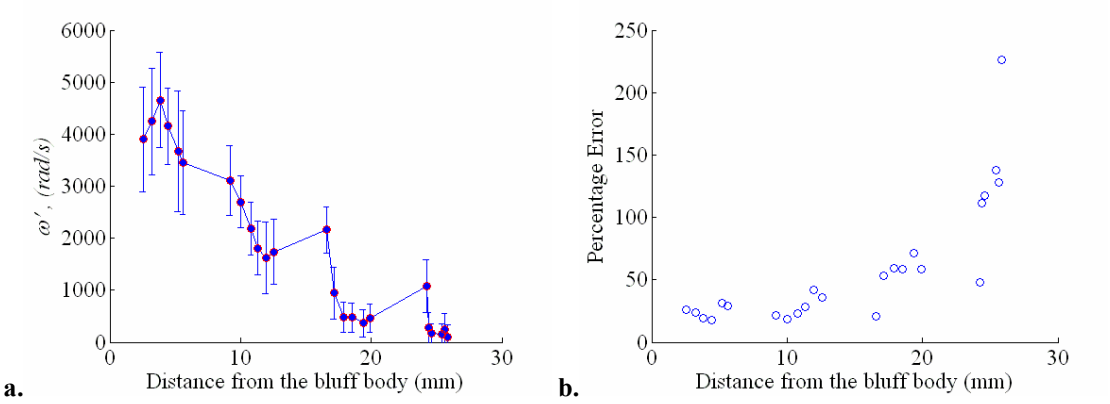

Figure 3.4.4: a. Plot of vorticity decay with uncertainty bars. b. Percentage error in vorticity estimation as a function of downstream distance.

CHAPTER 4

FLAME SHEET DYNAMICS OF BLUFF-BODY STABILIZED FLAMES DURING LONGITUDINAL ACOUSTIC FORCING

This chapter details the response of the flame to acoustic excitation. §4.1 begins by surveying the qualitative characteristics of the flame response. Next, the observed behavior, i.e. the spectral features and their spatial characteristics are quantified. Then, the focus is shifted towards understanding the parametric dependence of the flame response w.r.t. the amplitude and frequency of acoustic forcing. §4.2 presents the key features of the velocity field that lead to the observed behavior of the flame response. Based on these characteristics a comparison is made with the theoretical prediction of Shin and Lieuwen (2008) in §4.3. Finally, §4.4 discusses the behavior of the flame response at large amplitudes of excitation, i.e. when $u' = O(U_\infty)$.

4.1. Response of the Flame to Acoustic Excitation

To investigate the behavior of the flame under acoustic excitation, experiments were performed at mean and perturbation flow velocities of U_∞ =1.8 m/s and $0 < u'/U_\infty < 1.1$, respectively, where U_∞ is the centerline duct exit velocity in the absence of the bluff body. Disturbances were forced at six frequencies, f_o, between 130Hz and 240 Hz. These frequencies correspond to Strouhal numbers of $St_D = f_o D/U_\infty = 0.69$ - 1.27. The equivalence ratio was set to 0.8; this latter condition was chosen to provide a stable flame. These conditions correspond to $Re_D = 991$ and $Re_W = 9910$, where Re_D & Re_W are

the Reynolds numbers of based on the bluff body diameter and burner exit dimension respectively.

4.1.1. Qualitative Survey of Flame Motion

An instantaneous image, representative of an unexcited flame, is shown in Figure 4.1.1a. It can be seen that there are no *periodic* disturbances of the flame front (the field of view extends from 0.33D to 7D), although it does exhibit occasional, roughly symmetric, but non-periodic corrugations. Beyond the field of view too, no coherent motion of the flame front was observed in course of the experiments.

As acoustic forcing is introduced, the presence of periodic distortions of the flame front, due to the roll-up of shear layer into coherent structures, is evident in the flames. Typical images of the flame for several forcing levels are shown in Figure 4.1.1. Evident are discrete, periodic structures (Figure 4.1.1b-d), whose amplitudes are dependent on the amplitude of the excitation. The roll up of the flame by the structures is particularly evident at higher forcing amplitudes near the flame base. The period of formation of these structures is exactly commensurate with that of the acoustic excitation, f_o. A frame by frame inspection of these images also reveals the convection of these structures along the flame front, in the direction of the mean flow.

Next, consider image Figure 4.1.1d. A horizontal dotted line is placed in the middle of the figure, for reference. Below this line, the rollup of the flame on either side of the flame possess a good degree of symmetry and the spacing between these structures (indicative of the wavelength) is also well defined. In contrast, above the reference line, no rollup is seen; only cusping, indicative of destruction of flame surface area occurs. The spacing between the structures is also less regular. The images suggest that the

dotted line represents a threshold, below which, the growth of flame corrugations by these flow structures is dominant. Above this line, the amplitudes of corrugations decreases, indicating that the underlying velocity field causing these wrinkles has dissipated and the flame is relaxing back to its normal, unforced shape. This occurs due to kinematic restoration, a nonlinear process that leads to destruction of flame area; hence the cusping.

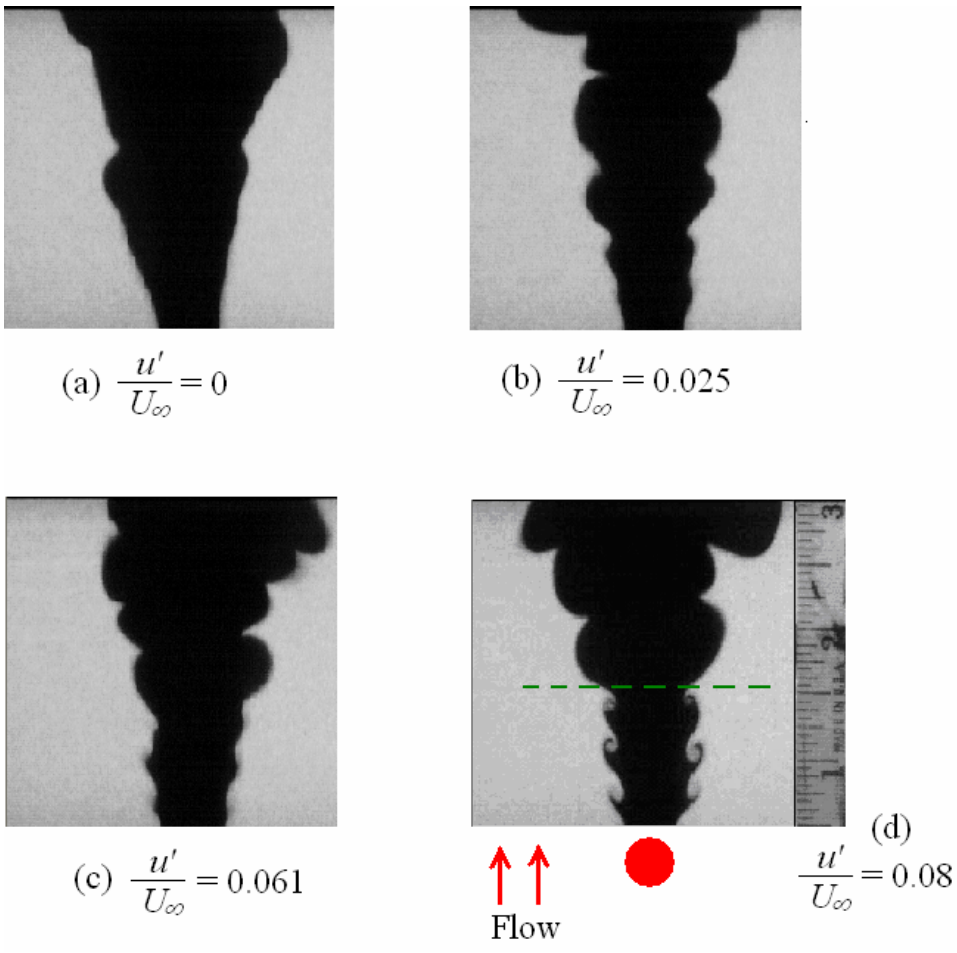

Figure 4.1.1: Instantaneous Mie-scattering images of flame structure. (a) No external forcing, (b)-(d) increased driving; the amplitudes of excitation are indicated below each figure. Flow direction is from bottom to top as indicated. The position of the bluff body is also shown for reference, drawn to scale. The scale on the right of image (d) measures in inches. Conditions: U_∞ = 1.8 m/s, D = 9.52 mm and ϕ = 0.8, circular bluff body. For the excited case, f_o =150 Hz, , u_a'/ U_∞ = 0.05

These observations will be quantified in the next section. However, before proceeding further, some attention is devoted to provide a qualitative understanding for the two-dimensionality of the problem. This can be studied by the cross stream visualization as shown in Figure 4.1.2a, obtained by rotating the laser sheet to be perpendicular to the flow direction. In this figure two instantaneous images are presented, which were taken at the same conditions and at the same distance downstream from the bluff body, but at different instances of time. In both the pictures a defocused metallic object runs through the black (product) region; this is the image of the bluff body.

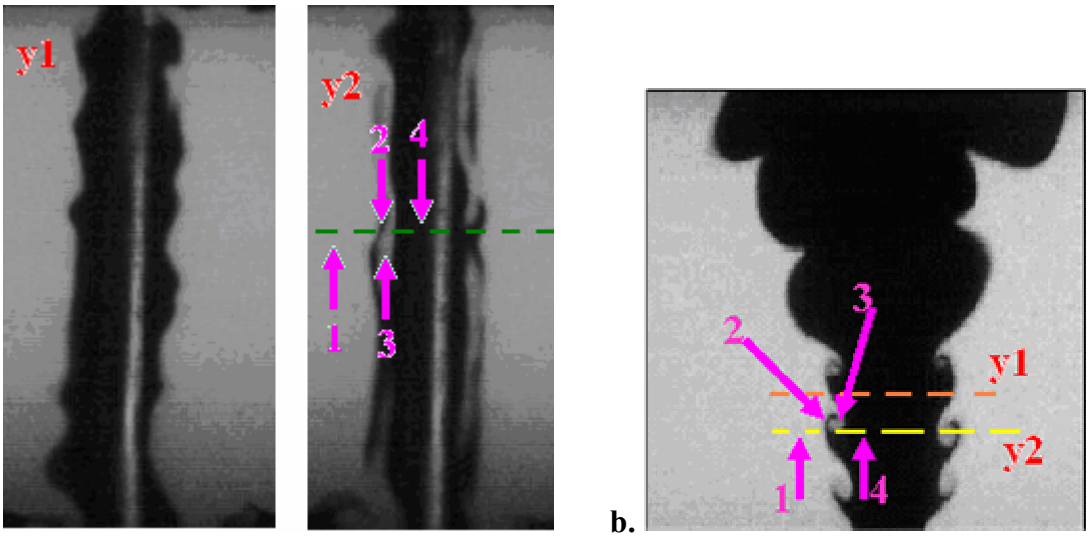

Figure 4.1.2: a. Two instances of span wise variation (at y/D = 3) of the flame front corrugation. For these images, flow direction is normal to the plane of the paper, towards the reader. Rollup of the flame is evident in the right image. b. Reference image (in which the flow is from bottom to top) marking the location of the horizontal slices. Conditions: f_o = 130 Hz, u'/U_∞ = 0.06, D = 9.52 mm and ϕ = 0.8, circular bluff body.

Figure 4.1.2a shows two different kinds of features. In Figure 4.1.2a(left), moving from left to right along any horizontal slice will move us from the gray region (reactants) to the black region (products) and back again into the reactants. This is not the case for Figure 4.1.2a (right). As an example, consider moving along the horizontal dashed line, where one encounters multiple transitions from reactants to products. To explain the

latter image better, Figure 4.1.2b plots the downstream locations, labelled as $y1$ and $y2$ which are representative of the slices shown in Figure 4.1.2a. Notice that, moving along location $y1$ (from left to right) of Figure 4.1.2b, one encounters reactants, products and then reactants again. Thus, one encounters a situation similar to Figure 4.1.2a(left). As regards Figure 4.1.2a (right), consider the dashed line in that image, and the slice $y2$ shown in Figure 4.1.2b. The corresponding locations between these two images are labeled 1 - 4. Starting at location 1, the point is located in the reactants. Moving to the right, at point 2, one then encounters a very narrow region of products. Moving slightly to the right one encounters region 3, which is a region of reactants into which the flame is trying to burn. Finally, region 4 is the product region outside the shear layer. Now, if an observer is at a fixed location, say $y1$ in Figure 4.1.2b, after some instance of time the layer $y2$ is convected upwards by the flow towards station $y1$; hence the observed transition from Figure 4.1.2a(left) to Figure 4.1.2a(right).

To revisit the issue of the degree of two-dimensionality, once can readily see from both images of Figure 4.1.2a ,that although some wrinkles are present along the span, these do not occur at well defined wavelengths and are more or less random in nature. Thus, for all practical purposes, the assumption of the flame front fluctuations being two-dimensional is, on average, reasonable.

We close this section by presenting instantaneous images of the perturbed flame at two different approach flow velocities, all other conditions being identical, see Figure 4.1.3. Comparing the two images one can see that the spacing between the structures has increased for the higher velocity case. This suggests that *the perturbation field that controls the flame response has convective characteristics*, despite the source of

excitation being acoustic. As such, the wavelength of these structures increase with increases in velocity or decreases in frequency, since $\lambda_c = U_\infty/f_o$. Second, notice that in Figure 4.1.3 (left) the rollup of the flame persists up to three convective wavelengths, and cusping starts at four wavelengths downstream. In contrast, in Figure 4.1.3 (right), cusping of the flame fronts are seen within two convective wavelengths. Part of this is because, as the velocity is changed, the most amplified mode of the shear layer shifts to a different value. Therefore, even if the two cases are forced at the same frequency and excitation level, the excitation level of the perturbation field of interest, i.e. the convective perturbation field, will be different. This observation, along with the amplitude dependence of the flame response highlighted in Figure 4.1.1, demands a quantitative understanding of the flame response and its parametric dependencies. This is discussed in the next section.

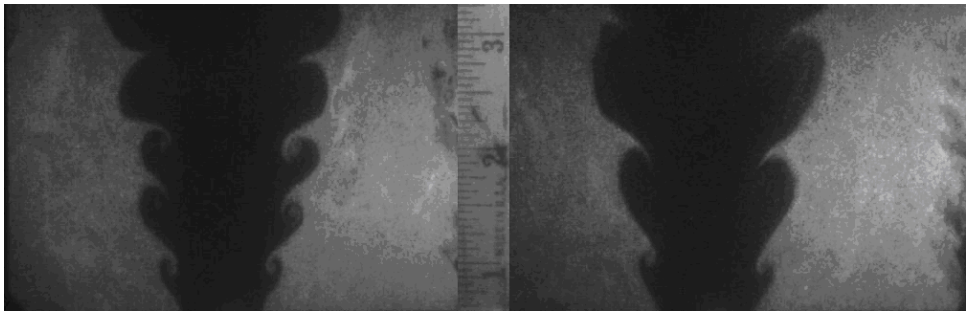

Figure 4.1.3: Instantaneous images of flame position for two different mean velocities, U_∞ = 2.27 m/s (left) and U_∞ =3.37 m/s (right), All other conditions are identical: f_o = 150 Hz, u' = 0.14 m/s and D = 12.7 mm. The scale placed in the middle of the picture measures in inches.

4.1.2. Spatial and Spectral Characteristics

This section presents a quantitative analysis of the flame front fluctuations at various conditions, using techniques described in §3.2.

4.1.2.1. Basic Characteristics

A sample flame front signal, with and without acoustics is illustrated in Figure 4.1.4a. Notice that during excitation, a clear peak is seen at the frequency of forcing. The amplitude of this peak exhibits a spatial dependence, discussed further in this section. In contrast, in the absence of excitation, the spectrum lacks any discrete spectral features and is more broadband in nature, at least within the highest frequency that can be resolved ($f_{Nyquist}$ = 250 Hz, corresponding to St_D = 1.3). Moreover, the amplitude of these fluctuations grows downstream leading to a monotonically growing flame brush as shown in Figure 4.1.4b, an observation also noted by Bédat and Cheng (1995), Knaus and Gouldin (2000) and Williams *et al.* (1951).

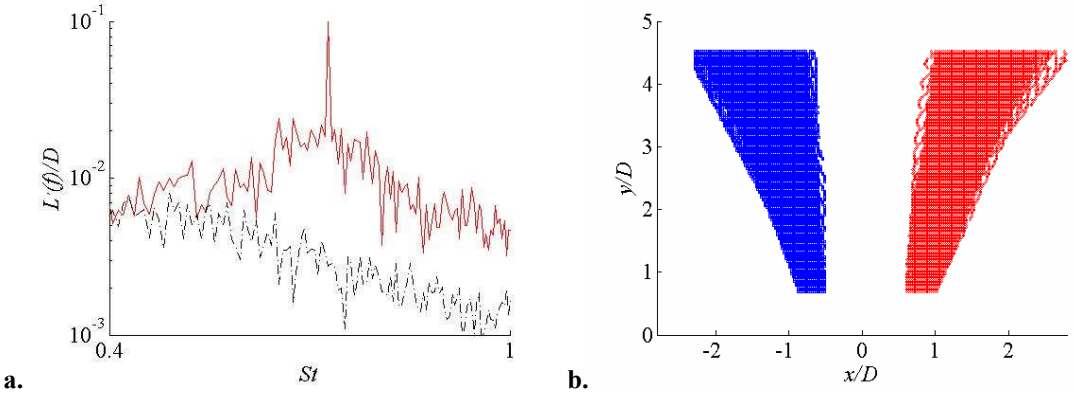

Figure 4.1.4: a. Typical spectrum of the flame front fluctuations, with (solid line) and without (dashed line) acoustic excitation. A distinct peak is seen at the frequency of excitation. b. Flame brush development downstream, in the absence of acoustic excitation. This image is obtained by the superposition of 2048 flame front positions. Conditions: U_∞ = 1.8 m/s, D = 9.52 mm. For the excited case, f_o =130 Hz, , u_a'/ U_∞ = 0.05 and ϕ = 0.8, circular bluff body.

To understand the spatial evolution of the flame response, typical amplitude characteristics of flame-front position spectra under the influence of acoustic excitation are shown as a three-dimensional plot in Figure 4.1.5. This figure plots the spectra at seven downstream locations. The downstream location is normalized by the convective

wavelength of the flame front disturbances, $\lambda_{cf} = U_\infty / f_o$, which approximately equals the distance a disturbance propagating at the mean flow velocity travels in one acoustic period. The envelope of the flame response at $f = f_o$ is also drawn. Close to the bluff body, the flame responds chiefly at the frequency of excitation (f_o). Moving downstream, the response[2] first grows, reaches a maximum, and then decreases. This behavior is due to the growth and decay of the underlying flow structures as well as the propagation of the flame, which tends to smooth out the wrinkles. These results are consistent with other data, e.g. Hegde *et al.* (1987), though they have apparently not been explicitly stated or discussed.

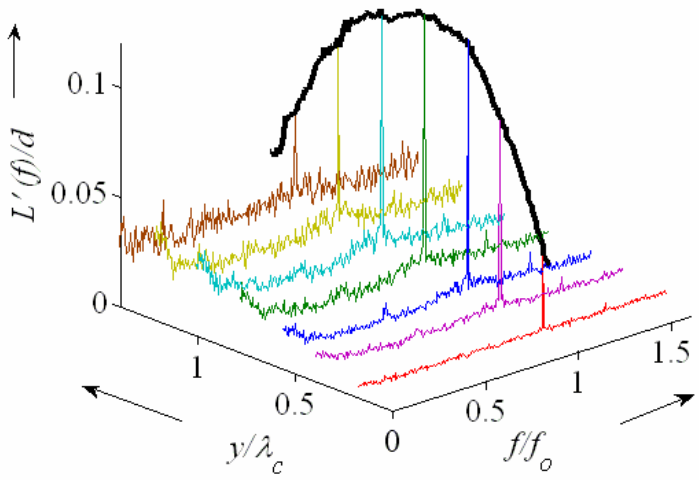

Figure 4.1.5: Spectrum of flame sheet fluctuations, $L'(y,f_o)$ at different downstream locations (U_∞ = 4.5 m/s, f_o = 300 Hz, D = 9.52 mm, u_a'/U_∞ = 0.05 and ϕ = 0.67, triangular bluff body).

The spectrum also exhibits a monotonic increase in broadband fluctuations with downstream distance. This reflects the random flapping of the flame brush, which increases in magnitude with downstream axial distance, as is clearly seen for the unforced

[2] From this point forward, the flame response will refer to the response at $f = f_o$, unless stated otherwise.

case, see Figure 4.1.4b. In addition, tiny peaks are also noticed at f/f_o = 0.5 and 1.25. The dynamics of the flame response at frequencies other than the frequency of excitation is discussed in §4.4.

To understand the parameters that govern the spatial dependence of the flame response, consider Figure 4.1.6. Figure 4.1.6a plots the flame response at different frequencies but at a fixed amplitude of excitation. Figure 4.1.6b plots the flame response for different amplitudes of excitation. Immediately, it is seen that the growth rate, decay rate, and peak amplitudes of these flame disturbances exhibit both, an amplitude and frequency dependence. Note that in two higher frequency cases, f_o = *130 Hz* and *230* Hz, the maximum in flame response is not captured and presumably occurs at a lower height. The decay rate in flame response is faster at the higher frequencies. For instance at f_o = *230 Hz*, all traces of any flame front fluctuation at the frequency of forcing is absent beyond $y>1.8\lambda_c$. In contrast, at f_o = *130 Hz*, the flame response persists till $y=4\lambda_c$.

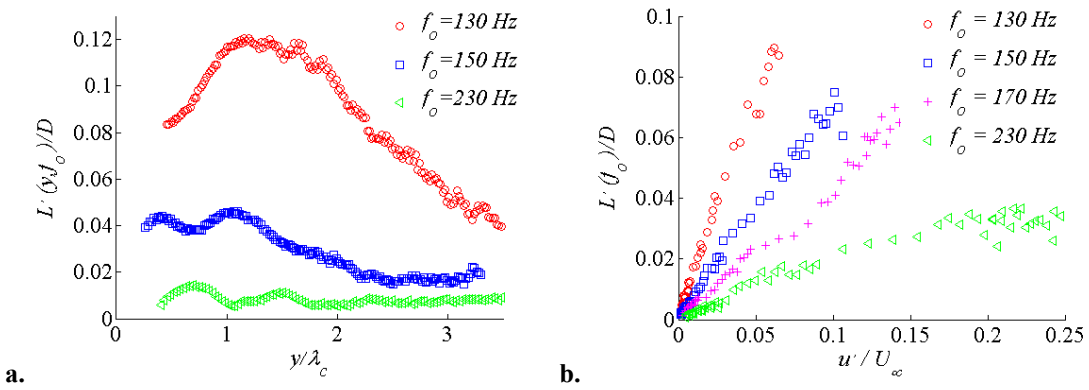

Figure 4.1.6: a. Illustration of flame response as a function of the frequency of excitation, at identical excitation levels (u'/U_∞ = 0.05). b. Dependence of flame front movement amplitude upon disturbance amplitude. Conditions: D = 9.52 mm, ϕ = 0.8, U_∞ = 1.8 m/s, circular bluff body.

Another view of forcing amplitude and frequency effects is shown in Figure 4.1.6b, which plots the flame response as a function of perturbation amplitude at a fixed

height. First, note the low pass nature of the flame response, as the slope of the response *vs*. forcing amplitude curve monotonically decreases with increases in frequency. Some care must be taken in quantitatively comparing these slopes, due to the modulated nature of the amplitude shown in Figure 4.1.6a (f_o = *150 & 230Hz*). This result would be expected for disturbances with a purely kinematic origin, e.g., see Preetham and Lieuwen (2004, 2005) . Another significant observation is that the flame response is proportional to the perturbation amplitudes- i.e., there does not appear to be some "threshold lock-in" amplitude, at which the response is initiated. This result would be expected if the disturbance field perturbing the flame is convectively unstable or the disturbance field arises from purely kinematic processes, due to the monotonically increasing fluctuation in flame angle at the stabilization point with disturbance amplitude.

In addition to the magnitude of the flame-front fluctuations, the phase was also computed and analyzed. Representing a convecting disturbance field as:

$$L'(y,t) = \sum_f L'(y,f)e^{i(\omega t - ky)}$$

Then, consider the phase of the flame-front fluctuations at the frequency of excitation:

$$\Psi = ky = \frac{2\pi}{\lambda_c} y$$

where, $\lambda_c = U_c / f_o$; U_c being the convection speed. Thus, if $U_c = U_\infty$, then any plot of Ψ *vs.* y/λ_c should possess a slope of 2π.

Figure 4.1.7a plots the phase of the flame-front fluctuations for a range of frequencies at two different velocities. For all cases, a linear variation is captured. Such a variation indicates a constant axial convection speed of these flame sheet disturbances, independent of the frequency of excitation. This convection speed is also independent of

the amplitude of excitation, see Figure 4.1.7b. From the slope of this graph, the convection speed was calculated to be $U_c = 0.84U_\infty$.

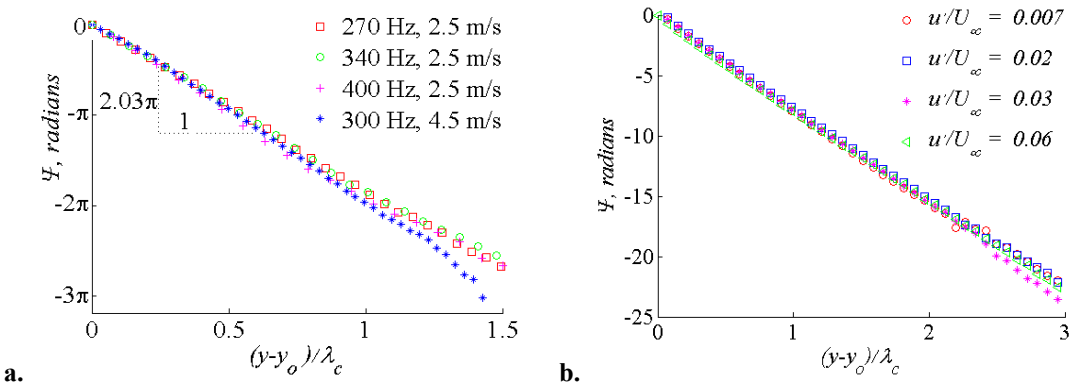

Figure 4.1.7: a. Phase dependence upon normalized axial location, where y_o indicates first axial location where data was obtained. Conditions: D = 9.52 mm, u'/U_∞ = 0.05 and ϕ = 0.67, triangular bluff body. b. Phase dependence upon normalized axial location for different amplitudes of excitation, all other parameters being same. Conditions: D = 9.52 mm, f_o = 130 Hz, u'/U_∞ = 0.05, ϕ = 0.8, U_∞ = 1.8 m/s, circular bluff body.

Experiments were also conducted to study the convection speed as a function of equivalence ratio. The results are shown Figure 4.1.8. Notice that as the equivalence ratio is varied from $0.69 < \phi < 0.75$ the convection speed increases slightly from $U_c = 1$ at ϕ = 0.69 to $U_c = 1.09$ at $\phi = 0.75$.

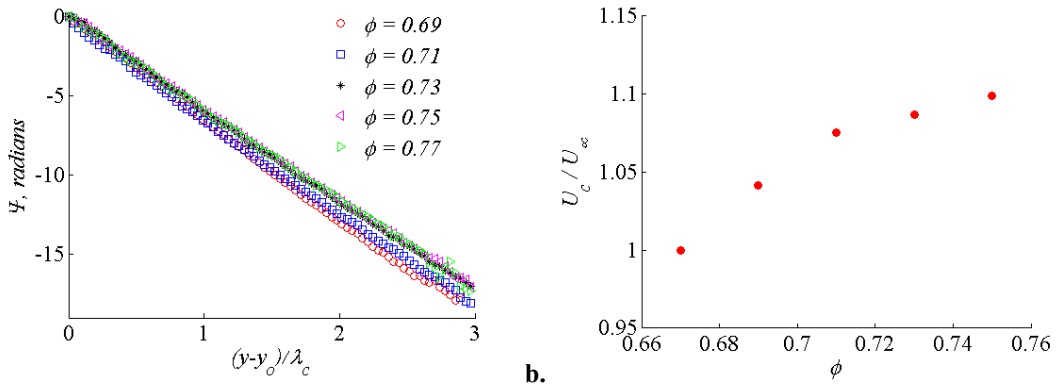

Figure 4.1.8: a. Phase dependence upon normalized axial location, where y_o indicates first axial location where data was obtained. b. Dependence of convection velocity upon equivalence ratio. Conditions: D = 9.52 mm, U_∞=3.37 m/s, u'/U_∞ = 0.0044, circular bluff body.

In summary, the convection speed was analyzed to be independent of magnitude of acoustic excitation, frequency and mean velocity. It however, depends on the equivalence ratio and the bluff-body shape, a variation bounded as $0.8 < U_c/U_\infty < 1.1$. As such, this depends on the appropriate choice of mean velocity U_∞.

So far, the flame response, L', has been studied for a range of conditions. This is related to the local heat release as $Q' = \sin\alpha \dfrac{\partial L'(y,t)}{\partial y}$ where α is the angle between the flame front and the flow direction. In terms of $L'(y,f_o)$ this can be rewritten as $Q' = \sin\alpha \sqrt{\left(\dfrac{\partial L'(y,f_o)}{\partial y}\right)^2 + \dfrac{4\pi^2}{\lambda_c^2}\left(L'(y,f_o)\right)^2}$.

4.1.2.2. Processes Controlling the Flame Response

Having explored the basic characteristics of the flame response, i.e. that it increases and then decreases, we shall now try to explain its key factors and the processes that lead to it.

Figure 4.1.9a plots the dependence of the amplitude upon normalized axial distance at three excitation amplitudes, but all other conditions remaining equal. Figure 4.1.9b plots these same data, with the *y*-axis normalized by the acoustic excitation amplitude. The plot can be divided into two regions manifested by "growth" and "decay" of the flame sheet oscillations. This plot shows that the flame response increases linearly with excitation amplitude in the bluff body nearfield, or "growth" region, as manifested by all the curves in the right plot converging onto a single line. However, farther downstream, the flame dynamics are clearly nonlinear, as is evidenced by the fact that in the decay regions, the curves intersect each other (see the region labeled 'decay', Figure 4.1.9a). In the amplitude normalized response plots they diverge with increasing axial distance. In particular, the saturation in flame response can be seen, indicating that the maximum in flame response, as well as response farther downstream, does not grow proportionally with amplitude.

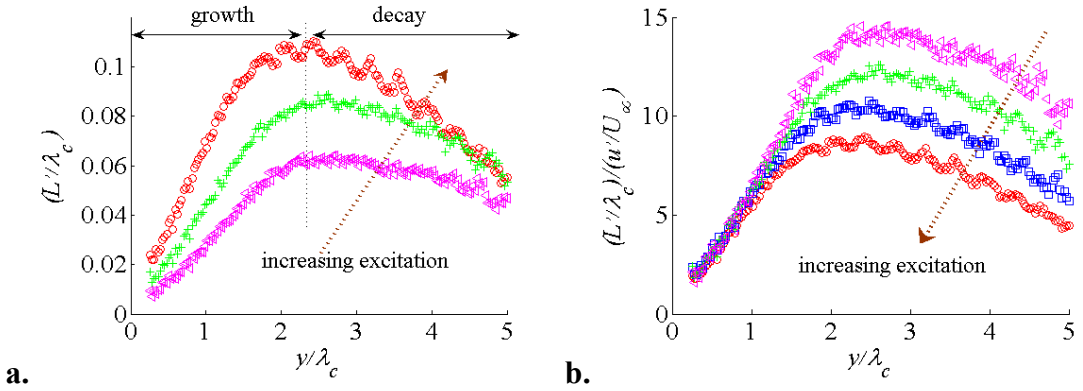

a. **b.**

Figure 4.1.9: a. Measured dependence of flame sheet amplitude response upon normalized axial distance, $\lambda_c=U_\infty/f_o$, b. Same curve, but amplitude normalized by acoustic velocity amplitude. Legend: (o) u'= 0.028, (□) u'= 0.021, (+) u' = 0.016, (◁) u' = 0.010. Other conditions: U_∞ = 2.27 m/s, D = 12.7 mm, f_o = 150 Hz, cylindrical bluff body.

The data presented in Figure 4.1.9a shows that the flame response first grows with downstream distance, up to an axial location of $y/\lambda_c = 2.2$, before decaying. This initial increase in L' with y is due to the flame anchoring; i.e., regardless of the perturbation, the flame attachment point remains largely fixed. As such, the amplitude of L' must start from zero or near zero. Obviously, it will not remain zero at $y > 0$, since it is being perturbed by the fluctuating velocity field – hence the initial increase in L' with y. Even if the flame attachment point vibrates some, i.e., $L'(y=0,t) \neq 0$, as long as the flame base does not move in phase and with the same amplitude as the flow field, similar behavior occurs. Furthermore, because the amplitude of fluctuations in the y~0 region are so small, nonlinear effects are negligible. These nonlinear effects are contained in the $S_L |\vec{\nabla} G|$ term, which describes flame propagation normal to itself.

The peaking and subsequent reduction in amplitude of flame response shown in Figure 4.1.9 is the result of flame propagation normal to itself, which destroys flame wrinkles – a nonlinear effect (Law and Sung 2000). Moreover, for a thermo-diffusively stable flame, unsteady curvature effects also work to destroy flame wrinkles – even at first order in perturbation amplitude – due to the increase in flame speed at locations concave to the flow and vice versa (Preetham 2007). If the perturbation velocity persisted indefinitely downstream, at some point the flame wrinkle excitation and destruction processes would equilibrate, leading to a roughly constant (or oscillating) amplitude of flame perturbation with downstream distance. However, the amplitude of the excitation field decays with downstream distance (shown in §4.2). Hence, the amplitude of flame wrinkling decays.

The trends explained up to this point are also seen at a variety of other conditions. These are plotted in Figure 4.1.10. Figure 4.1.10a plots the flame response at the same mean flow conditions as Figure 4.1.9 but different excitation conditions (f_o =180 Hz for Figure 4.1.10a *vs.* f_o =150 Hz for Figure 4.1.9). On the other hand, Figure 4.1.10b and Figure 4.1.9 have identical excitation conditions but different mean flow conditions.

Data from all these three plots are encapsulated in Figure 4.1.11. From this, one can see that across a range of conditions, the basic features of the flame response are the following:

a. $L' \rightarrow 0$ as $y/\lambda_c \rightarrow 0$. Stated differently, the flame does not move near the base of the bluff body.

b. In a region close to the base, the growth rate of the flame response is proportional to the amplitude of excitation, i.e. in this region $(L'/\lambda_c)/(u'/U_\infty)$ = constant.

c. At some region in space, the flame response peaks. Beyond this region, kinematic restoration, a non-linear process, controls the flame reponse.

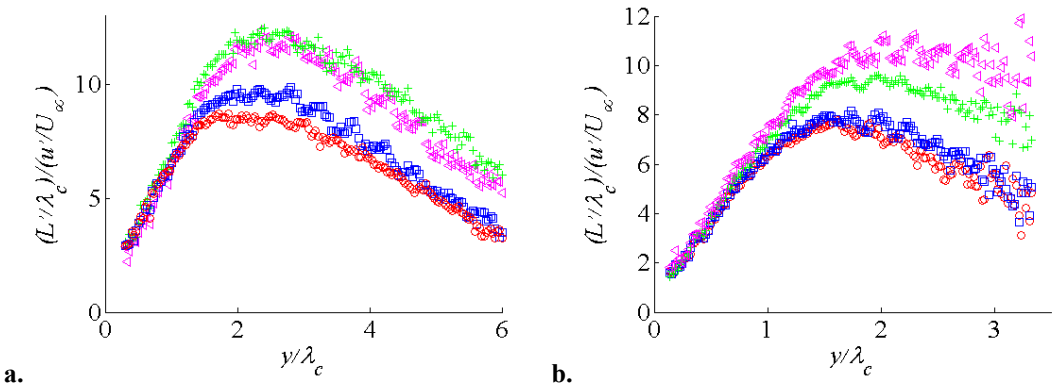

Figure 4.1.10: a. Illustration of near-field scaling of the flame response. Legend: (o) *u'*= 0.033, (□) *u'*= 0.026, (+) *u'* = 0.018, (◁) *u'* = 0.015. Other conditions: U_∞ = 2.27 m/s, *D* = 12.7 mm, f_o = 180 Hz, cylindrical bluff body. b. Legend: (o) *u'*= 0.028, (□) *u'*= 0.021, (+) *u'* = 0.016, (◁) *u'* = 0.010. Other conditions: U_∞ = 3.37 m/s, *D* = 9.52 mm, f_o = 150 Hz, cylindrical bluff body.

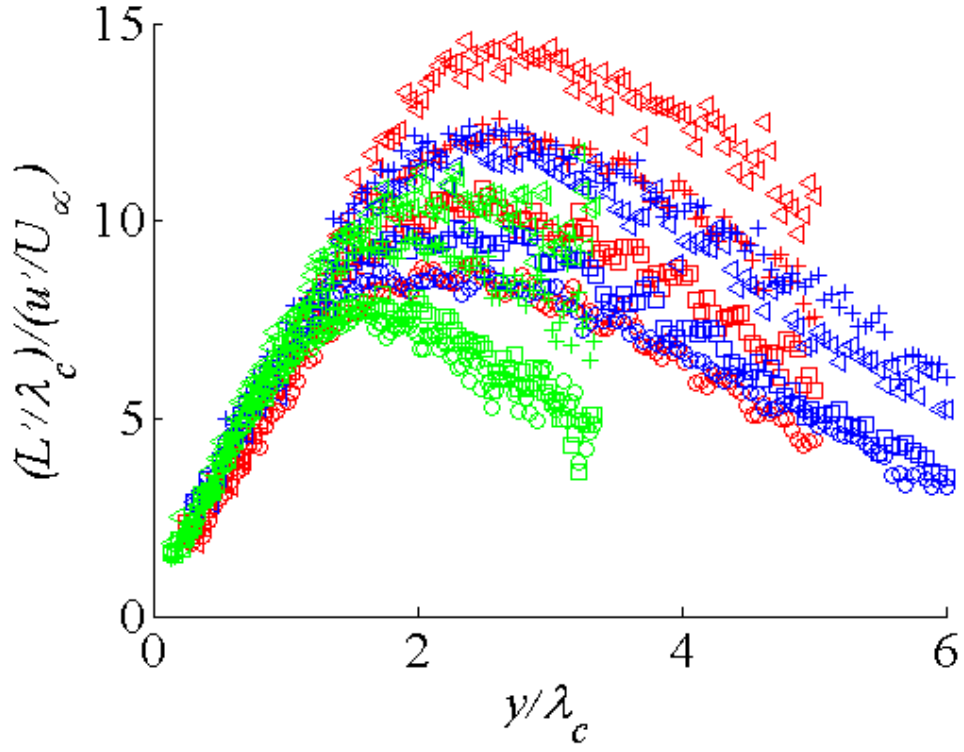

Figure 4.1.11: Combined data from various experiments, comparing the near-field scaling of the flame response. Legend: (RED) (o) *u'*= 0.028, (□) *u'*= 0.021, (+) *u'* = 0.016, (◁) *u'* = 0.010; U_∞ = 2.27 m/s, *D* = 12.7 mm, f_o = 150 Hz (BLUE) (o) *u'*= 0.033, (□) *u'*= 0.026, (+) *u'* = 0.018, (◁) *u'* = 0.015; U_∞ = 2.27 m/s, *D* = 12.7 mm, f_o = 180 Hz (GREEN) Legend: (o) *u'*= 0.028, (□) *u'*= 0.021, (+) *u'* = 0.016, (◁) *u'* = 0.010; U_∞ = 3.37 m/s, *D* = 9.52 mm, f_o = 150 Hz. For all these cases experiments were conducted on a cylindrical bluff body.

4.2.Characteristics of the Disturbance-Field Perturbing the Flame

Having discussed the basic features of the flame response, this section shifts the focus to uncover some characteristics of the velocity/vorticity field that is perturbing the flame. This will help us justify the observed characteristics of the flame response.

The perturbation field leading to the flame response shown in Figure 4.1.5 is plotted in Figure 4.2.1 for identical conditions. This figure plots the vorticity field at one phase, as a function of space. Notice how the vorticity field is concentrated into discrete blobs whose strength decreases as one moves downstream. This figure reveals two things. First, the excitation source, i.e. the acoustic field, results in a spatially periodic vorticity field. It is this vorticity field that perturbs the flame as opposed to the acoustic field, which is the source of excitation. Hence, the presences of vortical like structures as shown in Figure 4.1.3 and Figure 4.1.1d. Second, vorticity decays in space. Hence the decay of the flame response.

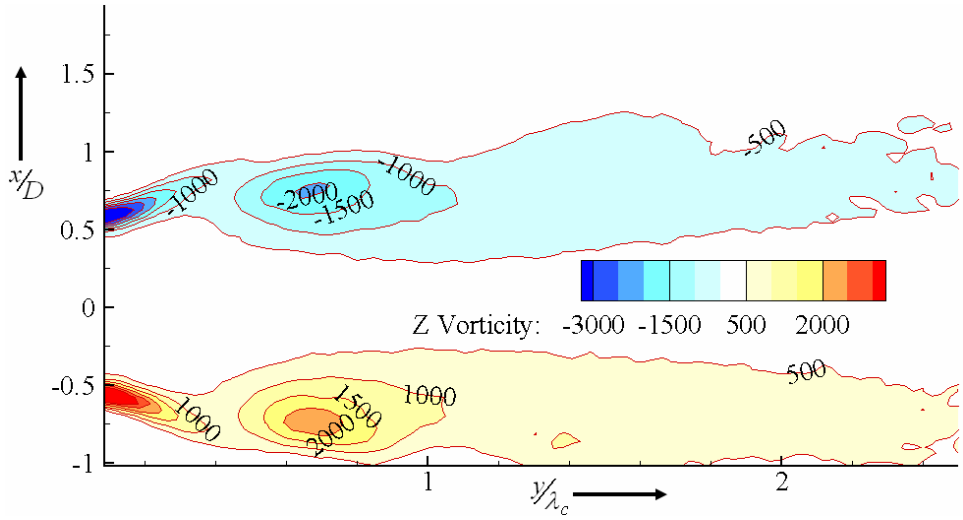

Figure 4.2.1: Contour plot of the vorticity field perturbing the flame (ensemble averaged data, phase=45^{o} *w.r.t.* excitation). Conditions: U_{∞} = 4.5 m/s, D = 9.52 mm and ϕ = 0.67, triangular bluff body.

We now turn our attention to explain the behavior of the flame in the near field (as $y/\lambda_c \rightarrow 0$). To better understand this, consider Figure 4.2.2. This figure plots the axial velocity profiles at four downstream locations. If one is in situated at, say $x/D = 1.5$, one will encounter a uniform free stream velocity on either side. As x/D reduces, at some point, one encounters the velocity gradient, a region in which the velocity reduces from its free-stream value to zero. This region of velocity gradient is the shear layer and is of most interest. In Figure 4.2.2 this zone is marked by solid black lines. It is within this region that the point $U(y) = S_L$ exists, where the flame is stabilized.

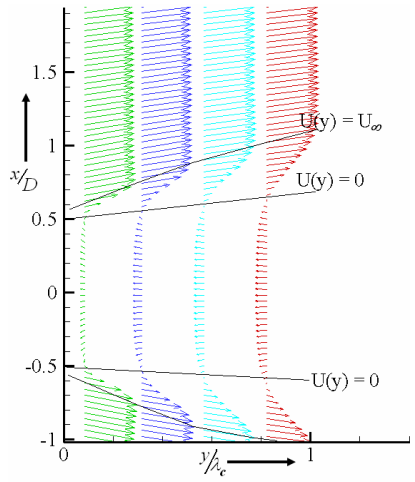

Figure 4.2.2: Velocity profiles at four downstream locations. Also shown are the loci of the points where $U(y) = 0$ & $U(y) = U_\infty$ for both the shear layers. Conditions: U_∞ = 4.5 m/s, f_o = 300 Hz, D = 9.52 mm, u'/U_∞ = 0.05 and ϕ = 0.67, triangular bluff body.

Close to the bluff body, the shear layer is very thin. However, as we move downstream, the shear layer widens. Hence, if any perturbation is applied to the flame, it has almost no space to move close to the bluff body, but ample space downstream. Figure 4.2.1 reinforces this point for the case when the acoustic field is present. Notice that in this figure, close to the bluff body, the high vorticity regions are densely packed within a narrow region, which expands as we move downstream. Another way of seeing this is by

following the $|\omega|$= 500 contour. Analyzing this contour along vertical slice shows that this zone increases as we move downstream.

This very structure of the shear layer, or the 'boundary condition' is what leads to $L' \rightarrow 0$ as we approach the bluff body base. This constraint is reduced as we move away from the bluff body. This coupled with the fact that the perturbation field keeps supplying oscillations, leads to L' increasing as we move away from the bluff body.

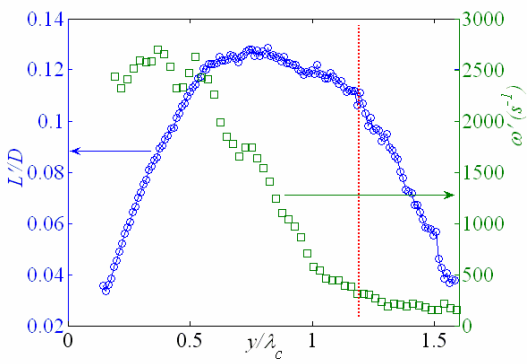

Figure 4.2.3: Spatial evolution of the flame response (○) and the vorticity field (□). Conditions: U_∞ = 4.5 m/s, f_o = 300 Hz, D = 9.52 mm, u'/U_∞ = 0.05 and ϕ = 0.67, triangular bluff body.

Next, to understand the nature of the growth and decay regions (as was first mentioned in Figure 4.1.9), the envelope of the vorticity and flame response for identical conditions are plotted in Figure 4.2.3. This figure shows that the strongest perturbations are supplied at the base of the bluff body. The flame is supplied with oscillations, continuously, in space, until the vorticity field completely decays. All along, the flame tries to kinematically restore itself to its mean state. Clearly, this effect will be small close to the bluff body where the vorticity is the strongest. Nevertheless, at some point downstream, when the excitation source of the flame is weak, kinematic restoration starts to become dominant. Hence, the flame response peaks and starts to decay thereafter, despite the oscillations still being present. This can be seen in Figure 4.2.3, at $y/\lambda_c \sim 0.75$,

which shows that the flame response starts to decay even before the vorticity field has decayed completely.

Finally, note that even if the vorticity field has decayed (shown by the dotted red line in Figure 4.2.3) the flame response is non-zero. This is simply because of the convection of residual wrinkles on the flame front. That is, kinematic restoration is not an instantaneous process; as the flame restores itself, the wrinkles convect downstream too.

4.3.Comparison with Theory

Shin and Lieuwen (2008) conducted a theoretical analysis on acoustically excited bluff body flames, where they use the G-equation to study the response of flames. Details of their predictions can be found in Appendix B. Based on their analysis, they predict the growth of the flame response using the following equation:

$$\frac{\partial L'(y=0)}{\partial y} = \frac{1}{\cos^2\theta}\frac{u_n'}{\bar{U}_t}$$

The assumption that leads to this expression is the flame anchoring boundary condition, i.e. $\frac{\partial L'(y=0,t)}{\partial t} = 0$; this was justified in the previous section based on velocity field measurements.

In order to match the prediction in equation(1.5), $\frac{\partial L'(y=0)}{\partial y}$ is computed from flame-sheet measurements, and $\frac{1}{\cos^2\theta}\frac{u_n'}{\bar{U}_t}$ is estimated from PIV measurements, at identical conditions.

Starting first with the amplitude, inserting the measured velocity field data into equation(1.5), leads to a predicted near-field slope of $\frac{|u_n'(y,f_o)|}{\bar{U}_t(y)}\frac{1}{\cos^2\theta}$ = 0.15 ± 0.04/0.02. The variation of this quantity, i.e. the flame surface perturbation slope, in space is shown in Figure 4.3.1. Theory requires that this quantity be extracted at $y/\lambda_c = 0$, where data was not available. But based on the trend in the flame surface perturbation slope between $0.2 < y/\lambda_c < 0.4$, it was set as 0.15 as indicated by the dotted line in the figure.

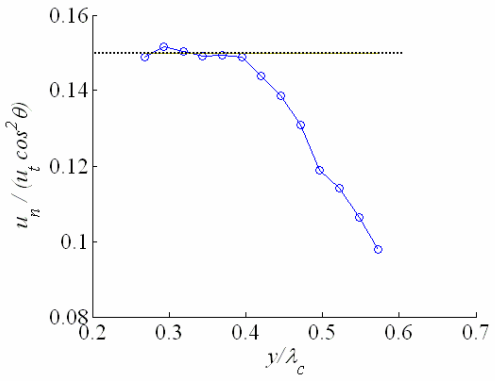

Figure 4.3.1: Axial dependence of the quantity $\frac{1}{\cos^2\theta}\frac{u_n'}{\bar{U}_t}$, extracted from PIV measurements (circles). Conditions: D = 9.52 mm, u'/U_∞ = 0.05 and ϕ = 0.67, triangular bluff body.

A further complication, particularly with velocity field specification further downstream, occurs because of flame sheet movement - measurements of the ensemble average perturbation velocity field just upstream of the flame front (i.e., at a temporally varying location), $\langle u(x(t),y(t))\rangle$, or at a spatially fixed point coinciding with some "average" flame front location, $\langle u(x_o,y_o)\rangle$, give different results.

Nonetheless, using $\langle u(x(t),y(t))\rangle$, very good quantitative comparisons are possible in the flame nearfield, see Figure 4.3.2. The flame surface perturbation slope as estimated

from the PIV measurements in excellent agreement with the value of $\frac{\partial |L'(y=0,f_o)|}{\partial y}$=0.16 ± 0.01 that was computed from the flame-sheet fluctuation measurements. The slope of the theoretical prediction in indicated in the figure. This shows a small departure from the measured value of 0.16.

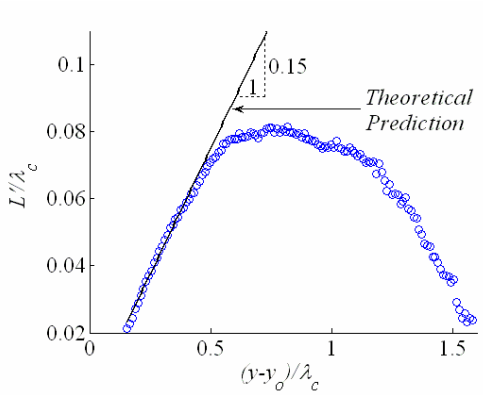

Figure 4.3.2: Comparison of axial dependence of flame sheet amplitude between experiments and theory. Conditions: U_∞ = 4.5 m/s, f_o = 300 Hz, D = 9.52 mm, u'/U_∞ = 0.05 and ϕ = 0.67, triangular bluff body.

In summary, the experimental data is in good agreement with the theoretical predictions.

4.4.Response of the Flame to Large Amplitude Forcing

The analysis to this point has focused on the flame response at the excitation frequency. In this section, we consider the flame's sub-harmonic response which was observed at f_o = *210 Hz*, where it was experimentally possible to attain acoustic velocities of the order of the mean flow. For other frequencies, such high forcing levels could not be reached due to limited speaker response at those frequencies. Under such conditions, sample flame responses computed at y = 0.66D are shown in Figure 4.4.1. For "low

amplitudes" of excitation, such as $u'/U_\infty = 0.42$, the spectrum in Figure 4.4.1a shows a discrete peak at the frequency of excitation. However, as the amplitude is increased to $u'/U_\infty = 0.7$, see (Figure 4.4.1b) that in addition to the response at the frequency of excitation, the flame front starts to flap at the first sub-harmonic too.

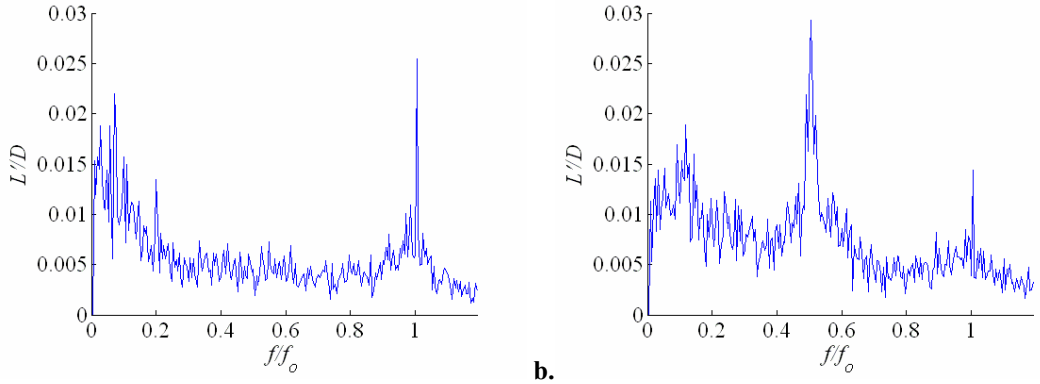

Figure 4.4.1: Spectrum of flame front fluctuations at $y = 0.66D$. a. $u'/U_\infty = 0.42$ b. $u'/U_\infty = 0.7$. Conditions: $U_\infty = 1.8$ m/s, $D = 9.52$ mm, $f_o = 210$ Hz, $\phi = 0.8$.

Figure 4.4.2a illustrates the amplitude dependence of the occurence of the sub-harmonic. See that up to a certain u'/U_∞, there is similar behavior as discussed previously (§4.1.2.1) – a linear region response region followed by saturation at high amplitudes. As the disturbance velocity is further increased, the response at the excitation frequency decreases slightly, while the sub-harmonic sharply increases. As the amplitude is further increased, the amplitude of the sub-harmonic decreases, and the amplitude of the fundamental increases again. The mechanism for the sub-harmonic response is possibly that of the parametric flame instability discussed by Baillot *et al.* (1999). Essentially, identical amplitude dependencies are observed for the sub-harmonic as seen here. This instability in the flame is related to the Rayleigh-Taylor instability which occurs when a heavy fluid is placed over a lighter fluid. This parametric instability is due to the

oscillatory acceleration of the flame interface which divides two fluids of different densities.

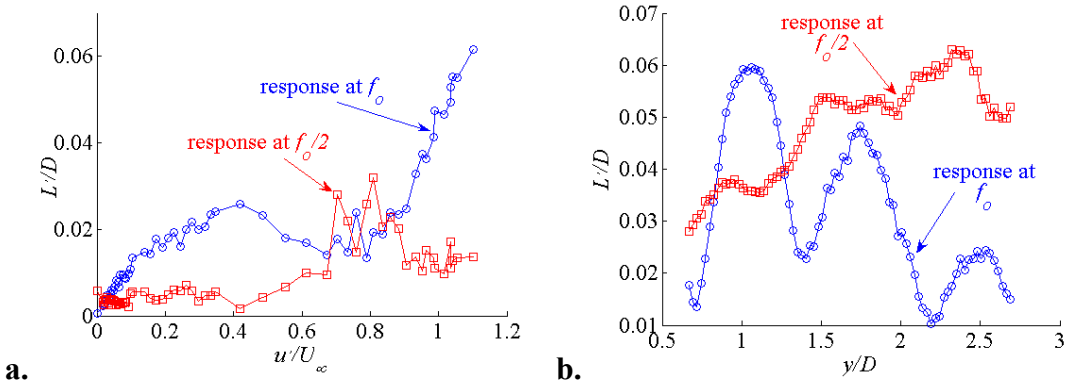

Figure 4.4.2: a. Amplitude dependence of flame response (measured at $y = 0.66D$, the first recorded point) at the forcing frequency, f_o & at the first sub-harmonic, $f_o/2$. b. Spatial evolution of the fundamental and the sub-harmonic for $u'/U_\infty = 0.7$. Conditions: $U_\infty = 1.8$ m/s, $D = 9.52$ mm, $f_o = 210$ Hz, $\phi = 0.8$.

Next, we shall address the spatial behavior of the flame response under the present conditions, i.e. when it responds at the fundamental and the sub-harmonic. Starting with Figure 4.4.1b, notice that at $u'/U_\infty = 0.7$, the amplitude at the sub-harmonic dominates over the fundamental. Figure 4.4.2b illustrates the spatial dependence of the fundamental and sub-harmonic response. It shows that the amplitude of the fundamental response grows, then decays, but in a modulated fashion, as discussed in the previous sections. The sub-harmonic grows gradually, apparently with little modulation. Of course, the extent of the observation was limited to only six bluff body diameters downstream (the graph is truncated at $y/D = 3$ because of poor signal to noise ratio downstream).

Some similarity can be seen with the behavior of the sub-harmonic in the wake compared to the generic response depicted in Figure 4.1.6a. In addition, this behavior is

similar to that observed in non-reacting shear layers (Brown and Roshko 1974), due to vortex pairing –this indicates that the sub-harmonic response is possibly also due to vortex pairing. Based on the dependence of the most amplified mode of the shear layer by Prasad and Williamson (1997), the natural frequency of the shear-layer fluctuations for the present conditions is estimated as:

U_∞ (m/s)	D (m)	Re	f_{BVK} (Hz)	$f_{SL} = 0.0235 \cdot f_{BVK}\,\mathrm{Re}^{0.67}$ (Hz)
1.8	9.52	1078.3	39.68	100.37

Immediately, it is seen that the natural frequency of the shear layer, 100 Hz is very close to the subharmonic frequency of excitation, viz. 105 Hz. Thus it is quite likely that the receptivity of the shear layer at the frequency of excitation saturates, and energy starts spilling over to the sub-harmonics, similar to what happens in planar free shear layers (Ho and Huerre 1984).

To get the more global picture, of the amplitude and spatial dependencies, see Figure 4.4.3. Cross-sections of this plot used earlier to illustrate the amplitude dependence (Figure 4.4.2a) and spatial dependence (Figure 4.4.2b) have also been marked, as black and grey points respectively. This plot tell us that the modulation of the flame response as it evolves in space occurs at all amplitudes, especially at the lower amplitudes where the sub-harmonic is not present. Hence, the modulation does not arise due to constructive/destructive interference between the fundamental and the sub-harmonic modes.

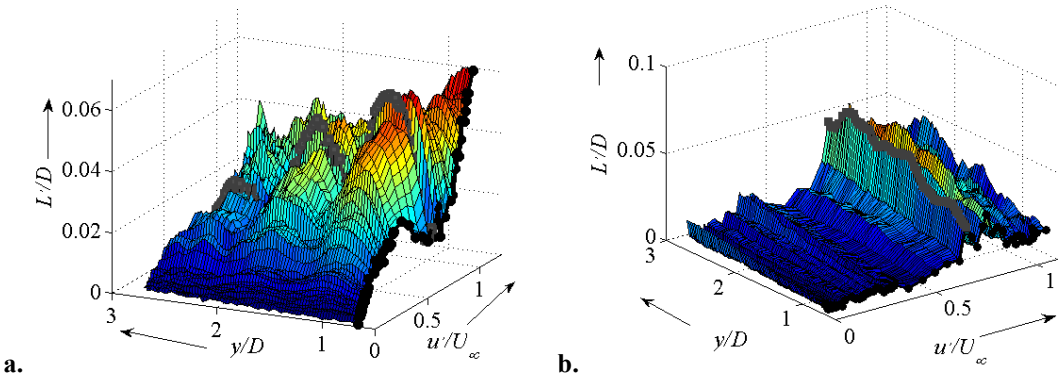

Figure 4.4.3: a. Spatial evolution of the flame response, at the frequency of excitation, as a function of amplitude of excitation. b. Spatial evolution of the flame response at the first sub-harmonic, as a function of amplitude of excitation. In both these figure, the black (-•-) and gray (-■-) symbols mark the cross-sections that displayed in Figure 4.4.2. Conditions: U_∞ = 1.8 m/s, D = 9.52 mm, f_o = 210 Hz, ϕ = 0.8.

All of the above points are summarized as an interaction diagram, see Figure 4.4.4.

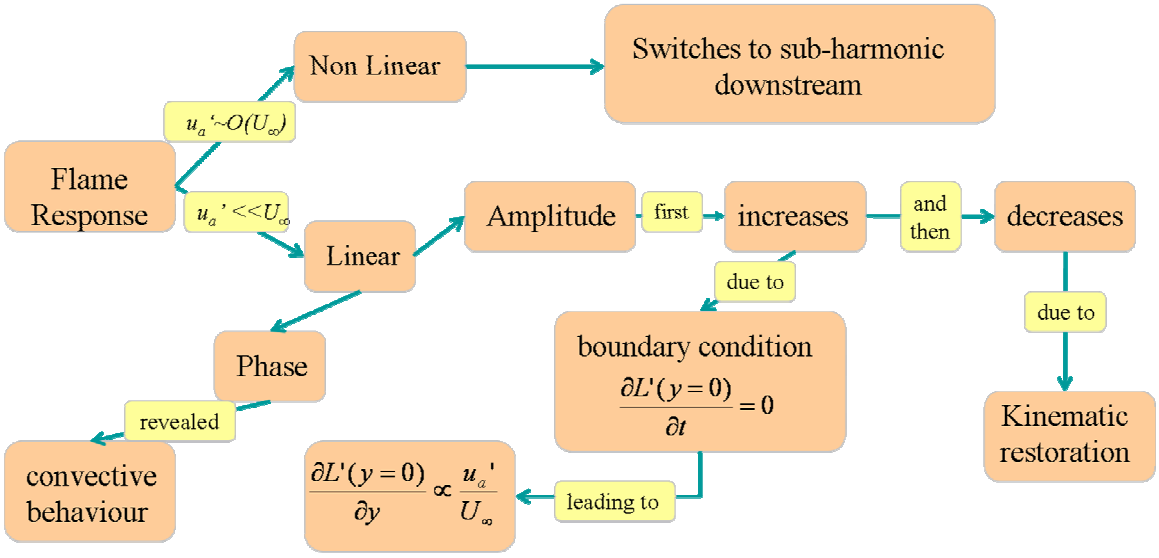

Figure 4.4.4: Interaction diagram summarizing the findings in this chapter.

CHAPTER 5

THE KELVIN-HELMHOLTZ INSTABILITY OF REACTING, ACOUSTICALLY EXCITED BLUFF-BODY FLOWFIELDS

This chapter describes the response of the reacting flow-field to acoustic excitation. §5.1 discusses the nature of the vorticity field and its behavior from instantaneous and phase-averaged perspectives. §5.2 presents vortex-rollup phase jitter, viz. a cycle-to-cycle variation in the position of the rolled-up vortices. §5.3 provides insight into the downstream decay of the vorticity and the role of combustion in the spatial characteristics of the vorticity field. Finally, §5.4 investigates the receptivity of the reacting shear-layer, i.e. the parametric dependence of the initial vorticity amplitude to acoustic excitation.

5.1. Response of the flow-field to acoustic excitation

This section discusses the basic characteristics of the perturbed vorticity field for bluff bodies with a triangular and circular cross-section.

5.1.1. Triangular Bluff Body Tests

A comparison of the flow-field and flame dynamics during forced and unforced conditions is shown in Figure 5.1.1, which overlays instantaneous and ensemble averaged vorticity contours with instantaneous flame sheet locations. In the absence of acoustic forcing (Figure 5.1.1a), i.e. when $u'/U_\infty = 0$, the vorticity is concentrated in the shear layer and monotonically decays downstream, being strongest at the separation point. This is shown also on an instantaneous basis, in Figure 5.1.3a. The same overlays

instantaneous flame sheet locations from 128 realizations, illustrating the flame brush. Notice that the flame is stabilized in the shear layer.

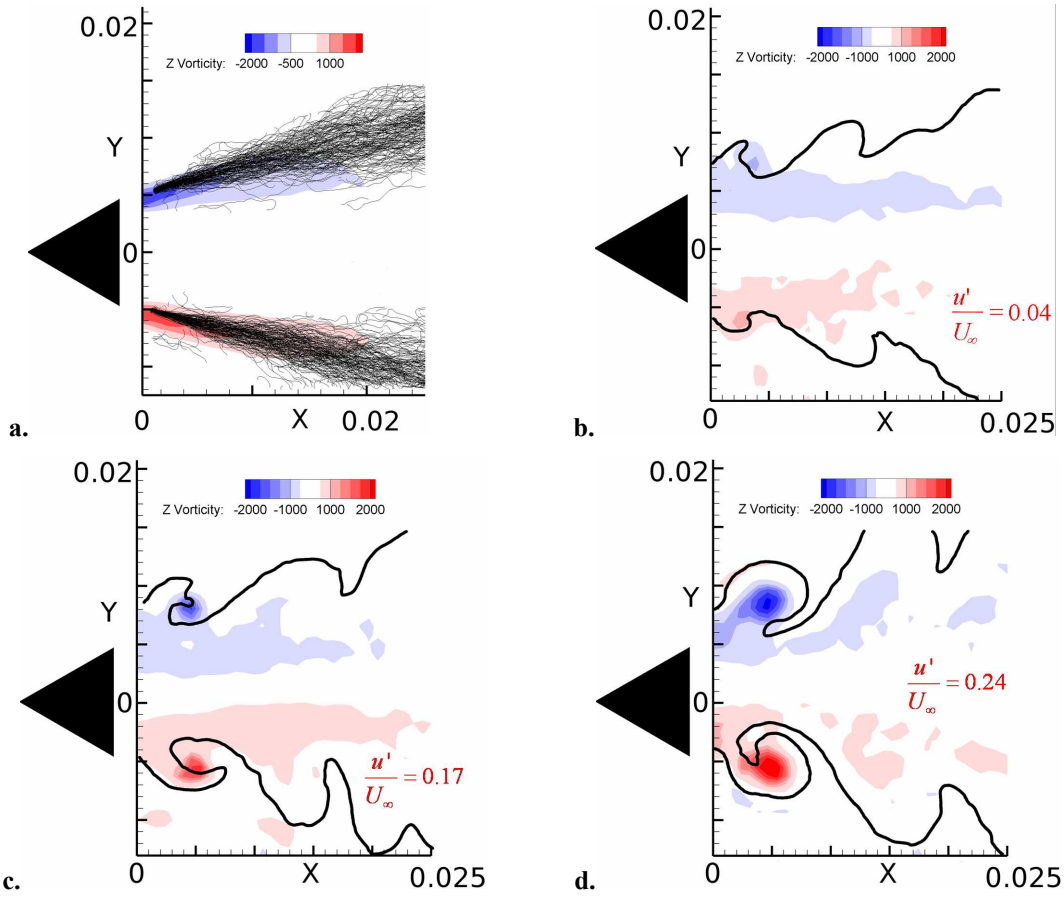

Figure 5.1.1: Instantaneous images of the flame sheet and vorticity field (a.) without excitation and (b.-d.) with increasing amplitudes of excitation at the same phase, i.e. = 135°. Conditions: d = 9.52 mm, U_∞=2.7 m/s, f_o =300 Hz & ϕ = 0.72

As acoustic forcing is introduced, (Figure 5.1.1b-d), the presence of concentrated regions of vorticity within the shear layer are evident, whose magnitudes are dependent on the amplitude of excitation. The flame is directly influenced by the vorticity field. Notice that as the amplitude of vorticity increases, the flame becomes even more contorted. If the amplitude of the vorticity is high enough (Figure 5.1.1d) the complete roll-up of the flame by the convecting vortical structure is also seen. These images also

show that the vorticity/velocity field that perturbs the flame decays quickly. The vortical structures originate in the shear layer of the bluff body and propagate in the direction of the flow.

In order to understand the evolution of the velocity field and its interaction with the flame, Figure 5.1.2 plots phase locked images vorticity field at three phases. The first image overlays 128 flame images obtained at this same phase, as well as the ensemble averaged vorticity field. The remaining three phases overlay the instantaneous vorticity and flame position. Examination of the plots illustrates the formation of regions of intense vorticity at the bluff body separation point that subsequently convect downstream. These are associated with the rollup of the harmonically pulsing vortex sheet originating at the separation point. The rotating flow strongly distorts the flame, causing it to be wrapped around the center of vorticity. The fluctuations in vorticity cause corresponding fluctuations in surface area, and therefore, heat release rate of the flame. The decay in vorticity field farther downstream is also clearly evident in the figure – note that the vortex formed in the immediate cycle of forcing is clearly present, the one formed in the prior cycle of forcing (the one associated with the second wrinkle on the flame) is nearly gone but unrecognizable, and the one forced two preceding cycles earlier is not recognizable. This means that the vortex decays within two convective wavelengths for this result; in other results shown later it persists up to four convective wavelengths downstream. Also, note the nearly symmetric response of the shear layer, as evidenced by the nearly identical vorticity and flame sheet on both the top and bottom sides of the bluff body shear layer.

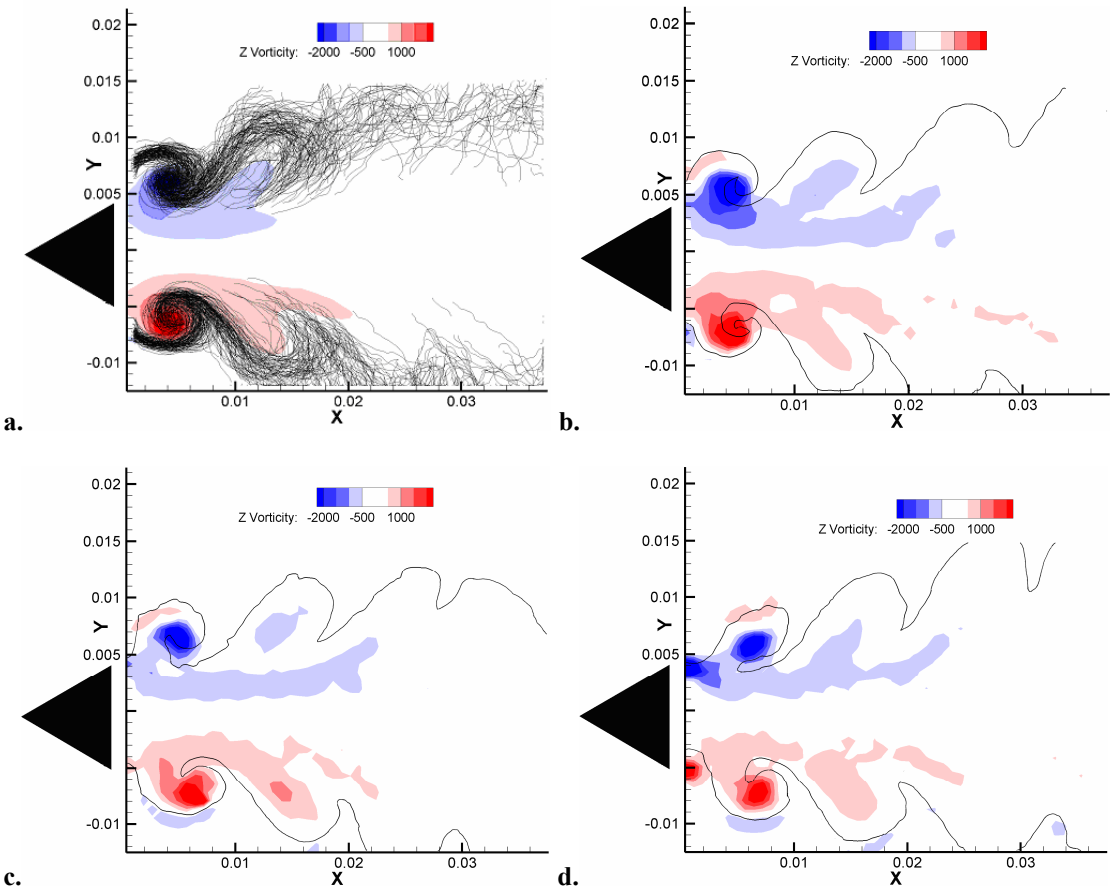

Figure 5.1.2: Illustration of the interaction between the vorticity field and the flame. a. Phase averaged vorticity field and overlay of instantaneous flame location for 128 images taken at 0^o phase acoustic excitation. Instantaneous vorticity field and flame edge at phases 0^o (b.), 45^o (c.), and 90^o (d.). Dimensions in the figure are in meters.

From the first image, an estimate of the repeatability of the phenomenon can be gained. The overlaid flame images are almost directly on top of each other in the near-field region indicating very strong phase locking of the vortical perturbations, and therefore the flame, to the excitation field. Farther downstream, more scatter can be seen in the flame position. As will be shown later, this is due to phase jitter.

These images indicate that the flame sheet dynamics are controlled by their interaction with the convecting vorticity field, as opposed to a direct response to the velocity oscillations directly associated with the acoustic field. This illustrates that

understanding this flame interaction problem requires an understanding of the growth, propagation, and decay of these vortices in a reacting, harmonically oscillating flow field.

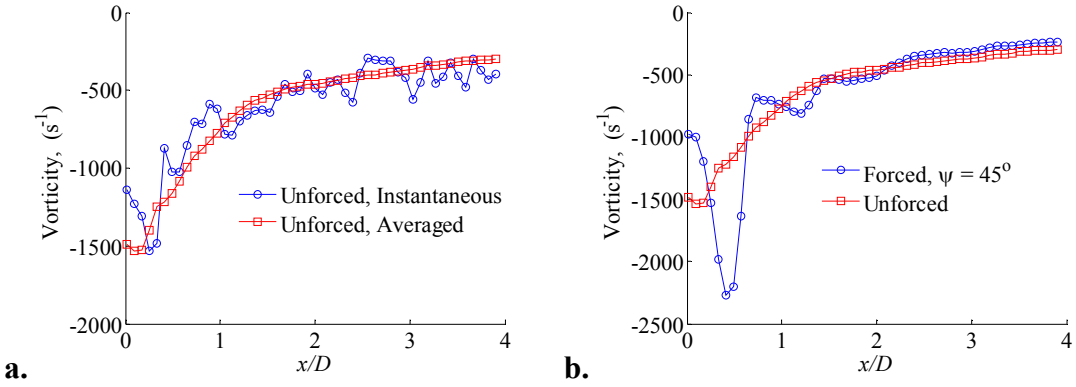

Figure 5.1.3: a. Dependence of instantaneous (circles) and ensemble averaged (squares) vorticity upon axial location, in the absence of acoustic excitation. b. Dependence of ensemble averaged vorticity profile upon axial location at 45° phase (circles). The amplitude of excitation is $u'/U_\infty = 0.29$. Time averaged vorticity also shown for reference (squares). For both cases $\phi = 0.71$.

We next consider the spatial evolution of the vorticity field at different phases of the cycle more quantitatively. This was accomplished by determining the maximum value of the vorticity at each axial location, *x*. This corresponds to the trajectory of the vortex sheet. As a baseline, Figure 5.1.3a plots an instantaneous and time averaged value of this maximum vorticity value for the unforced case. The unforced case shows the intense vorticity at the bluff body separation point, which monotonically decays downstream, as discussed elsewhere in the literature (Bush and Gutmark 2007, Nair and Lieuwen 2007). Figure 5.1.3b overlays this same time averaged value with the ensemble averaged value at one phase of the cycle. The forced case clearly shows the phase locked modulation of vorticity amplitude about this mean value. However, the convecting vortical structure is very rapidly dissipated; i.e., two clear structures are clearly evident, and a third and fourth structure of very small amplitude can also be seen, albeit faintly.

5.1.2. Circular Bluff Body Tests

The above results were obtained with the triangular bluff body (referred to as TBB, hereon) that employed a sharp separation point. In this section, we consider how these results are altered with a circular bluff body (referred to as CBB, hereon), where the separation point is not well-defined and can possibly exhibit oscillations with stochastic characteristics. An overlay of instantaneous flame images and vorticity field are plotted in Figure 5.1.4 at three phases of the cycle. On an instantaneous basis, the results are quite similar to those from the prior section, with the exception of substantially more asymmetry in the upper and lower flame branches. This suggests that the vortex sheet dynamics of the top and bottom shear layers are not as phase synchronized as in the TBB. This point can particularly be seen in Figure 5.1.4a, which shows an overlay of 128 flame images and the ensemble averaged vorticity field. The flame position is clearly spread out substantially and the vorticity is smeared out. This shows that there is a significantly wider variation in the position of the vortex (spatial jitter), its vorticity and hence the flame that is wrapped around it.

Interestingly, however, the vorticity decay rate is substantially lower than for the TBB at the same temperature ratio, i.e., three distinct vortices can clearly be seen downstream. Part of this is due to the relative location of the flame and vortex sheet. Note that in many of the images that the vortex centers are in the cold, reactant regime, where the diffusivity is substantially lower.

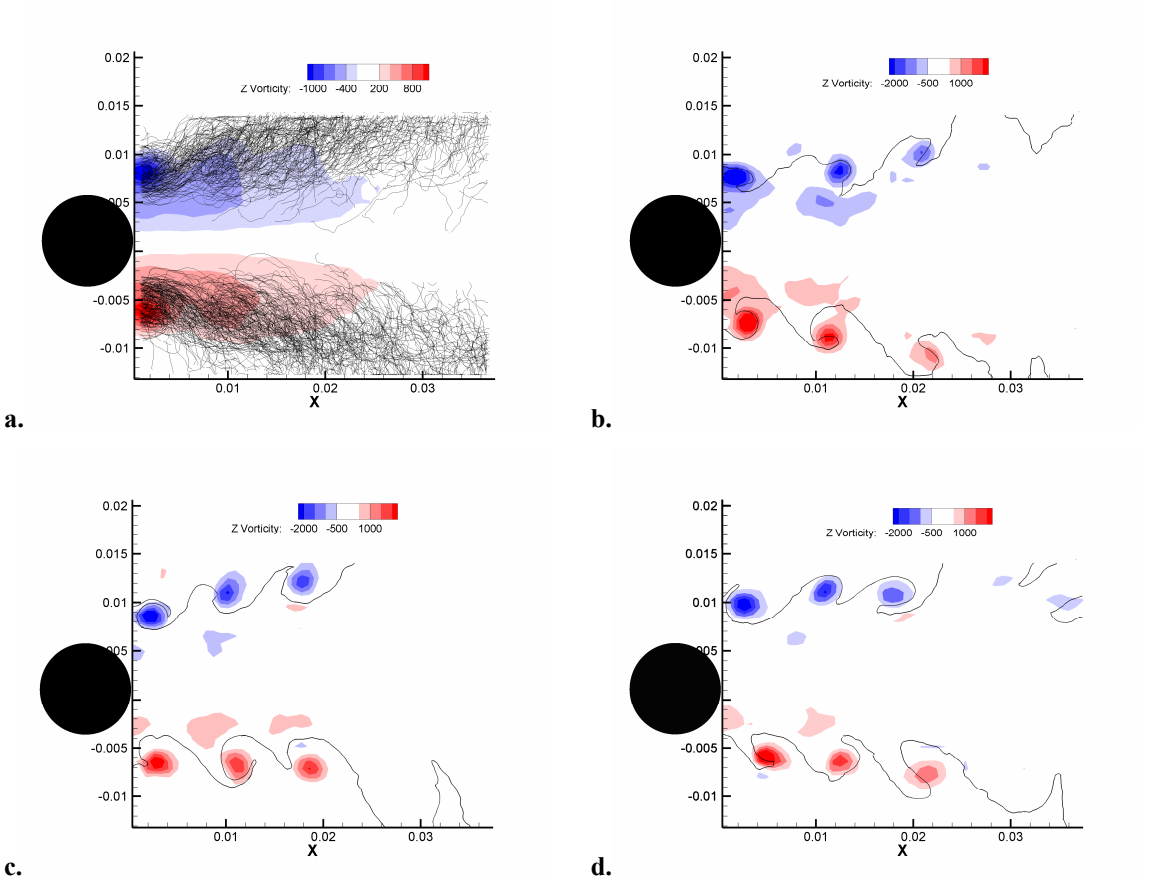

Figure 5.1.4: a. Illustration of the interaction between the vorticity field and the flame. a. Phase averaged vorticity field and overlay of instantaneous flame location for 128 images taken at 0^o phase acoustic excitation, with amplitude $u'/U_\infty = 0.29$. (Remaining images) Instantaneous vorticity field and flame edge at 0^o (b.), 45^o (c.), and 90^o (d.). Dimensions in the figure are in meters. The flow direction is from left to right. Conditions: $D = 9.52$ mm, $U_\infty = 2.7$ m/s, $\phi = 0.71$

To quantify the effect of phase jitter and how it compares for the TBB and CBB, Figure 5.1.5 (left) plots the locations of the vortex core center at one phase of the cycle, at the same amplitude of acoustic excitation. The figure indicates that the variation in CBB vortex core center is approximately twice that of the TBB. In other words, for the CBB, the vortices occupy positions that are further spread from the mean, compared to the TBB.

Because of phase jitter, ensemble averaging smears out the vorticity field, as discussed above. As such, some care must be taken in interpreting vorticity decay rates

and amplitudes for the acoustically forced case. That is, taking the maximum vorticity amplitude from the ensemble averaged field, as done in the TBB case in the prior section, leads to a different answer than if one takes the average of the maximum vorticity values. In the rest of this section, we consider both approaches for interpreting the data.

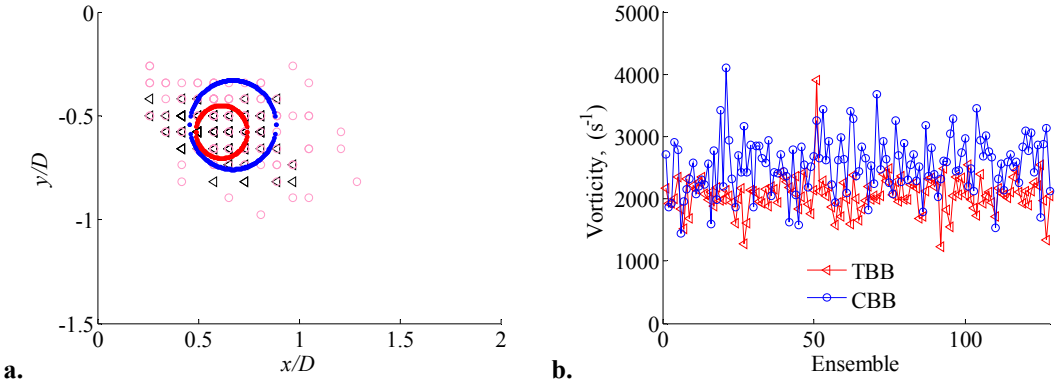

Figure 5.1.5. a. Location of instantaneous peak location of the vortex center for TBB flow-fields (black, triangles) and CBB flow-fields (pink, circles), both for 135° phase of excitation and amplitude of excitation $u'/U_\infty = 0.29$. Circles are also drawn that mark the boundary containing 50% of all the peaks for TBB (red circle) and CBB (blue circle) flow-fields. b. Instantaneous variation of the peak vorticity across 128 ensembles for TBB (triangles) and CBB (circles) flow-fields. Conditions: U_∞ = m/s, D = 9.52 mm, ϕ = 0.71

A comparison of the ensemble averaged and instantaneous vorticity fields between the TBB and CBB illustrate this point; see Figure 5.1.6 (left). The ensemble averaged result shows similar spatial behavior between the two bluff bodies, but a clear reduction in vorticity amplitude in the CBB. This is due to averaging across vortices with time varying locations, as can be seen by comparing these ensemble averaged results with representative instantaneous ones. It can be seen that the instantaneous vorticity values are actually larger for the CBB than the TBB, opposite the result suggested by the ensemble averaged curves.

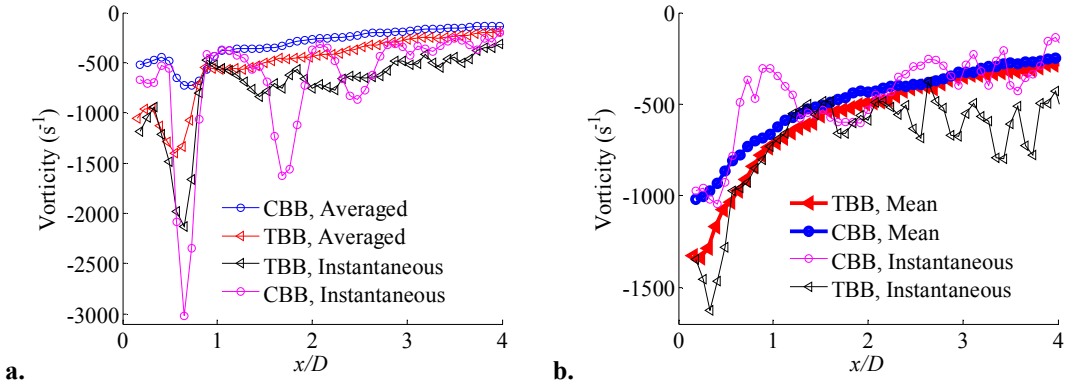

Figure 5.1.6. a. Dependence of ensemble averaged vorticity fluctuations for two different bluff bodies, triangular (red triangles) and circular (CBB, blue circles) during acoustic excitation. In both cases, the amplitude of acoustic excitation is $u'/U_\infty = 0.29$. b. Dependence of vorticity distribution on axial location for CBB (circles) and TBB (triangles) flow-fields for unforced cases. Conditions: $D = 9.52$ mm, $\phi = 0.71$.

To illustrate this further, Figure 5.1.5 (right), plots the magnitude of the maximum vorticity value for each of the 128 images obtained at one excitation phase. The curves are slightly offset due to the higher mean value of vorticity for the CBB case in the forced case. From this result, one can see substantially larger instantaneous values and fluctuations in vortex strength in the CBB case relative to the TBB. Furthermore, the offset in mean value of vorticity of the CBB relative to the TBB is opposite to that in the unforced case, see Figure 5.1.6 (right); i.e., in the unforced case, the TBB mean vorticity distribution is everywhere higher than that of the CBB. Naturally, the vorticity distribution at the separation point will be dependent on the radius of curvature of the bluff-body at the point of separation, causing larger mean vorticity levels for the TBB.

A more conclusive explanation of the higher instantaneous vorticity for the CBB relative to the TBB requires us to understand why, despite the relatively comparable values in initial vorticity amplitude, the decay rates downstream are very different. As such, understanding the question would require knowledge of the processes controlling

the decay of the vorticity. A necessary step then, is quantifying the decay of vorticity downstream, accounting for the effects of spatial jitter. This issue is addressed next.

5.2. Phase Jitter

The previous section revealed the cycle-to-cycle variation in the position of the vortices which we shall henceforth refer to as phase jitter. That is, the trajectory of the vortex center is not perfectly repeatable, even under harmonic excitation. This effect is well-known in the non-forced case and leads to a broadened peak in the shear layer velocity perturbation spectra, if measurements are carried out without conditional sampling (Cardell 1993). This effect is much larger in circular bluff body stabilized flames than triangular flames, due to the fluctuations of the flow separation point in the former case, as will be quantified in this section.

However, this phase jitter is appreciable even in triangular bluff bodies with sharp separation points. In other words, even when the initial vorticity formation processes are phase locked to the excitation, their downstream evolution processes exhibit stochastic characteristics. In order to appreciate the magnitude of this effect, see Figure 5.2.1. Figure 5.2.1a shows the instantaneous vorticity contours, with the flame sheet location superimposed. Under identical conditions, an average of 128 images is also shown in the Figure 5.2.1c. These two figures show that the locations and magnitudes of the vortices close to the bluff-body have closer values compared to the vortices downstream. As an example, compare the contour levels of the second and third vortex, between images (a) & (c). In the averaged image, there is an order of magnitude difference between the peak vorticity levels of the third vortex compared with the third vortex in the instantaneous image.

To facilitate easy quantification of this effect, Figure 5.2.1b plots the axial variation of vorticity from three different realizations, but at the same phase with respect to the excitation. These vorticity magnitudes were obtained by extracting the maximum vorticity along the shear layer. First, notice the presence of three well-defined (negative) peaks in all the realizations, coinciding with the vortex center. This location is not constant from image to image. Next, notice the decaying magnitude of these peaks in downstream direction, due to decay in vorticity amplitude. Finally, notice that this variation in position increases in the downstream direction - arrows are drawn to similar peaks and a horizontal line is drawn below each arrow-set to indicate the extent of deviation. Clearly, the jitter is enhanced as the vortex develops in space. The green dashed line indicates the same quantity calculated from the ensemble averaged image. Note the substantial variation in vorticity magnitude between the instantaneous and ensemble averaged results at the second and third vortex center. Clearly, vorticity decay rates estimated from instantaneous and ensemble averaged images can differ considerably, solely because of phase jitter. Hence, any procedure that attempts to quantify the decay of vorticity would require accounting for phase jitter, and will be done in detail in the next section where decay rates are quantified. The remainder of this section will focus on studying the characteristics of phase jitter.

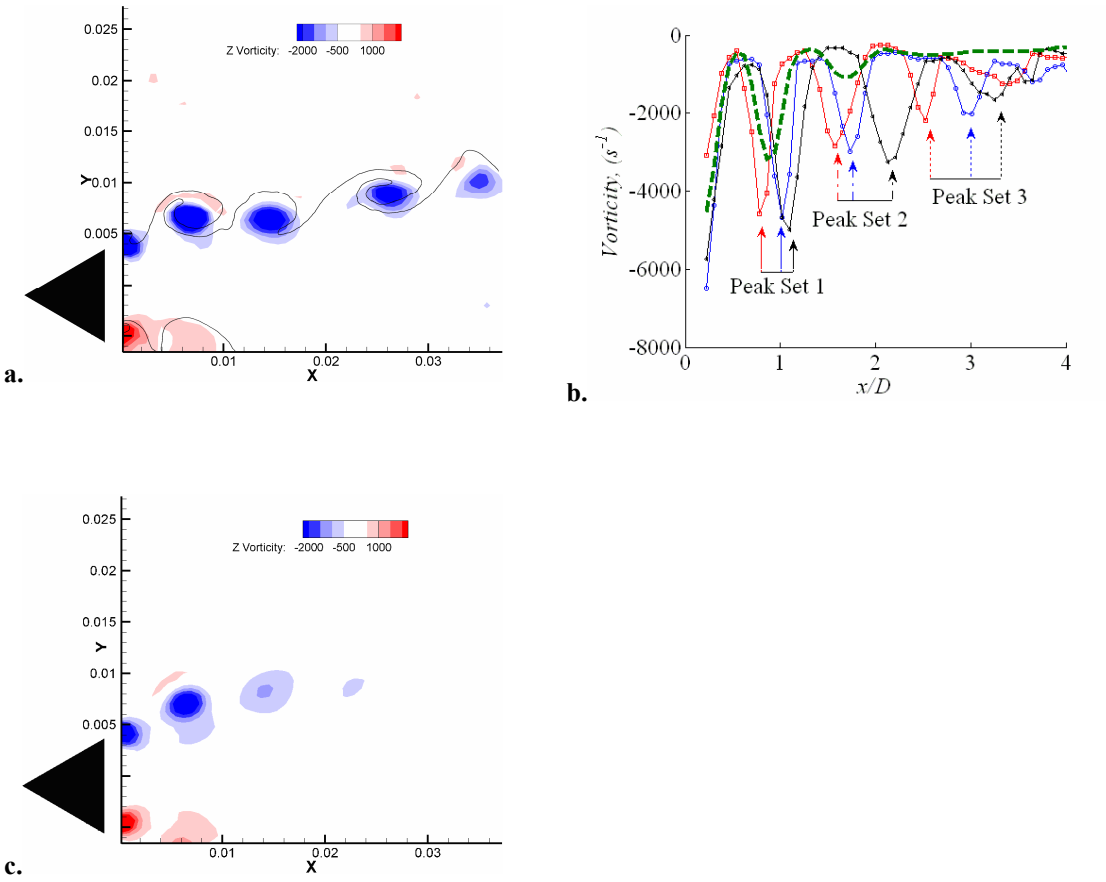

Figure 5.2.1. (a) Instantaneous vorticity contours and flame sheet location. (c) Ensemble averaged vorticity contours. (b) Illustration of axial vorticity variation. The dashed line (---) represents the ensemble averaged vorticity variation at $\psi = 135^{o}$. The other three lines represent realizations at different instances of time for $\psi = 135^{o}$. Other conditions: $D = 9.52$ mm, $\phi = 0.63$, $U_{\infty} = 2.7$ m/s, $u'/U_{\infty} = 0.29$ & $f = 300$ Hz.

To understand the behavior of phase jitter (x_{σ}), consider Figure 5.2.2a. This graph plots phase jitter as a function of downstream distance for two different velocity conditions, i.e. U_{∞} = 2.3 m/s (squares: ■, ■, ■, ■) and U_{∞} = 4.1 m/s (circles: ●, ●, ●). The different colors for a given shape indicate that even at a fixed velocity, parametric variations exist in frequency and amplitude of excitation, as detailed in Table 5.1. The figure tells us that phase jitter for the low velocity case is large, compared to the high velocity case. As such, there exist variations of phase jitter with amplitude of excitation, but these are minor compared to the large jump seen due to the change in free-stream

velocity. Despite the variation in approach flow velocity, frequency and amplitude of excitation, phase jitter monotonically increases as the vortex convects downstream.

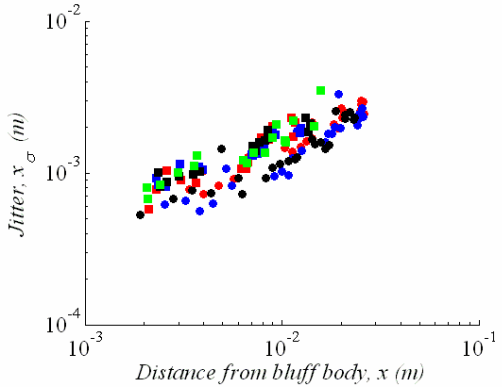

Figure 5.2.2. Phase jitter plotted (on a log-log plot) as a function of distance from the bluff body for two different velocity conditions. Squares represent U_∞ = 2.3 m/s and circles U_∞ = 4.1 m/s. The conditions corresponding to each symbol are listed in Table 5.1.

These phase jitter characteristics resemble a Random-Walk process (Taylor 1922) shown schematically in Figure 5.2.3. The bottom half of the figure shows three discrete vortices, typical of an instantaneous representation at a given phase (see Figure 5.1.2c & Figure 5.2.1a). In the absence of phase jitter, this would be the exact same picture, if the same phase from a later cycle is recorded. The centers of each of these vortices are shown by green dot on the top-half of the figure. Now, in the presence of phase jitter, on an instantaneous basis (at the same phase), the recorded position varies from cycle to cycle. If all the vortex centers (at the same phase) are superimposed on top of each other, one would obtain a picture shown as clouds of blue points. That is, centered about a mean position, there is a random deviation of the vortex. The question of interest is how this deviation varies from one vortex location to another (i.e. from one green dot to another). On this issue, the random walk description tell us that as the vortex migrates from one position to another, the standard deviation in the position of the vortex increases, as the

time of migration increases and depends whether subsequent motions are correlated of uncorrelated.

For perfectly correlated motions:

$$x_\sigma = \tilde{c}T \tag{6}$$

and, for uncorrelated motions:

$$x_\sigma = \tilde{c}\sqrt{2AT} \tag{7}$$

where A is a correlation coefficient that describes how subsequent motions are correlated.

Since the vortex is convected with the free-stream velocity, the time of migration can be related to the mean position of the vortex as:

$$T = \frac{x}{U_\infty} \tag{8}$$

Then, for uncorrelated motions,

$$x_\sigma \propto \sqrt{\frac{x}{U_\infty}} \tag{9}$$

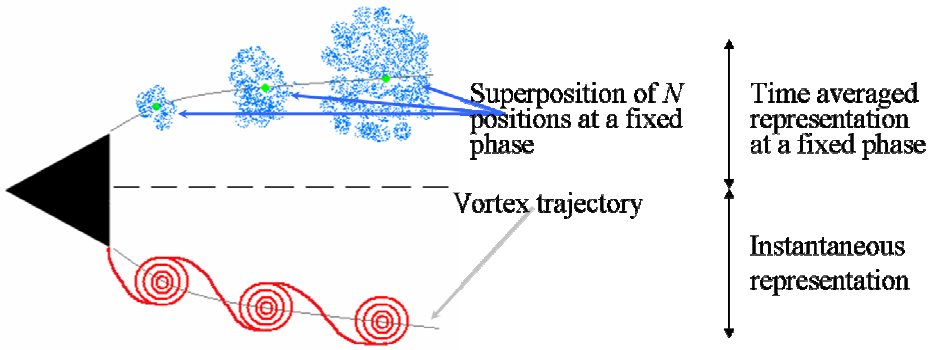

Figure 5.2.3: Illustration of phase jitter as a Random-Walk process

Based on the above considerations, the phase jitter data from Figure 5.2.2 is re-plotted as a function of migration time in Figure 5.2.4a. It can be seen that the data collapses reasonably well. To further strengthen the point, the same data is plotted along

with data from other parametric variations in Figure 5.2.4b. The conditions are detailed in Table 5.1. For all these cases, the data show a roughly power-law increase in magnitude with downstream distance, with significant overlap of data points on one another. Moreover, the parametric range included variations in mean velocity, diameter, frequency and amplitude of excitation. This tells us that to the first order, phase jitter scales with the migration time. As such, there is a mild dependence of phase jitter on the amplitude of excitation, which will be discussed in the following section.

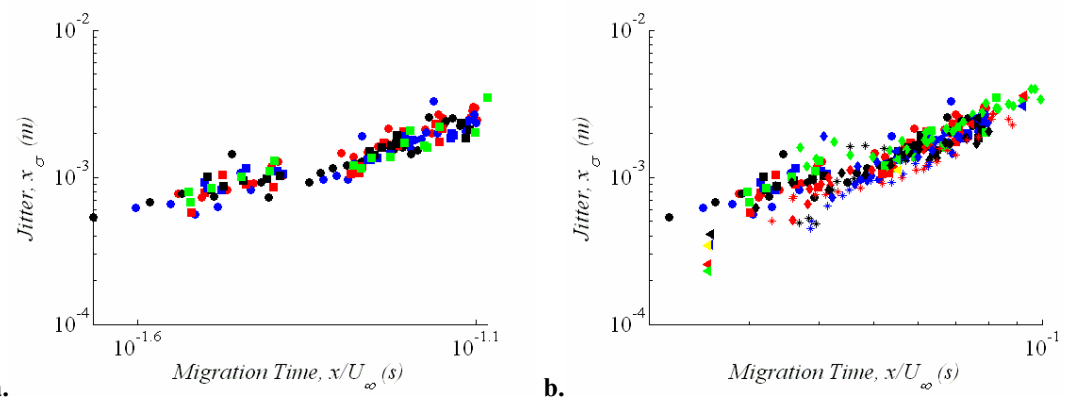

Figure 5.2.4: a. Phase jitter as a function of migration time. The data is identical to that in Figure 5.2.2. b. Compilation of phase jitter data, for a range of conditions. The conditions corresponding to each symbol are listed in Table 5.1. Both plots are on a log-log scale.

Table 5.1: Experimental conditions for each symbol plotted in Figure 5.2.4. For a given symbol shape, the grey background indicates the parameters that were varied within the data sets, all other conditions being the same.

Symbol	U_∞ (m/s)	D (mm)	ϕ	T_b/T_u	u'/U_∞	f (Hz)	Phase, ψ (degrees)
●	4.1	9.52	0.65	5.87	0.11	300	45,90,135,180,225,240
●	4.1	9.52	0.65	5.87	0.15	450	45,90,135,180,225,240
●	4.1	9.52	0.65	5.87	0.16	600	45,90,135,180,225,240
■	2.3	9.52	0.72	6.24	0.56	420	45,90,135,180,225,240
■	2.3	9.52	0.72	6.24	0.45	420	45,90,135,180,225,240
■	2.3	9.52	0.72	6.24	0.35	420	45,90,135,180,225,240
■	2.3	9.52	0.72	6.24	0.26	420	45,90,135,180,225,240
*	2.7	9.52	0.69	6.07	0.24	300	0,45,90,135,180,225,240,300,330
*	2.7	9.52	0.75	6.40	0.24	300	0,45,90,135,180,225,240,300,330
*	2.7	9.52	0.82	6.75	0.24	300	0,45,90,135,180,225,240,300,330
♦	2.7	6.35	0.7	6.12	0.29	300	0,45,90,135,180,225,240,300,330
♦	2.7	9.52	0.7	6.12	0.29	300	0,45,90,135,180,225,240,300,330
♦	2.7	12.7	0.7	6.12	0.29	300	0,45,90,135,180,225,240,300,330
♦	2.7	19.05	0.7	6.12	0.29	300	0,45,90,135,180,225,240,300,330
◀	2.9	9.52	0.63	5.76	0.29	300	135
◀	2.9	9.52	0.65	5.87	0.29	300	135
◀	2.9	9.52	0.68	6.05	0.29	300	135
◀	2.9	9.52	0.71	6.18	0.29	300	135
◀	2.9	9.52	0.74	6.38	0.29	300	135

5.2.1. Influence of separation point fluctuations

The previous section discussed phase jitter exclusively for triangular bluff bodies (TBB) where the separation point is sharp. This section will explore how the shape of the separation point changes phase jitter. The motivation for this is two fold. First, as was discussed in Chapter 2 we saw that for circular bluff bodies (CBB), the separation point fluctuates and leads to the rollup occurring at a different spatial location. The contribution of this particular "boundary condition" on phase jitter needs remains to be seen.

Second, a quantification of phase jitter for TBB and CBB also needs to be carried out to address the differences between the vorticity fields and flame brushes as is seen in Figure 5.1.2a and Figure 5.1.4a. For all the data reported in this thesis using TBB, the vorticity fields and flame brushes were similar to Figure 5.1.2a. This leads us to anticipate, that phase jitter should be higher for CBB compared to TBB.

To answer the above questions, experiments were performed on TBB and CBB at identical conditions. The results are shown in Figure 5.2.5. Notice that phase jitter is much higher for a CBB compared to the TBB. Second, extrapolation of both trends towards $x = 0$ tells us that there is a higher offset for the CBB at the origin, compared to the TBB. Presumably, this offset is a measure of the separation point fluctuations. For reference, all the data from Figure 5.2.4 is also plotted on the same figure. This tells us that phase jitter for the CBB is higher than that for all the experiments carried out on TBB reported earlier. This is why the degree of smearing of the vorticity fields and flame brushes seen in Figure 5.1.4a for CBB, could not be captured for any conditions at which experiments were performed for TBB.

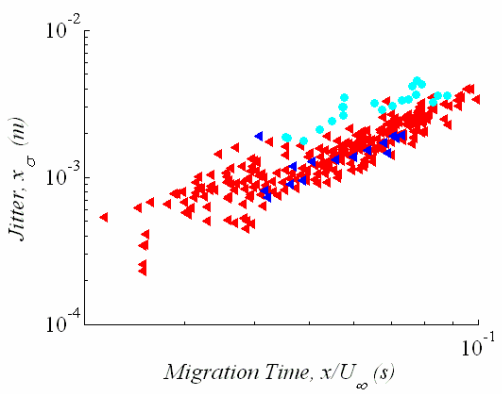

Figure 5.2.5: Comparison between phase jitter for TBB and CBB. All previous data for TBB, i.e. from Figure 5.2.4b, have been reproduced here for reference and are represented by red triangles (◀). The conditions for the symbols (●) and (◀) are detailed in Table 5.2. Axes are on a log-log scale.

Table 5.2: Experimental conditions for the new data plotted in Figure 5.2.5. The conditions for the two cases listed below are identical. The only difference is the shape of the bluff body.

Symbol	Cross Section	U_∞ (m/s)	D (mm)	ϕ	T_b/T_u	u'/U_∞	f (Hz)	Phase, ψ (degrees)
◀	Triangle	2.7	9.52	0.7	6.12	0.29	300	9 phases
●	Circle	2.7	9.52	0.7	6.12	0.29	300	9 phases

Finally, experiments were also performed to determine the amplitude dependence of phase jitter. The results are plotted in Figure 5.2.6. For the TBB, increasing the amplitude of excitation seems to mildly decrease phase jitter. For the CBB, the same effect is seen, although the levels of phase jitter are higher, as is expected.

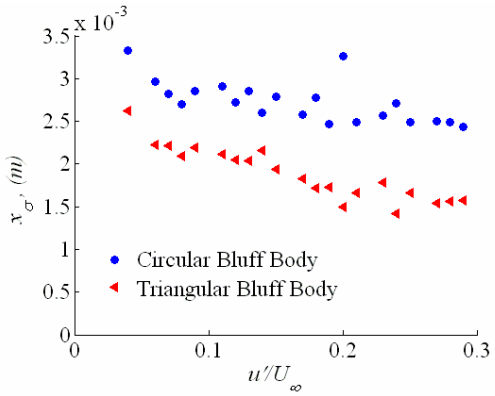

Figure 5.2.6. Phase jitter plotted as a function of perturbation amplitude for both, triangular and circular bluff bodies.

5.3.Downstream decay of vorticity

This section focuses on the spatial characteristics of the vorticity field. Already, in Figure 5.1.2 it was shown that the vorticity field decays quickly within two diameters downstream. In order to understand the processes that govern the decay, we first need to account for phase jitter effects in estimating the decay rate, as would happen if the decay rates are estimated from ensemble averaged vorticity fields.

In order to compute the vorticity decay rates, the 128 phase locked measurements, obtained at nine phases, were analyzed. Two different procedures were employed (1) extracting maximum vorticity amplitudes from ensemble averaged images, i.e. $\omega'(x) = max(<\omega'(x)>)$ and (2) averaging the maximum of the vorticity at each phase from the instantaneous images, yielding $\omega'(x) = <max\ \omega'(x)>$. For the first procedure, the velocity fields from all 128 realizations were averaged. The local maxima in vorticity were then identified. For the second procedure, the magnitude and position of each local maxima in vorticity were identified from the 128 images individually. Then, the amplitudes and

positions of each peak are averaged separately using the procedure described in Chapter 3, §3.4.2.

Typical results illustrating the output from both methods are shown in Figure 5.3.1. The horizontal bars in the peak averaged data indicate the standard deviation, in vortex location. The two curves have comparable amplitudes in the bluff body near-field, where phase jitter effects are minimal. Moving downstream, the ensemble averaged representation overestimates the decay rate, as also noted above. Second, the ensemble averaged representation indicates a monotonic reduction in amplitude, while the peak averaged representation indicates an initial region of amplitude growth. In the rest of the paper all spatial vorticity variations reported were computed using the peak averaged method unless explicitly mentioned otherwise.

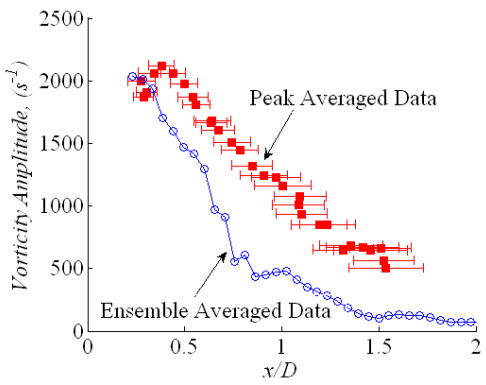

Figure 5.3.1: Vorticity decay rate estimated by ensemble averaging and peak averaging. Horizontal bars denote standard deviations of the vorticity positions. Conditions: D = 19.05 mm, ϕ = 0.70. For all data: U_∞ = 2.7 m/s, u'/U_∞ = 0.29 & f = 300 Hz.

These results illustrate that the vorticity field disturbing the flame starts at some initial value, then decays downstream – i.e.,

$$\omega'(s,t) = \mathrm{Re}\{\omega'(s=0)g(s)e^{-j2\pi f(t-\frac{s}{U_c})}\} \quad (1)$$

where s is the coordinate along the shear layer (with the origin at the separation point), f is the frequency of excitation and U_c the convection velocity of the vortex. The equation shows that two processes need to be understood in order to capture the key flow field features: the initial vorticity amplitude, $\omega'(s=0)$ and its downstream decay profile, $g(s)$. The rest of this section will focus on the downstream decay of vorticity. The initial vorticity amplitude will be dealt with in the next section.

In Figure 5.1.6a (§5.1.2), the decay of vorticity was quantified for TBB and CBB at identical conditions, using the ensemble averaged method. This, along with the simultaneous visualization of the vorticity field and the flame for both cases (Figure 5.1.2 and Figure 5.1.4) tells us that an important parameter controlling the decay of vorticity is the vortex sheet trajectory relative to the flame. In cases where the vortices are on the burned side, much more rapid decay of vorticity is noted relative to when they are on the unburned side. This effect can be attributed to the substantially larger viscosity in the hot products relative to the reactants (viscosity increases by a factor of 3.13 due to the temperature jump). However, even for cases where the vortex is only on one side of the flame, the decay rate can vary widely with seemingly small variations in conditions, such as equivalence ratio, as shown in Figure 5.3.2. These plots show the instantaneous vorticity field and flame front at for five different equivalence ratios, all other conditions being the same. For the lowest equivalence ratio, i.e. $\phi = 0.63$, up to five vortices can be seen downstream. In contrast, for the highest equivalence ratio, i.e. $\phi = 0.74$, only two vortices are seen. Clearly, this tells us that the point at which the vorticity completely decays is a function of the temperature jump across the flame.

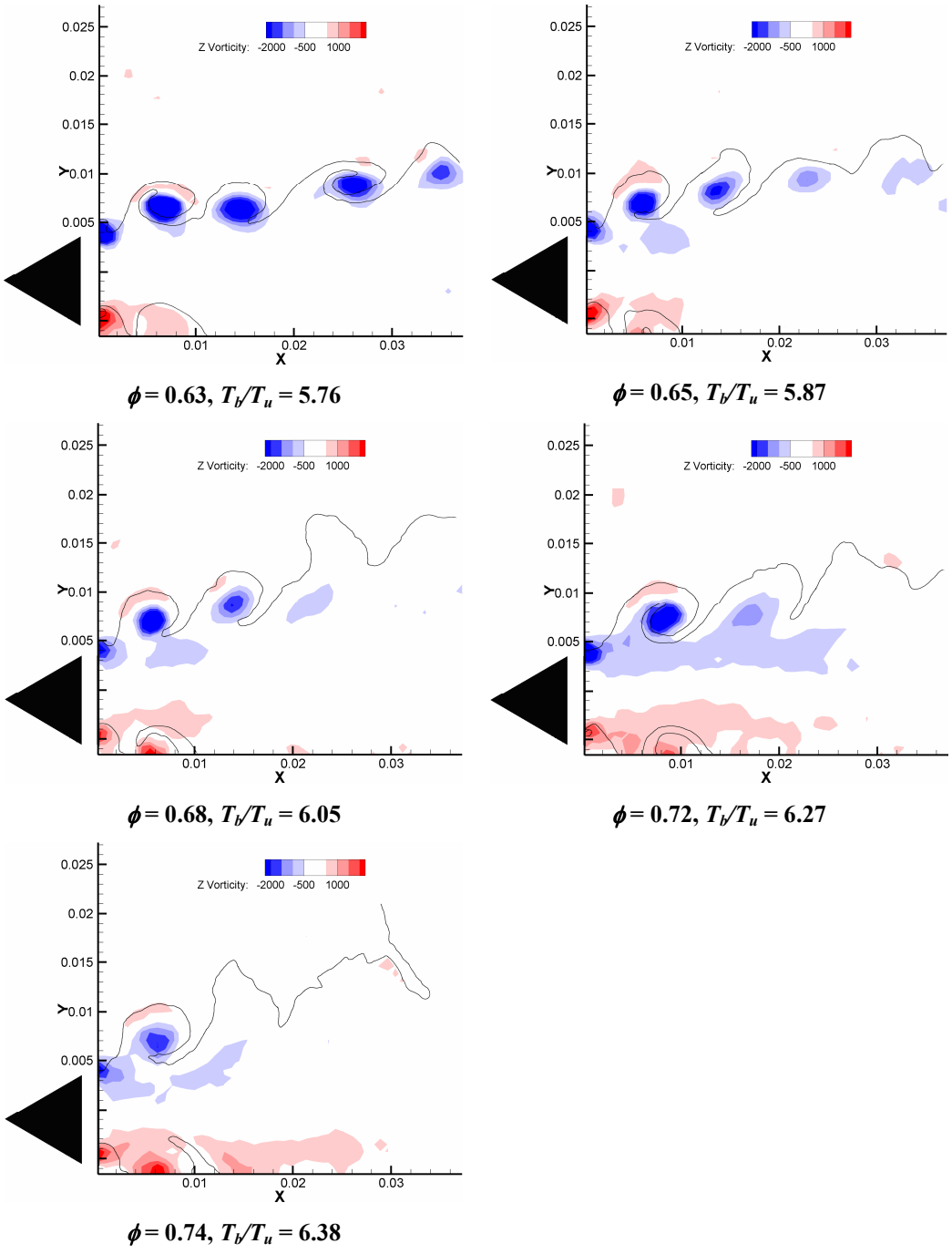

Figure 5.3.2: Illustration of the spatial dependence of the voriticity field at different equivalence ratios, for the same amplitude ($u'/U_\infty = 0.29$) and phase ($\psi = 135^o$) of acoustic excitation. Each image plots the instantaneous vorticity field on which the flame position is overlaid. The position of the bluff body is also shown for reference, drawn to scale. Dimensions on the axes are in meters. Other conditions: $D = 9.52$ mm, $U_\infty = 2.9$ m/s, $f_o = 300$ Hz.

It is also of interest to know whether the temperature jump across the flame changes the decay *rate*, in addition to the point at which the vorticity completely decays. This is less easy to infer from the colored images, and will be analyzed by quantifying the vorticity variation downstream.

To quantify the downstream variation of vorticity, the vorticity amplitude is computed using the peak averaged method, for three different equivalence ratios using data from nine phases for each case, and is plotted in Figure 5.3.3. See that as the equivalence ratio is increased from $\phi = 0.69$ to $\phi = 0.75$[3], the point at which the vorticity completely decays drops by nearly half, however, the initial amplitude does not change so much. Clearly, in addition to the downstream point at which the vorticity completely decays, the decay rate is also affected by the temperature jump across the flame.

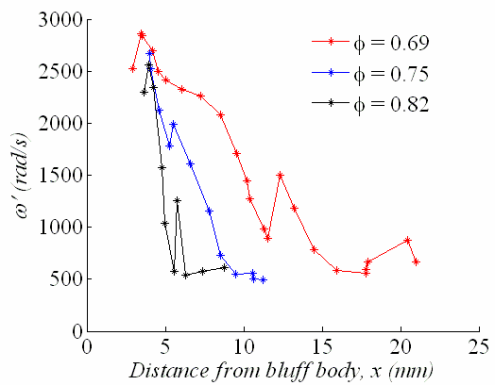

Figure 5.3.3: Vorticity decay downstream : effect of varying equivalence ratio, all other conditions being the same. Other conditions are listed in Table 5.1.

[3] As the equivalence ratio changes the temperatures in the product region also changes. This leads to a different bluff-body temperature and may modify the boundary layer on the surface of the flame-holder. Experiments were conducted by Zukoski (1954) to study any possible effects of this boundary layer preheating, but the results showed a minimal impact on the dynamics downstream.

To further explore the parametric dependencies of vorticity decay, Figure 5.3.4 plots the downstream variation of vorticity for different frequencies (Figure 5.3.4a) and different amplitudues of excitation (Figure 5.3.4b). The mean flow conditions such as velocity, equivalence ratio and bluff body diameter are constant for each figure. Notice that the point at which the voriticity decays completely is the same within each figure. A tiny spread seen for the decay point in Figure 5.3.4b, but this is small compared to the variation in amplitude. Also note that the decay point is Figure 5.3.4a is x = 26 mm, compared to x = 14 mm for is Figure 5.3.4b. The former figure contains data at U_∞ = 4.1 m/s, and the latter U_∞ = 2.3 m/s.

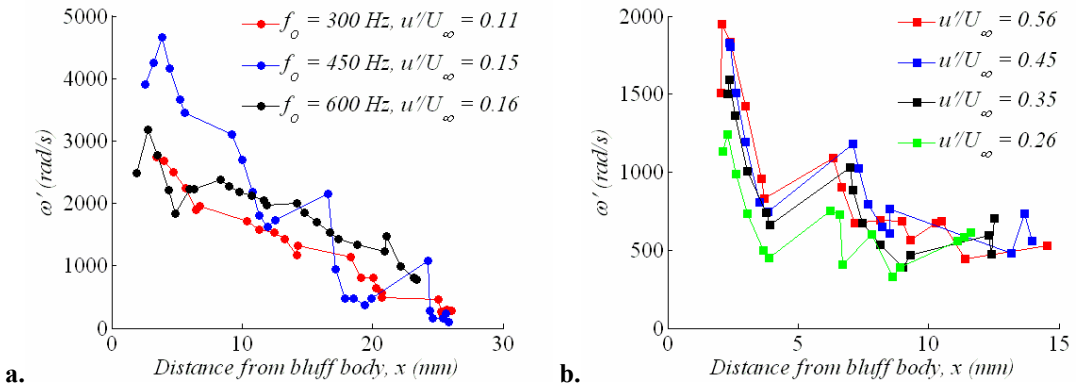

Figure 5.3.4: Illustration of vorticity variation downstream. a. Effect of frequency of excitation b. Effect of amplitude of excitation, at the same frequency. Other conditions are listed in Table 5.1.

It will be next be shown that the point at which the vorticity has completely decayed can be correlated with the recirculation zone length, suggesting that shear layer spreading processes serve as the key mechanism responsible for the decay of the vortices as they evolve downstream. To illustrate, a schematic of the mean flow field is shown in Figure 5.3.5 (left). At the two vertices of the triangle the flow separates and then reattaches downstream at some point along the axis of symmetry. At this closure point

the mean velocity is zero. This point divides the flow into two axial distinct regions- the shear layer/recirculation zone and the wake (note that there is a third region farther downstream where the flow becomes a jet). The region between the separation point and the end of the recirculation zone is the distance over which shear layer spatially evolves; the evolution being primarily governed by viscous diffusion for the Reynolds numbers considered here (i.e. Re_D << 10,000, see Zukoski 1954).

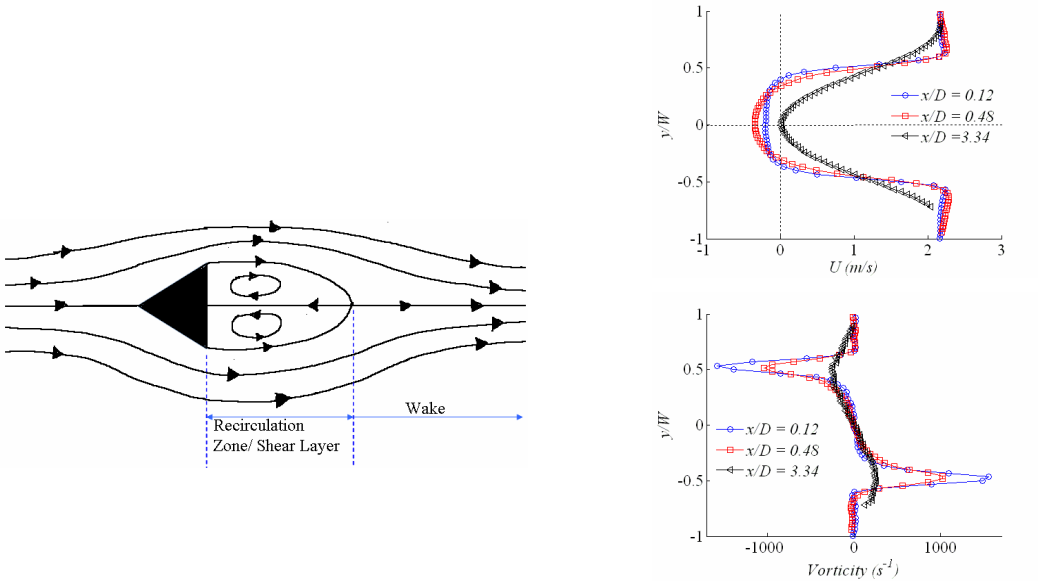

Figure 5.3.5. (Left) Schematic of the streamlines for flow past a triangular bluff body (Right) Transverse velocity (top) and vorticity (bottom) profiles normalized by the shear layer width at different downstream locations (U_∞ = 1.8 m/s, D = 9.52 mm and ϕ = 0.65).

To understand the manner which the shear-layers evolve, merge into each other, then transition into the wake, see Figure 5.3.5 (right). The top and the bottom figures plot the transverse variations in velocity and vorticity respectively, at different downstream locations. Consider the velocity profile close to the bluff body (*x/D = 0.12* in the figures). As the velocity profile evolves, it does so in two stages. The first stage is when the vorticity from the centers of the shear layers have diffused outward and begun to merge, so that there is no region of zero vorticity within the recirculation zone. The shear layers

now evolve with vorticity of opposite signs diffusing into one another as opposed to vorticity of one sign diffusing into a region of zero vorticity. This enhanced evolution continues downstream till the end of the recirculation zone where the center-line velocity is zero (*x/D = 3.34* in the figures). From this point further the separated-flow/recirculation-zone ends and the wake begins. The length of the recirculation zone is controlled by the rate at which the two shear layers diffuse transversely into each other.

With this as background, consider the vorticity decay rate for three bluff bodies diameters, 6.35mm, 12.7mm and 19.05mm. The mean vorticity profiles for the extreme cases are plotted in Figure 5.3.6 (left). Notice that for the smallest bluff-body the shear layers have already merged at the first measurement point, whereas for the largest bluff body it is not until some distance downstream that the shear layers start diffusing into one another. All these three base flow cases were subjected to identical amplitudes of acoustic excitation, see Figure 5.3.6 (right). Notice the slow linear decay for the largest bluff body (*D = 19.05* mm) compared to the near exponential decay of the vorticity amplitude for the smallest bluff body (*D = 6.35* mm). The enhanced decay for the latter can be attributed to the merging (annihilation) of oppositely signed vorticity very close to bluff body resulting in transverse diffusion alongside the axial diffusion of the velocity/vorticity profiles. The bluff body with an intermediate diameter exhibits a decay rate between these extremes. Slightly close to the bluff body, where the shear layers have not merged, the decay is almost linear but after that, it switches over to an exponential type of decay. It seems likely that the decay rates have different characteristics in the regions before and after the shear layers merge. For the majority of cases considered here, the bluff body diameters were small enough that this hypothesized initial region is

very small. However, some caution should be exercised in translating this scaling to much larger bluff body diameters.

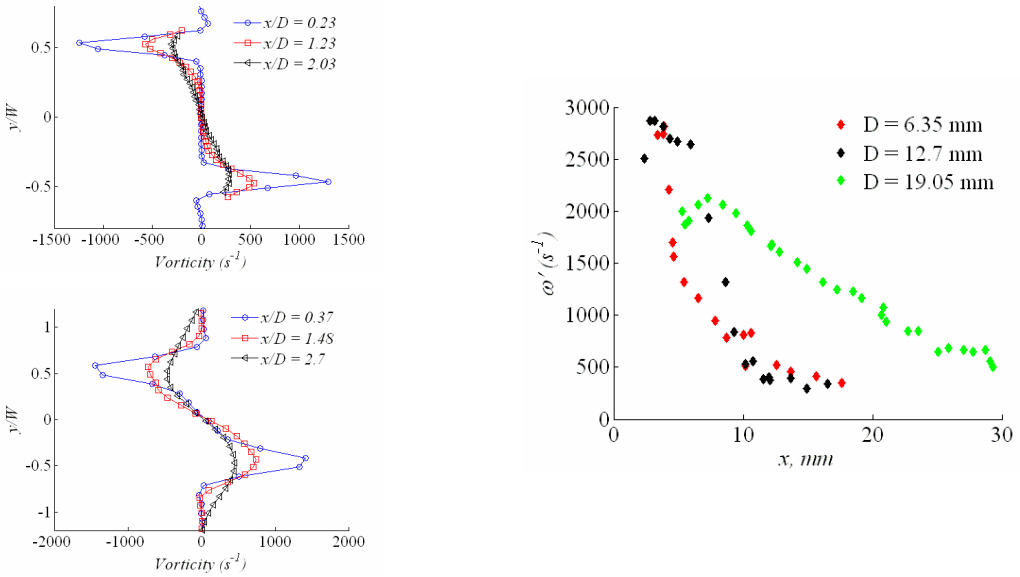

Figure 5.3.6. (Left) Transverse mean vorticity variation without acoustic excitation (mean vorticity) normalized by the separation between the shear layers (*W*) at different axial locations (*D = 19.05* mm, top and *D= 6.35* mm, bottom). (Right) Dependence of vorticity magnitude with axial location for three bluff body diameters Conditions described in Table 5.1.

These considerations can be used to interpret the earlier results which showed strong sensitivities of decay rates to small changes in equivalence ratio (Figure 5.3.2) and quantified in Figure 5.3.3.

Figure 5.3.7a plots the axial variation of the *mean* velocity profiles as they evolve downstream. Figure 5.3.7b is a slice along the centerline, i.e. at $y/D = 0$. Notice that the velocity profiles are nearly identical near the base of the bluff body. This is also true for those portions of the profiles on the reactants side, outside the shear layer, that seem to lie on top of each other as we move downstream. The differences arise on the products side, where it can be seen that the velocities for highest equivalence ratio case are the highest. This change is driven by the velocity jump due to the flame. The higher the temperature ratio, higher the velocity jump.

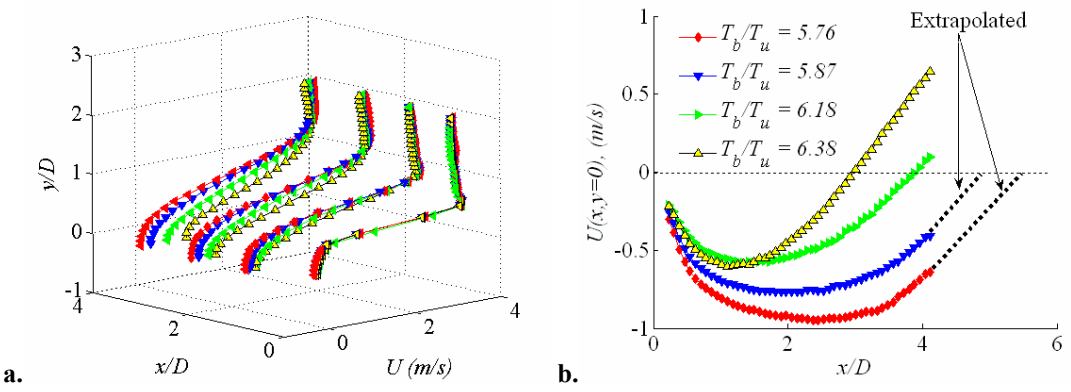

Figure 5.3.7. a. Evolution of the mean velocity profile downstream at four equivalence ratios. b. Variation of axial velocity along the streamline dividing the two recirculation zones. Conditions are described in Table 5.1.

For given upstream conditions, the extent of heat-release dictates the velocity jump at every downstream station and accordingly, the evolution of the velocity profile. Since the rate of change of the velocity profiles is the larger for the higher equivalence ratios, the recirulation zone lengths for those cases should be the shortest. This is validated in Figure 5.3.7b where the point where $U = 0$ occurs along the centerline marks the end of the recirculation zone.

The recirculation zone length is thus a surrogate for the processes that control the decay of vorticity. This fact also helps explain the differences in the decay point seen in Figure 5.3.4a & Figure 5.3.4b. As was explained in §2.2, the recirculation zone length increases with velocity for reacting bluff body flows in which the shear-layer has not transitioned to turbulence. Hence, for the larger velocity case (Figure 5.3.4a), the decay point is further downstream.

This scaling of the point at which vorticity decays, with the recirculation zone length is illustrated in Figure 5.3.8. Figure 5.3.8a plots all the decay profiles without any normalization. Figure 5.3.8b plots the same graph as Figure 5.3.8a, but with the x-axis

normalized with the recirculation zone length (L_r) and with the y-axis normalized with the maximum vorticity amplitude. See that most data scale on this plot, with some deviations being exhibited by the high velocity data (circles). This is due to the fact that the recirculation zone length was so long that it extended beyond the field of view and the length had to be extrapolated, leading to an overestimation in its magnitude.

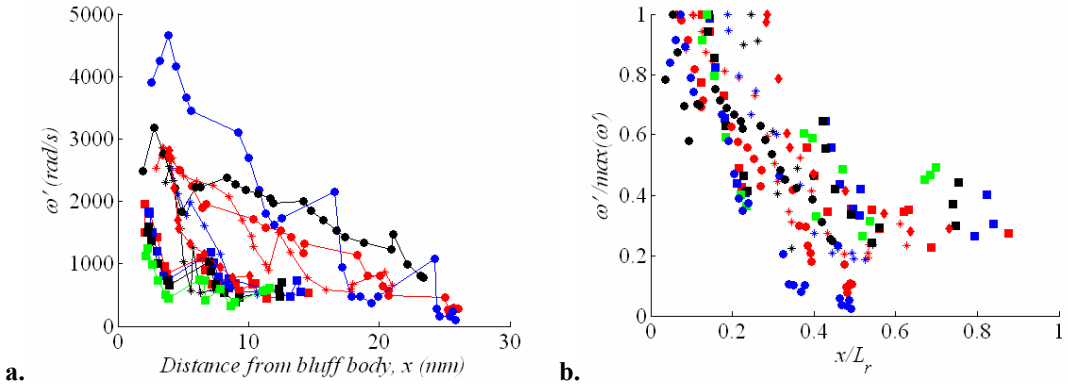

Figure 5.3.8: a. Plot of all the vorticity decay profiles mentioned earlier in the paper. b. Same plot, but with the x-axis normalized by the recirculation zone length. Conditions are described in Table 5.1.

Lastly, for completeness, it should be mentioned that the above discussion does not allow for budgeting the respective roles of viscous diffusion, baroclinic torque or volume dilatation on the decay of vorticity. These are the processes that dictate the transition of the velocity profile from a shear-layer to a wake; these two regions of the flow are separated by the recirculation zone. Nevertheless, no matter how they act, since they modify the transition, their influence on the flow-field will necessarily result in a change in the recirculation zone length.

This decay of vorticity in the shear layer has also been reported in non-reacting flows, as was detailed in Chapter 2. In such situations, viscous diffusion is the only decay process (for 2-D configurations). From this, we infer that viscous diffusion plays an

equally significant role in the decay of vorticity for reacting flows. Particularly, when we compare data across TBB & CBB, we see that when the vortices propagate along the burnt side, their decay is much faster, relative to when they propagate on the unburnt side. The role of combustion in enhancing the decay is a two-step process. First, gas expansion increases the velocities on the product side without affecting the velocities on the reactant side. This reduces the effective velocity gradient in the shear layer, i.e. it smoothes the shear layer. Then, the enhanced product diffusivities accelerate the decay.

5.4.Initial Vorticity Amplitude

This final section describes measurements of the receptivity of the shear-layer right near the bluff body separation point to external perturbations; i.e., to determine the dependencies of $\omega'(s=0)$ in Eq (1).

In a Figure 5.1.1, qualitative results were shown illustrating the amplitude response characteristics of the flow field- i.e., the dependence of the vorticity fluctuation amplitude upon incident acoustic wave amplitude. It is seen that the amplitude of vorticity fluctuations increased monotonically with excitation amplitude at a single frequency. This is quantified in Figure 5.4.1, which plots the response amplitude as a function of the amplitude of excitation, at a single phase ($\psi = 135^o$). These amplitudes were computed using the peak averaged method.

See that for both bluff body shapes tested, a linear dependence is seen for the range of amplitudes at which experiments were conducted. These curves extrapolated to $u'/U_\infty = 0$ do not seem to yield $\omega'=0$, but this is simply because the amplitude at an arbitrary phase ($\psi = 135^o$) is plotted, i.e. $\omega'\sin(135^o)$ is being plotted as opposed to ω' since experiments were done only at one phase.

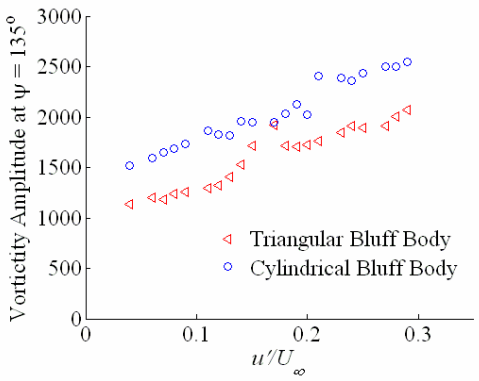

Figure 5.4.1: Dependence of the initial vorticity amplitude at a single phase ($\psi = 135^o$) upon the amplitude of excitation. Conditions: $U_\infty = 2.7$ m/s, $\phi = 0.72$, $D = 9.52$ mm, $f_o = 300$ Hz.

Similar response amplitude dependencies have been observed at other frequencies too, see Figure 5.3.4b. However, it is of interest to compare these response amplitudes across different frequencies of excitation (all other conditions remaining same), i.e. to see whether some frequencies yield higher vorticity amplitudes over others. Some evidence of this behavior is already seen Figure 5.3.4a, which shows that all other conditions being equal, as the frequency of excitation is changed from 450 Hz to 600 Hz, the initial vorticity amplitude that is excited is not the same; it decreases.

To study this effect, experiments were performed over a range of frequencies at a fixed excitation amplitude ($u'/U_\infty = 0.128$) to study the frequency scaling of the shear layer response. At each condition, data were collected at 6 phases. The spatial vorticity profiles at each phase were used to calculate the envelope of the vorticity decay, using the ensemble average method. The maximum amplitudes were then extracted and the results are shown in Figure 5.4.2.

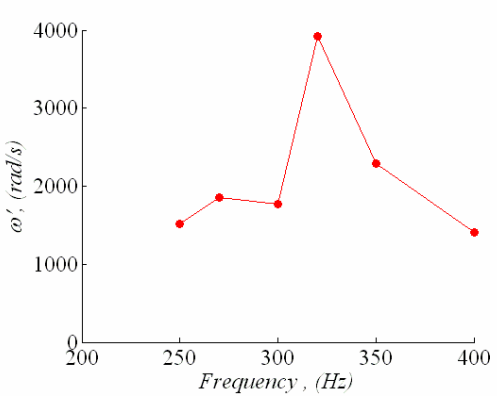

Figure 5.4.2: Initial vorticity amplitude plotted as a function of frequency of excitation, at fixed excitation amplitudes. Conditions: $U_\infty = 2.5$ m/s, $\phi = 0.66$, $D = 9.52$ mm, $u'/U_\infty = 0.128$.

An attempt was also made to non-dimensionalize the above plot by normalising the frequency using a Strouhal number as $St_\theta = f\theta/U_\infty$, where θ is the momentum thickness computed at $x = 0$. This way, the highest vorticity amplitude corresponds to a Strouhal number of $St_\theta = 0.016$.

All of the above points are summarized in an interaction diagram, see Figure 5.4.3.

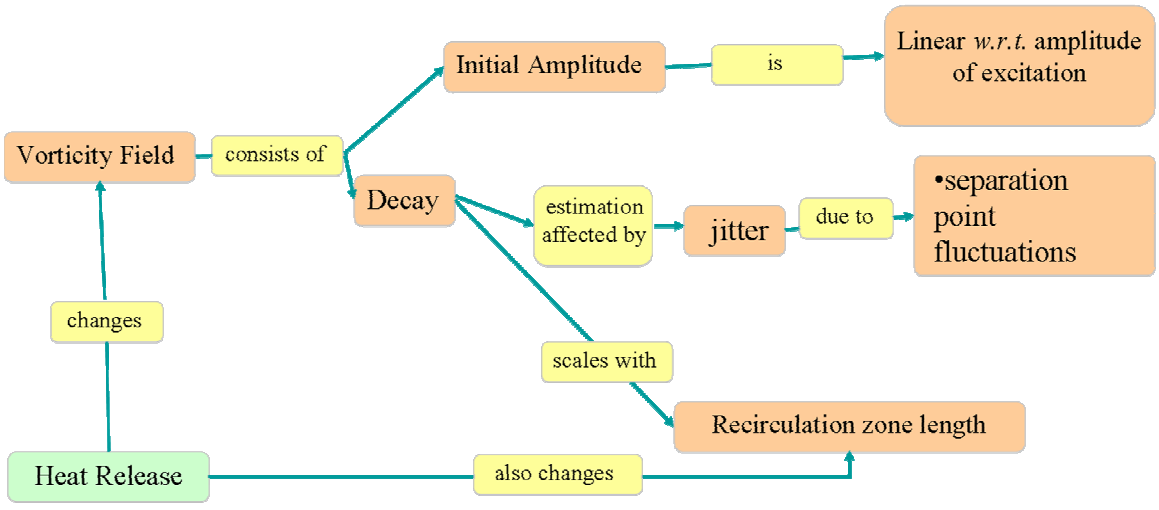

Figure 5.4.3: Interaction diagram summarizing the findings in this chapter

CHAPTER 6

CONCLUDING REMARKS

This chapter summarizes the key contributions of this study (§6.1) and provides some recommendations for future research (§6.2).

6.1.Summary of Contributions

The original contributions of this study were presented in Chapters four and five. The work in the fourth chapter contributes in an improved understanding of the response of bluff-body flames to excitation. Experiments were conducted to understand the response of the flame, i.e. its spatio-temporal characteristics at a range of frequencies, velocities, equivalence ratios and excitation levels.

Despite the source of excitation being acoustic, the disturbances propagated along the flame at a velocity of the order of the mean velocity. This convection velocity (U_{cf}) was found to be independent of the amplitude of acoustic excitation but dependent upon the equivalence ratio and the approach flow speed. For the experiments conducted in this thesis, the values of the convection speed were bounded as $0.8 < U_{cf}/U_{\infty} < 1.1$.

The frequency response characteristics of the flame were found to be similar to a low-pass filter. In all the tests conducted, the coherent flame response was found to first increase, reach a maximum and then decrease. These spatial features have roughly two different behaviors in the near and far field of the bluff body, dominated by linear flame kinematic processes in the near-field and non-linear processes in the far-field. The linear process in the near-field lead to the spatial growth of the flame-front perturbations being proportional to the acoustic velocity at the stabilization point. In contrast, the decay rate

in the far-field depends upon the peak amplitude of the flame response, i.e. the first point downstream of which the decay process starts.

The key processes controlling the response have been identified as 1) the flame anchoring at the bluff body, 2) the excitation of flame-front wrinkles by the oscillating velocity field and 3) flame propagation normal to itself at the local flame speed. The first two processes control the growth of the flame response and the last process controls the decay. Good agreement was obtained when compared with a kinematic model (Shin and Lieuwen 2008) that encapsulated the dominant features of the perturbing velocity field. The key assumption in this model is the flame anchoring boundary condition; this assumption was justified by the experimental data.

In the course of characterizing the flame response, additional non-linearities were observed in the flame-response. For instance, at certain velocity and frequency conditions, the flame-response is low at the frequency of excitation and switches to the first sub-harmonic of the imposed perturbation. Preliminary calculations show that this can be attributed in part to the non-linear dynamics of the shear layers that perturb the flame. As such, obtaining a thorough understanding of the flame-response, particularly its frequency-domain characteristics would necessarily involve accounting for the frequency-domain characteristics of the reacting shear layer that is perturbing the flame.

The fifth chapter of this thesis includes contributions to the understanding of the effect of acoustic excitation on the velocity field of reacting bluff body flows. The acoustic excitation excites the Kelvin-Helmholtz (KH) instability of the reacting shear layer. In turn, the KH instability imposes a convecting, harmonic excitation on the flame, which leads to spatially periodic flame wrinkling and heat-release oscillations.

Understanding the factors influencing these heat release oscillations requires an understanding of the generation, convection, and dissipation of these vortical disturbances. Phase locked particle image velocimetry was carried out over a range of conditions for bluff bodies with triangular and circular cross-sections to understand the processes controlling the decay of vorticity downstream. Of particular significance is the relative location of the flame and vortex sheet. If the vortex sheet is inside the hot products, it dissipates much more rapidly than if it lies in the reactants.

It was found that the baseline mechanism for decay of coherent vorticity fluctuations is governed by shear layer evolution processes. The length over which the decay occurs scales with the length of the recirculation zone of the bluff body, i.e. the length over which the velocity profile transitions from shear layer to wake. The flame influences this decay process in two ways: gas expansion and viscosity increase. Gas expansion across the flame reduces the extent of shear in the velocity profile by reducing the magnitude of negative velocities within the recirculation zone. This combined with the higher product viscosity reduces the length of the recirculation zone, thereby further augmenting the decay of the vorticity fluctuations.

These results also revealed cycle-to-cycle variation in the position of the rolled-up vortices, or phase jitter. Close to the bluff-body, phase jitter is very low but increases monotonically in the downstream direction. This leads to fairly significant differences between instantaneous and ensemble averaged flow fields.

In particular, phase jitter leads to significant differences in the response of triangular and circular bluff-body flow fields to acoustic excitation. The triangle has a well-defined separation point, leading to phase locked and transversely symmetric

vorticity and flame wrinkling. In contrast, while instantaneous images from the circular bluff body look similar to those of the triangle, overlays from cycle to cycle reveal a substantial amount of phase jitter in the vortex sheet, and therefore flame position. Vorticity fluctuations of comparable magnitudes are generated instantaneously for both bluff body shapes, but the spatial jitter leads to reduced ensemble averaged amplitudes for the circular bluff body.

All of the above points are summarized in an interaction diagram, see Figure 6.1.1

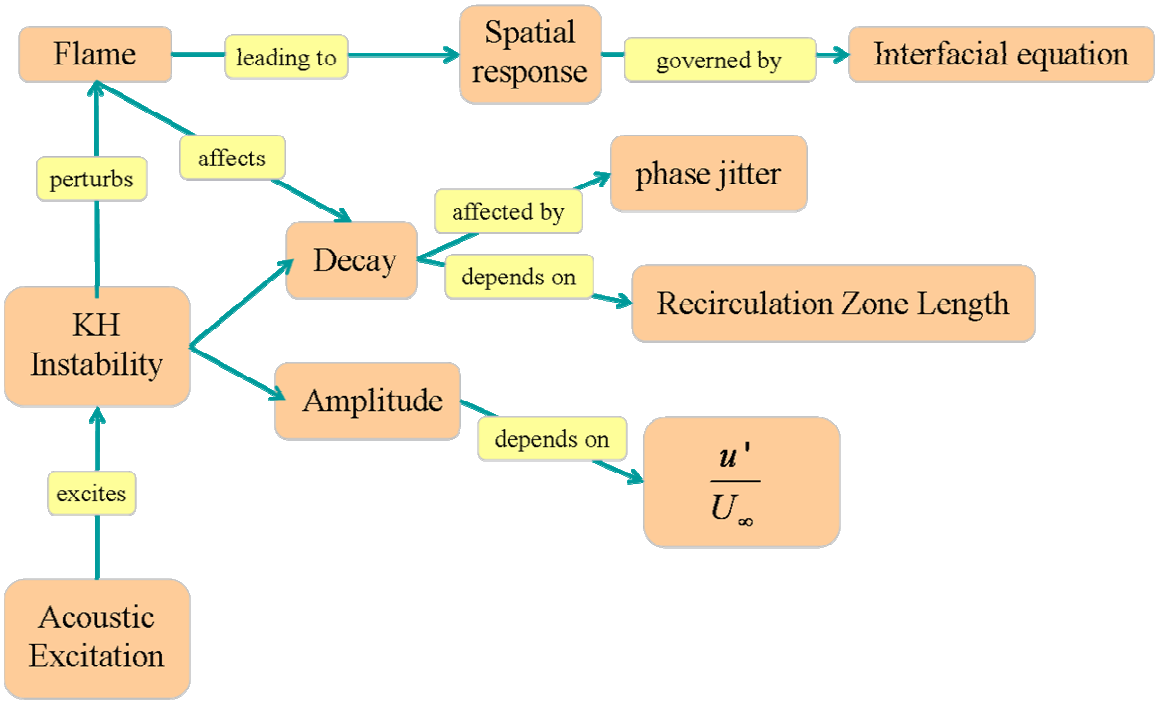

Figure 6.1.1: Interaction diagram summarizing the key findings in this thesis.

6.2.Recommendations for Future Work

This thesis has contributed to the understanding of the response of the reacting shear layers to acoustic excitation and its interaction with the flame. Further research along lines outlined below will help broaden our understanding of bluff body flow-fields.

6.2.1. Physics of Bluff Body Flows

Chapter 2 reviewed the fluid mechanics of bluff body flows. Most of the discussion in that chapter was based on non-reacting flows. Studies of reacting flows revealed interesting results, but the key physics of reacting flows that lead to a departure from the phenomena generic to non-reacting flows is far from clear. Examples of such departures include the absence of the BvK instability in most laboratory experiments conducted on bluff body flows.

There is a need to integrate the various studies that exist on bluff body flows, both reacting and non-reacting. A much-needed element in such a task will be identifying the key non-dimensional parameter that will bridge results that exist in both these realms. Based on the data that exist in the literature, the temperature jump across the flame or the dilatation ratio seems to be promising as a leading order parameter.

Once such parameters are identified, the next step will be identifying the physics leading to a departure. The vortex transport equation shows that three terms are affected by the temperature jump across by the flame – baroclinic torque, volume dilatation and viscous diffusion. Varying the magnitude of the temperature jump changes all the three terms and as such, it does not allow for identifying which of these terms control the physics.

If the temperature jump can be held constant, then carefully constructed experiments can be taken advantage of, to identify the roles of various terms. For instance, by using fuels with varying diffusivities, one can obtain flames with identical temperature jumps but different flame speeds. This will change the inclination of the

flame with respect to the flow and impact the baroclinic torque term more than the other terms.

As regards the role of viscous diffusion, studies already exist on preheated low Reynolds number flows ($Re \sim 50$) to show that as the temperature of the cylinder is increased, the BvK instability is suppressed (Fedorchenko *et al.* 2007). Lecordier *et al.* (1999) conducted experiments with both water and air since they have opposite dependencies of viscosities on temperature. In the air flow experiments, increasing the temperature of the cylinder lead to suppression of the BvK instability. Whereas, in the water flow experiments, suppression of the BvK instability was possible only by cooling the cylinder. From this, they concluded that viscous stresses are responsible for the suppression of the BvK instability. It remains to be whether these results are applicable at higher Reynolds numbers where the inertial forces dominate.

Finally, studies should also be conducted to assess the impact of partial fuel/air premixing on the flow-field. Typically, in afterburners, the fuel is injected through injectors located on the surface of the bluff body. Thus, the fuel and air do not have a sufficient distance to mix perfectly leading to partially premixed combustion downstream of the bluff body.

6.2.2. Response of Bluff Body Flows to Excitation

The regions of the bluff body flow vulnerable to acoustic excitation are the convectively unstable regions, i.e. the shear-layer and the far-wake.

Chapter 5 focused on characterizing the response of the shear layer to acoustic excitation. However, to complete the characterization, further experiments are needed to determine the receptivity of the shear layer. It remains to be seen whether there is a non-

dimensional Strouhal number, based on the momentum thickness that characterizes the receptivity of the reacting shear layer.

All the experiments in this thesis were conducted at high dilatation ratio conditions. Futher investigation is required to determine the extent to which the present results hold if the dilatation ratio is lowered such that the BvK instability is also present. In such a situation, the recirculation zone length does not remain fixed, but changes periodically due to interference with the BvK instability. This would then lead to an unsteady vorticity decay rate.

Next, it is worthwhile to investigate the response of the reacting far-wake to acoustic excitation. The far-wake for non-reacting flows has received some attention, particularly with regard to its behavior under acoustic excitation, see Desruelle (1983) & Williamson and Prasad (1993). Figure 2.8 (Chapter 2) showed a sample combustion result where the far-wake commenced at x/D = 10 (for Re_D = 950, ϕ = 0.71). However, for non-reacting flows, the equation provided by Vorobieff *et al.* (2002) shows that far wake does not start until x/D = 38, at the same Reynolds number. Clearly, the far wake is much closer to the cylinder for reacting flows.

APPENDIX A : FUEL FLOW-METER CALIBRATION

The fuel flow rate was measured with a Dwyer RM-40-400-SSV 12" scale flow meter. The scale on such flow meters are calibrated for use with air. A calibration was done with a Ritter drum type TG25-5 gas calibrator for natural gas operation.

The calibration curve is shown in Figure 6.2.1. The *x*-axis on this curve is labeled as 'Computed fuel flow rate'. This means that the reading from the flow-meter display was corrected for molecular weights to get an estimate for the fuel flow rate of the gas. This is then compared with the fuel flow reading from the calibrator, which is plotted on the y-axis.

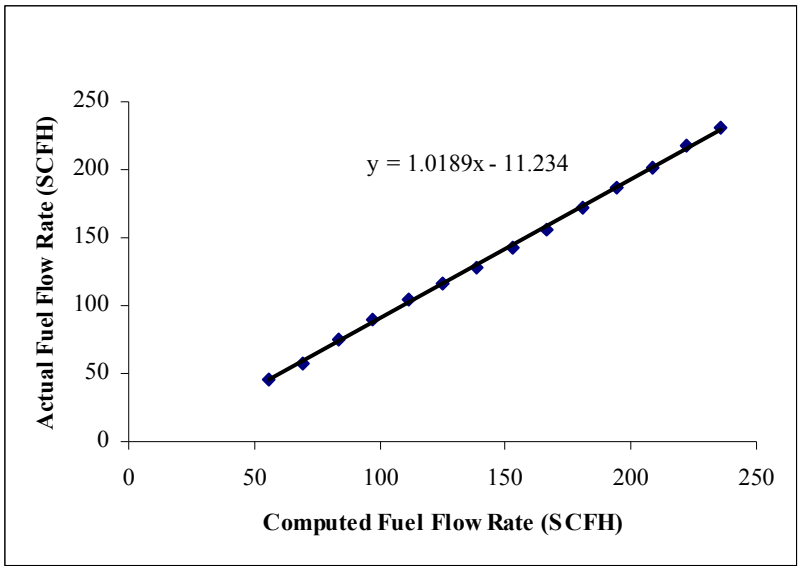

Figure 6.2.1: Calibration curve for the fuel flow meter

Thus, from the figure, we can conclude that that the bias in the fuel flow rate estimation is 1.8%, within the range of interest (50 -220 SCFH).

APPENDIX B: DETAILS OF THEORETICAL PREDICTION (SHIN AND LIEUWEN 2008).

The purpose of this appendix is to reproduce the key features of the theoretical predictions by Shin and Lieuwen (2008), for ready reference.

The co-ordinate system used in the formulation is illustrated in Figure 6.2.1. Note that the convention adopted is $G<0$ for the reactants and $G>0$ for products. Accordingly the flame is the $G=0$ level set.

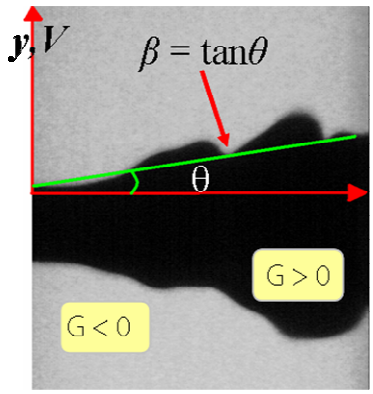

Figure 6.2.1: Co-ordinate system and definitions used in the theoretical formulation. The flow is from left to right.

Starting with the interfacial equation:

$$\frac{\partial G}{\partial t} + \vec{u} \cdot \vec{\nabla} G = S_L \left| \vec{\nabla} G \right| \tag{1.10}$$

the flame is represented as:

$$G(x, y, t) = L(x, t) - y$$

In the above equation the definition of L(y,t) is identical to the one adopted in Chapter 4. Now, the flame front motion is decomposed into mean and fluctuating components as:

$$L(x,t) = \beta x + L'(x,t)$$

Substituting this into (1.10), we get the equation for the flame front motion:

$$\frac{\partial L'}{\partial t} + U\left(\beta + \frac{\partial L'}{\partial x}\right) - V = S_L\left(\sqrt{1+\beta^2} + \frac{\beta}{\sqrt{1+\beta^2}}\frac{\partial L'}{\partial x}\right) \quad (1.13)$$

Note that the non-linear terms are still kept intact on the r.h.s. After linearizing this term, and applying the flame anchoring assumption:

$$\frac{\partial L'(x=0,t)}{\partial t} = 0$$

This along with a decomposition of the velocity field into a mean and oscillating component as:

$$\begin{aligned} U(x,y,t) &= \bar{U}(x,y) + u'(x,y,t) \\ V(x,y,t) &= \bar{V}(x,y) + v'(x,y,t) \end{aligned} \quad (1.15)$$

The, equation (1.13) reduces to:

$$\cos^2\theta\left(\bar{U}\cos\theta + \bar{V}\sin\theta\right)\frac{\partial L'(x=0,t)}{\partial x} = v'\cos\theta - u'\sin\theta \quad (1.16)$$

Applying a co-ordinate transform, the above expression reduces to:

$$\frac{\partial L'(x=0)}{\partial x} = \frac{1}{\cos^2\theta}\frac{u_n'}{\bar{U}_t}$$

The above expression predicts the slope of the flame response close to the base of the bluff body and will be compared with the experimental data in Chapter 4.

REFERENCES

AMES, L. E. 1956 Interference Effects between Multiple Bluff Body Flameholders. *Aeronautical Engineer Thesis*, California Insitute of Technology, Pasadena

BAILLOT, F., DUROX, D., DUCRUIX, S., SEARBY, G. and BOYER, L. 1999 Parametric Response of a Conical Flame to Acoustic Waves.*Combust. Sci. Technol.* **142**, 91-109

BARKER, C. L. R. 1958 Experiments Concerning the Occurrence and Mechanism of High-Frequency Combustion Instability. *PhD Thesis*, California Institute of Technology, Pasadena

BEARMAN, P. 1969 On Vortex Shedding from a Circular Cylinder in the Critical Reynolds Number Regime.*J. Fluid Mech.* **37**, 577

BÉDAT, B. and CHENG, R. K. 1995 Experimental Study of Premixed Flames in Intense Isotropic Turbulence.*Combust. Flame* **100**, 485-494

BEER, J. and CHIGIER, N. 1972 Combustion Aerodynamics. John Wiley and Sons New York

BILL, R. G., JR. and TARABANIS, K. 1986 The Effect of Premixed Combustion on the Recirculation Zone of Circular Cylinders.*Combust. Sci. Technol.* **47**, 39-53

BIRBAUD, A. L., DUROX, D. and CANDEL, S. 2006 Upstream Flow Dynamics of a Laminar Premixed Conical Flame Submitted to Acoustic Modulations.*Combust. Flame* **146**, 541-552

BLEVINS, R. D. 2006 The Effect of Sound on Vortex Shedding from Cylinders.*J. Fluid Mech.* **161**, 217-237

BLEVINS, R. D. 1985 The Effect of Sound on Vortex Shedding from Cylinders.*J. Fluid Mech.* **161**, 217-237

BLOOR, M. S. 1964 The Transition to Turbulence in the Wake of a Cylinder.*J. Fluid Mech.* **19**, 290-304

BOVINA, T. A. 1959 Studies of Exchange between Re-Circulation Zone Behind the Flame-Holder and Outer Flow.*Proc. Combust. Inst.* **7**, 692-696

BROWN, G. L. and ROSHKO, A. 1974 On Density Effects and Large Structure in Turbulent Mixing Layers.*J. Fluid Mech.* **64**, 775-816

BUSH, S. M. and GUTMARK, E. J. 2006 Reacting and Non-Reacting Flow Fields of a V-Gutter Stabilized Flame. *44th AIAA Aerospace Sciences & Meeting* AIAA Paper No. 2006-807

BUSH, S. M. and GUTMARK, E. J. 2007 Reacting and Nonreacting Flowfields of a V-Gutter Stabilized Flame.*AIAA J.* **45**, 662-672

CANTWELL, B. and COLES, D. 1983 An Experimental Study of Entrainment and Transport in the Turbulent near Wake of a Circular Cylinder.*J. Fluid Mech.* **136**, 321-374

CARDELL, G. S. 1993 Flow Past a Circular Cylinder with a Permeable Splitter Plate. *PhD Thesis*, California Insititute of Technology, Pasadena

CHAKRAVARTHY, V. K. and MENON, S. 1999 Large Eddy Simulations of Confined Bluff Body Stabilized Highly Turbulent Premixed Flames. *ASME Fluids Engineering Summer Meeting* Paper No. FEDSM-99-7798

CIMBALA, J. M. 1984 Large Structure in the Far Wakes of Two-Dimensional Bluff Bodies. *PhD Thesis*, California Institute of Technology, Pasadena

CIMBALA, J. M., NAGIB, H. M. and ROSHKO, A. 1988 Large Structure in the Far Wakes of Two Dimensional Bluff Bodies.*J. Fluid Mech.* **190**, 265

COATS, C. M. 1996 Coherent Structures in Combustion.*Progr. Energy Combust. Sci.* **22**, 427-509

COHEN, J. M. and ANDERSON, T. J. 1996 Experimental Investigation of near-Blowout Instabilities in a Lean, Premixed Step Combustor. *AIAA Aerospace Sciences Meeting and Exhibit* AIAA Paper No. 96-0819

CROW, S. C. and CHAMPAGNE, F. H. 1971 Orderly Structure in Jet Turbulence.*J. Fluid Mech.* **48**, 547-591

DESRUELLE, D. 1983 Beyond the Karman Vortex Street. *Masters Thesis*, Illinois Institute of Technology, Chicago, Illinois

DUCRUIX, S., SCHULLER, T., DUROX, D. and CANDEL, S. 2003 Combustion Dynamics and Instabilities: Elementary Coupling and Driving Mechanisms.*J. Propul. Power* **19**, 722-734

DUNLAP, R. A. 1950 Resonance of a Flame in a Parallel-Walled Combustion Chamber. *UMM-43* Aeronautical Research Center, Engineering Research Institute, University of Michigan

EBRAHIMI, H. 2006 Overview of Gas Turbine Augmentor Design, Operation, and Combustion Oscillation. *42nd AIAA/ASME/SAE/ASEE Joint Propulsion Conference & Exhibit* AIAA Paper No. 2006-4916

EMMONS, H. W. 1958 Flow Discontinuities Associated with Combustion, Fundamentals of Gas Dynamics in *High Speed Aerodynamics and Jet Propulsion* (ed. H. W. Emmons) Princeton University Press Princeton

ERICKSON, R. R., SOTERIOU, M. C. and MEHTA, P. G. 2006 The Influence of Temperature Ratio on the Dynamics of Bluff Body Stabilized Flames. *44th AIAA Aerospace Sciences Meeting & Exhibit* AIAA Paper No. 2006-753

FEDORCHENKO, A. I., TRÁVNÍCEK, Z. and WANG, A. B. 2007 On the Effective Temperature Concept in the Problem of Laminar Vortex Shedding Behind a Heated Circular Cylinder.*Phys. Fluids* **19**, 051701

FOSTER, J. R. 1956 Effects of Combustion Chamber Blockage on Bluff Body Flame Stabilization. *Aeronautical Engineer Thesis*, California Institute of Technology,

FUJII, S. and EGUCHI, K. 1981 A Comparison of Cold and Reacting Flows around a Bluff-Body Flame Stabilizer.*J. Fluid Eng.* **103**, 328-334

FUREBY, C. and LOFSTROM, C. 1994 Large Eddy Simulations of Bluff Body Stabilized Flames.*Proc. Combust. Inst.* **25**, 1257-1264

FUREBY, C. and MOLLER, S.-I. 1995 Large Eddy Simulation of Reacting Flows Applied to Bluff Body Stabilized Flames.*AIAA J.* **33**, 2339-2347

GERRARD, J. 1965 A Disturbance Sensitive Reynolds Number Range of the Flow Past a Circular Cylinder.*J. Fluid Mech.* **22**, 187-196

GHONIEM, A. F., ANNASWAMY, A., WEE, D., YI, T. and PARK, S. 2002 Shear Flow-Driven Combustion Instability: Evidence, Simulation, and Modeling.*Proc. Combust. Inst.* **29**, 53-60

HARP, J. L., MALLETT, W. E. and SHILLITO, T. B. 1954 Experimental Sea-Level Static Investigation of a Short Afterburner. *NACA RM E54B18*

HEGDE, U. G., REUTER, D., DANIEL, B. R. and ZINN, B. T. 1987 Flame Driving of Longitudinal Instabilities in Dump Type Ramjet Combustors.*Combust. Sci. Technol.* **55**, 125-138

HERMANSON, J. C. and DIMOTAKIS, P. E. 1989 Effects of Heat Release in a Turbulent, Reacting Shear Layer.*J. Fluid Mech.* **199**, 333-375

HERTZBERG, J. R., SHEPHERD, I. G. and TALBOT, L. 1991 Vortex Shedding Behind Rod Stabilized Flames.*Combust. Flame* **86**, 1-11

HO, C. M. and HUERRE, P. 1984 Perturbed Free Shear Layers.*Ann. Rev. Fluid Mech.* **16**, 365-422

HOMANN, F. 1936 Einfluß Großer Zähigkeit Bei Strömung Um Zylinder.*Forschung im Ingenieurwesen* **7**, 1-10

HUERRE, P. and MONKEWITZ, P. A. 1990 Local and Global Instabilities in Spatially Developing Flows.*Ann. Rev. Fluid Mech.* **22**, 473-537

KASKAN, W. E. and NOREEN, A. E. 1955 High-Frequency Oscillations of a Flame Held by a Bluff Body.*ASME Transactions* **77**, 885-895

KIEL, B. V. 2001 Review of Advances in Combustion Control, Actuation, Sensing, Modelling and Related Technologies for Air Breathing Gas Turbines. *AIAA Aerospace Sciences Meeting and Exhibit* AIAA Paper No. 2001-0481

KNAUS, D. A. and GOULDIN, F. C. 2000 Measurements of Flamelet Orientations in Premixed Flames with Positive and Negative Markstein Numbers.*Proc. Combust. Inst.* **28**, 367-373

KOURTA, A., BOISSON, H. C., CHASSAING, P. and MINH, H. H. 1987 Nonlinear Interaction and the Transition to Turbulence in the Wake of a Circular Cylinder.*J. Fluid Mech.* **181**, 141-161

LAW, C. K. and SUNG, C. J. 2000 Structure, Aerodynamics, and Geometry of Premixed Flamelets.*Progr. Energy Combust. Sci.* **26**, 459-505

LECORDIER, J. C., DUMOUCHEL, F. and PARANTHOËN, P. 1999 Heat Transfer in a Benard-Karman Vortex Street in Air and in Water.*Int. J. Heat Mass Transfer* **42**, 3131

LIEUWEN, T. C. 1999 Investigation of Combustion Instability Mechanisms in Premixed Gas Turbines. *PhD Thesis*, Georgia Institute of Technology, Atlanta, Georgia

LOUCH, D. S. and BRAY, K. N. C. 2001 Vorticity in Unsteady Premixed Flames: Vortex Pair–Premixed Flame Interactions under Imposed Body Forces and Various Degrees of Heat Release and Laminar Flame Thickness.*Combust. Flame* **125**, 1279-1309

LOVETT, J. A., BROGAN, T. P., PHILIPPONA, D. S., KEIL, B. V. and THOMPSON, T. V. 2004 Development Needs for Advanced Afterburner Designs. *40th AIAA/ASME/SAE/ASEE Joint Propulsion Conference & Exhibit* AIAA Paper No. 2004-4192

MCMURTRY, P. A., RILEY, J. J. and METCALFE, R. W. 1989 Effects of Heat Release on the Large-Scale Structure in Turbulent Mixing Layers.*J. Fluid Mech.* **199**, 297-332

MEHTA, P. G. and SOTERIOU, M. C. 2003 Combustion Heat Release Effects on the Dynamics of Bluff Body Stabilized Premixed Reacting Flows. *41st Aerospace Sciences Meeting & Exhibit* AIAA Paper No. 2003-835

MURUGANANDAM, T. M. 2006 Sensing and Dynamics of Lean Blowout in a Swirl Dump Combustor. *PhD Thesis*, Georgia Institute of Technology, Atlanta, GA

NAIR, S. 2006 Acoustic Detection of Blowout Phenomenon. *PhD Thesis*, Georgia Institute of Technology, Atlanta

NAIR, S. and LIEUWEN, T. 2007 Near-Blowoff Dynamics of a Bluff-Body Stabilized Flames.*J. Propul. Power* **23**, 421-427

NICHOLSON, H. M. and FIELD, J. P. 1948 Some Experimental Techniques for the Investigation of the Mechanism of Flame Stabilization in the Wakes of Bluff Bodies.*Proc. Combust. Inst.* **3**, 44-68

NOTTIN, C., KNIKKER, R., BOGER, M. and VEYNANTE, D. 2000 Large Eddy Simulations of an Acoustically Excited Turbulent Premixed Flame.*Proc. Combust. Inst.* **28**, 67-73

PAN, J. C. 1991 Laser Diagnostic Studies of Confined Turbulent Premixed Flames Stabilized by Conical Bluff Bodies. *PhD Thesis*, University of Dayton, Dayton, OH

PAN, J. C., VANGSNESS, M. D. and BALLAL, D. R. 1992 Aerodynamics of Bluff-Body Stabilized Confined Turbulent Premixed Flames.*J. Eng. Gas Turb. Power* **114**, 783-789

PERRY, A. E., CHONG, M. S. and LIM, T. T. 1982 The Vortex Shedding Process Behind Two-Dimensional Bluff Bodies.*J. Fluid Mech.* **116**, 77-90

PLASCHKO, P., BERGER, E. and PERALTA-FABI, R. 1993 Periodic Flow in the near Wake of Straight Circular Cylinders.*Phys. Fluids A-Fluid* **5**, 1718

POINSOT, T. and VEYNANTE, D. 2001 Theoretical and Numerical Combustion. RT Edwards Inc Flourtown PA

POINSOT, T. J., TROUVE, A. C., VEYNANTE, D. P., CANDEL, S. M. and ESPOSITO, E. J. 1987 Vortex-Driven Acoustically Coupled Combustion Instabilities.*J. Fluid Mech.* **177**, 265-292

POTTER, A. E., JR. and WONG, E. L. 1958 Effect of Pressure and Duct Geometry on Bluff-Body Flame Stabilization. *NACA TN 4381* National Advisory Committee on Aeronautics

PRASAD, A. and WILLIAMSON, C. H. K. 1997 The Instability of the Shear Layer Separating from a Bluff Body.*J. Fluid Mech.* **333**, 375-402

PREETHAM 2007 Modeling the Response of Premixed Flames to Flow Distrubances. *PhD Thesis*, Georgia Institute of Technology, Atlanta, GA

PREETHAM and LIEUWEN, T. 2004 Nonlinear Flame-Flow Transfer Function Calculations: Flow Disturbance Celerity Effects. *40th AIAA/ASME/SAE/ASEE Joint Propulsion Conference & Exhibit* Paper No. AIAA 2004-4035

PREETHAM and LIEUWEN, T. 2005 Nonlinear Flame-Flow Transfer Function Calculations: Flow Disturbance Celerity Effects Part 2. *43rd AIAA Aerospace Sciences Meeting & Exhibit* Paper No. AIAA 2005-0543

PROVANSAL, M., MATHIS, C. and BOYER, L. 2006 Bénard-Von Kármán Instability: Transient and Forced Regimes.*Journal of Fluid Mechanics Digital Archive* **182**, 1-22

RAFFEL, M., WILLERT, C. and KOMPENHANS, J. 1998 Particle Image Velocimetry: A Practical Guide. Springer Verlag New York

RAYLEIGH, J. W. S. 1896 The Theory of Sound, Vol. 2. Mc. Millan & Co London and New York

REUTER, D. M. 1988 Investigation of Combustion Instability in Ramjet Combustors. *PhD Thesis*, Georgia Institute of Technology, Atlanta, GA

RHEE, C. W., TALBOT, L. and SETHIAN, J. A. 1995 Dynamical Behaviour of a Premixed Turbulent Open V-Flame.*J. Fluid Mech.* **300**, 87-115

ROGERS, D. E. and MARBLE, F. E. 1956 A Mechanism for High Frequency Oscillations in Ramjet Combustors and Afterburners.*Jet Propulsion* **26**, 456–462

ROSHKO, A. 1954 On the Drag and Shedding Frequency of Two-Dimensional Bluff Bodies.

ROSHKO, A. 1954 On the Drag and Shedding Frequency of Two-Dimensional Bluff Bodies. *NACA TN-3169* National Advisory Committee on Aeronautics

SATO, H. 1956 Experimental Investigation on the Transition of Laminar Separated Layer.*J. Phys. Soc. Jpn.* **11**, 702-709

SCHADOW, K. C. and GUTMARK, E. 1992 Combustion Instability Related to Vortex Shedding in Dump Combustors and Their Passive Control.*Progr. Energy Combust. Sci.* **18**, 117-132

SCHILLER, L. and LINKE, W. 1933 Pressure and Frictional Resistance of a Cylinder at Reynolds Numbers 5,000 to 40,000. *NACA TM-715* National Advisory Committee on Aeronautics

SCHULLER, T., DUROX, D. and CANDEL, S. 2003 A Unified Model for the Prediction of Laminar Flame Transfer Functions Comparisons between Conical and V-Flame Dynamics.*Combust. Flame* **134**, 21-34

SHERIDAN, J., SORIA, J., WU, J. and WELSH, M. C. 1991 The Kelvin-Helmholtz Instability of the Separated Shear Layer from a Circular Cylinder.

SHIN, D.-H. and LIEUWEN, T. 2008 Premixed Flame Kinematics in an Axially Decaying, Harmonically Oscillating Vorticity Field. *44th AIAA Joint Propulsion Conference and Exhibit* Paper No. AIAA-2008-5042

SINIBALDI, J. O., MUELLER, C. J., TULKKI, A. E. and DRISCOLL, J. F. 1998 Suppression of Flame Wrinkling by Buoyancy - the Baroclinic Stabilization Mechanism.*AIAA J.* **36**, 1432-1438

SMITH, C., NICKOLAUS, D., LEACH, T., KIEL, B. and GARWICK, K. 2007 Les Blowout Analysis of Premixed Flow Past V-Gutter Flameholder. *45th AIAA Aerospace Sciences Meeting and Exhibit* AIAA Paper No. 2007-170

SOMERS, S. L. 2004 Duct Burners in *Industrial Burners Handbook* (ed. C. E. Baukal) CRC Press New York

SOTERIOU, M. C. and GHONIEM, A. F. 1994 The Vorticity Dynamics of an Exothermic, Spatially Developing, Forced Reacting Shear Layer.*Proceedings of the Combustion Institute* **25**, 1265-1272

TAYLOR, G. I. 1922 Diffusion by Continuous Movements.*Proceedings of the London Mathematical Society* **2**, 196

THURSTON, D. W. 1958 An Experimental Investigation of Flame Spreading from Bluff Body Flameholders. *Aeronautical Engineer Thesis*, California Institute of Technology, Pasadena

USOW, K. H., MEYER, C. L. and SCHULZE, F. W. 1953 Experimental Investigation of Screeching Combustion in Full-Scale Afterburner. *NACA RM E53I01*

VOROBIEFF, P., GEORGIEV, D. and INGBER, M. S. 2002 Onset of the Second Wake: Dependence on the Reynolds Number.*Phys. Fluids* **14**, L53

WILLIAMS, G. C., HOTTEL, H. C. and SCURLOCK, A. C. 1951 Flame Stabilization and Propagation in High Velocity Gas Streams.*Proc. Combust. Inst.* **3**, 21-40

WILLIAMSON, C. H. K. 1996 Vortex Dynamics in the Cylinder Wake.*Ann. Rev. Fluid Mech.* **28**, 477-539

WILLIAMSON, C. H. K. and PRASAD, A. 1993 A New Mechanism for Oblique Wave Resonance in the 'Natural'far Wake.*J. Fluid Mech.* **256**, 269-313

WILLIAMSON, C. H. K. and PRASAD, A. 1993 Oblique Wave Interactions in the Far Wake.*Phys. Fluids* **5**, 1854–1857

WINTERFELD, G. 1965 On Processes of Turbulent Exchange Behind Flame Holders.*Proc. Combust. Inst.* **10**, 1265-1275

WU, M. S. and DRISCOLL, J. F. 1992 A Numerical Simulation of a Vortex Convected through a Laminar Premixed Flame.*Combust. Flame* **91**, 310-322

YAMAGUCHI, S., OHIWA, N. and HASEGAWA, T. 1985 Structure and Blow-Off Mechanism of Rod-Stabilized Premixed Flame.*Combust. Flame* **62**, 31-41

YANG, J. T., TSAI, G. L. and WANG, W. B. 1994 Near-Wake Characteristics of Various V-Shaped Bluff Bodies.*J. Propul. Power* **10**, 47-53

YANG, J. T., YEN, C. W. and TSAI, G. L. 1994 Flame Stabilization in the Wake Flow Behind a Slit V-Gutter.*Combust. Flame* **99**, 288-294

YU, K. H., TROUVÉ, A. and DAILY, J. W. 1991 Low-Frequency Pressure Oscillations in a Model Ramjet Combustor.*J. Fluid Mech.* **232**, 47-72

ZDRAVKOVICH, M. M. 1997 Flow around Circular Cylinders: A Comprehensive Guide through Flow Phenomena, Experiments, Applications, Mathematical Models, and Computer Simulations. Oxford University Press

ZUKOSKI, E. E. 1997 Afterburners in *Aerothermodynamics of Gas Turbine and Rocket Propulsion* (ed. G. Oates)

ZUKOSKI, E. E. 1954 Flame Stabilization on Bluff Bodies at Low and Intermediate Reynolds Numbers. *PhD Thesis*, California Institute of Technology, Pasadena

ZUKOSKI, E. E. and MARBLE, F. E. 1956 Experiments Concerning the Mechanism of Flame Blowoff Form Bluff Bodies.*Proceedings of the Gas Dynamics Symposium on Aerothermochemistry* 205 - 210

VITA

Santosh Janardhan Shanbhogue was born in Bombay, India on 17th March 1982, the son of Subash and Veena Shanbhogue. He attended K-12 in the United Arab Emirates. He received his bachelor's degree in Aerospace Engineering from the Indian Institute of Technology, Madras, India in 2003 and his Master of Science degree in Aerospace Engineering in 2005 from Georgia Institute of Technology, Atlanta, GA, U.S.A.